Toledo resides at approximately 42 degrees northern latitude. Since the solar declination angle as well as insolation undergoes the greatest variations in magnitude between the solstices and equinoxes, these would represent the most extreme changes in solar heating that could be expected during the course of a single year. Consequently, thermal analyses were conducted for conditions representative at these four times. [redacted]

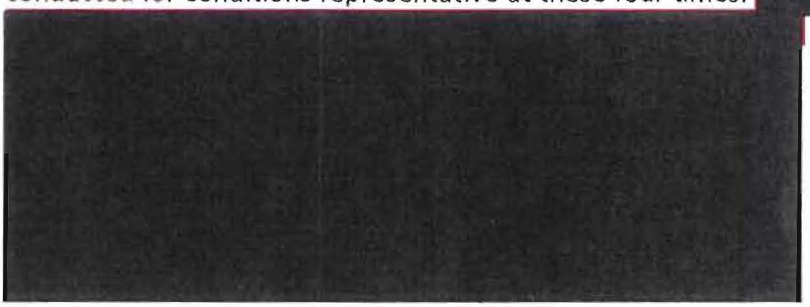

Aside from variations in the solar flux, the length of day also varies through the course of the year, being longest at the summer solstice and least at the winter solstice. Solar heating would only be present when the sun is visible in the sky. This will occur when the zenith angle is 90 degrees or less. Sunrise and sunset will occur when the zenith angle is precisely 90 degrees. Using a latitude of 42 degrees along with the appropriate solar declination angle, the corresponding hour angle that marked sunrise and sunset was calculated. In this way the number of hours when daylight was present was determined. This enabled precisely locating not only the solar position relative to the zenith but also relative to east and west. Using this methodology, it was determined that at the Summer Solstice, the longest period of daylight was 15 hours whereas at Winter Solstice there was only 9 hours of daylight. At both Equinoxes, there was precisely 12 hours of daylight. These daylight hours were checked online for accuracy at the US Naval Oceanography Portal (http://www.usno.navy.mil/USNO/astronomical-applications/data-services/rs-one-year-us). Here the number of daylight hours as well as the time of sunrise and sunset can be determined for any location worldwide and for any month of any year.

The solar heating was treated as a directional flux of constant intensity during the hours of daylight. The direction cosines relative to east-west, north-south, and the zenith were derived as a function of the time of day. These definitions were used by NASTRAN to determine the direction of the solar flux as well as those portions of the outer concrete shield building that would be lit as well as those portions that would be shaded. In addition to the shading attributed to suns position in the sky, additional shading provided by any adjacent structures had to be taken into account. This was especially true of the auxiliary building that resides adjacent to the eastern half of the concrete shield building. Consequently, a Boolean solid representation of the auxiliary building was derived that approximated its outer shape. This was coarsely meshed and included in the model solely for the purposes of including any shading effects. Temperatures were not calculated or recovered for this structure. Rather it was assumed to have the same temperature as the surrounding ambient environment. In Figure 3,

the 9:00am temperatures contours that were calculated for the summer solstice are plotted along with an outline of the auxiliary building. The shadow cast on the concrete shield building is clearly visible by the lower temperatures on the southeast and northeast walls due to the lack of solar heating during the early morning hours.

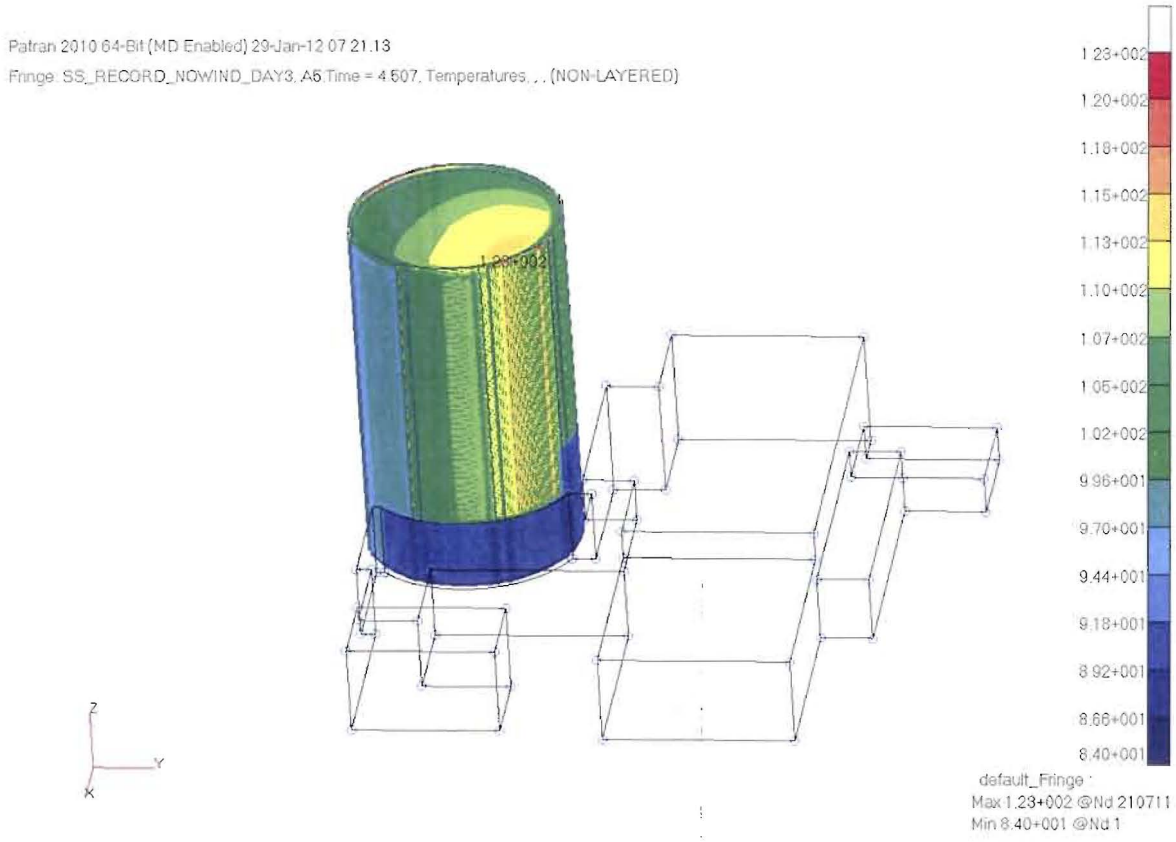

FIGURE 3. SUMMER SOLSTICE 9:00AM TEMPERATURES SHOWING THE AUXILLIARY BUILDING AND THE SHADING OF THE CONCRETE SHIELD BUILDING

In addition to solar heating, another source of radiant heating is attributable to the inner steel containment that houses the reactor. This steel containment operates at an elevated temperature that is well above the surrounding ambient air as well as the annular air. Unfortunately, no direct temperature measurements were available to determine the spatial distribution, if any, in the temperature on the exterior of the steel containment. Consequently, a uniform temperature of 120°F was used. This was the same operating temperature that was cited in the Davis-Besse thermal analysis (CALC 27 014 Shield Bldg Temp Analysis page 4, dated 12/20/2000). It was further assumed that this temperature remained invariant in response to any seasonal changes in the external ambient conditions. For the purposes of incorporating the

radiant heat transfer to the interior face of the concrete shield building, the steel containment was treated as a simple constant 120°F ambient source with a view factor of 1.0 since the entire steel containment has an unobstructed view of the interior of the concrete.

For all of the thermal conditions examined, radiation with the external ambient was included. This was especially important at night and in winter when the cooler night sky and surroundings would result in an appreciable heat loss even in the absence of any convective losses due to wind. For all radiant heat transfer effects, the typical published and CR3 measured properties for concrete were assumed. Namely, an emissivity of .93 and an absorptivity of .6 were used.

2.2 AMBIENT TEMPERATURE

The Davis-Besse facility resides at 42 degrees north latitude and as a result experiences dramatic seasonal variations in the ambient temperatures and conditions. The average and record monthly temperatures for Toledo are shown in Tables 1 and 2. These temperatures were obtained from The Weather Channel and are based upon NOAA historical records that extend back to 1870.

Month	Jan	Feb	Mar	Apr	May	Jun	Jul	Aug	Sep	Oct	Nov	Dec
High (°F)	33	38	48	61	74	83	87	84	77	64	51	38
°C	1	3	9	16	23	28	30	29	25	18	10	3
Low (°F)	22	24	33	42	53	63	68	66	59	48	38	27
°C	-5	-4	1	5	12	17	20	19	15	9	3	-3

TABLE 1. MONTHLY AVERAGE TEMPERATURES AT TOLEDO, OHIO

Month	Jan	Feb	Mar	Apr	May	Jun	Jul	Aug	Sep	Oct	Nov	Dec
Record high (°F)	68	71	82	90	99	104	106	103	101	91	80	70
°C	18	22	28	32	37	40	41	39	38	33	27	21
Record low (°F)	-16	-5	4	11	28	39	47	36	36	24	6	-13
°C	-27	-21	-16	-12	-2	3	8	2	2	-4	-14	-25

TABLE 2. MONTHLY RECORD DAYTIME TEMPERATURES AT TOLEDO, OHIO

The monthly average high and low temperatures were used to define the excursion in daily average temperatures for the winter and summer solstices and the vernal and autumn

equinoxes. The same daily variation in average temperature was also used for either record high or low conditions. An examination of the record temperatures reveals that the highest temperatures always occur in the summer and fall and the coolest in the winter and spring. To ascertain the effect of thermal stress over the maximum range of annual temperatures, thermal transient analyses were performed using the average and record high temperatures for the summer solstice and autumn equinox. Conversely, the average and record low temperatures were used for the winter solstice and vernal equinox.

To simulate the thermal lag that typically occurs in the ambient temperature relative to the solar transit, it was assumed that for the first 90 minutes after sunrise, there was no appreciable change in the ambient temperature. The sunrise temperature was set to the minimum nocturnal temperature. After the first 90 minutes, the temperature was gradually increased in a sinusoidal fashion to its daily maximum at 1:30 pm in the afternoon. The temperature was then allowed to gradually loose 90 % of the daily temperature rise at sunset. After sunset, the temperature exponentially decayed to its nocturnal minimum at 11:30pm. The temperature then remained invariant till 90 minutes after sunrise on the following morning. The average and record temperature profiles that were used are shown in Figures 4 through 7.

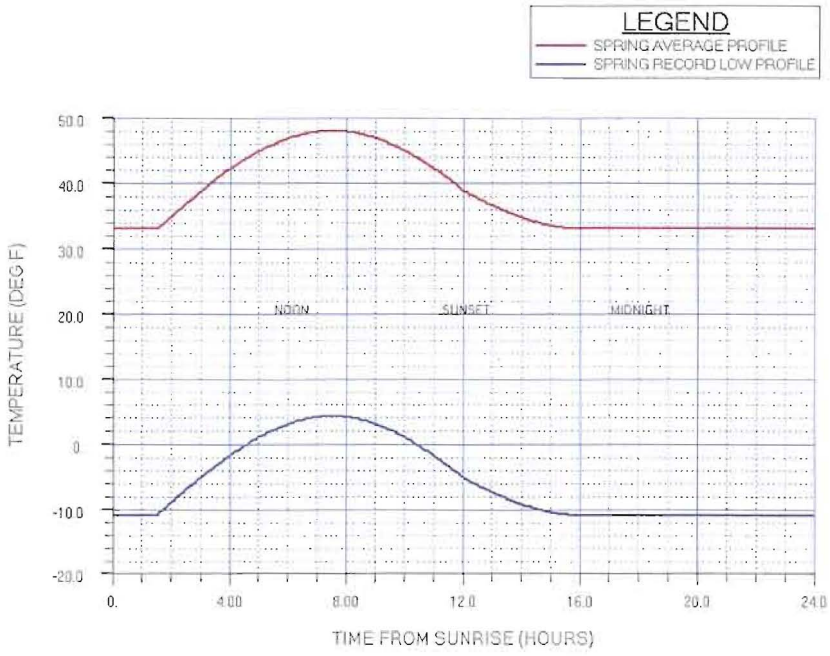

FIGURE 4. VERNAL EQUINOX AVERAGE AND RECORD LOW HOURLY TEMPERATURES

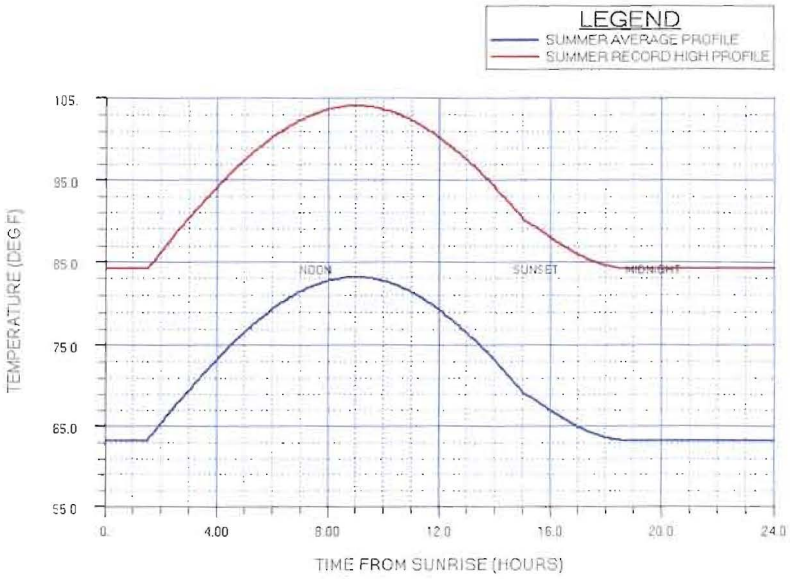

FIGURE 5. SUMMER SOLSTICE AVERAGE AND RECORD HIGH HOURLY TEMPERATURES

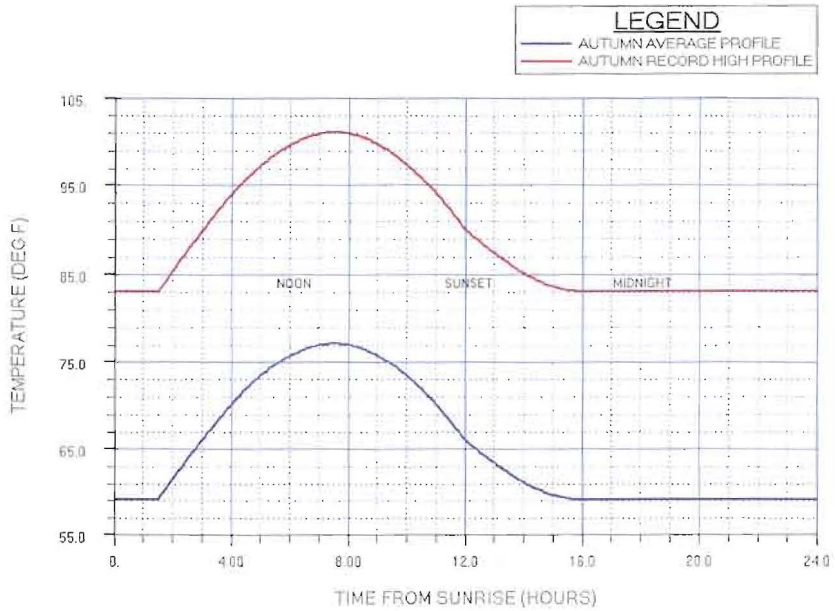

FIGURE 6. AUTUMN EQUINOX AVERAGE AND RECORD HIGH HOURLY TEMPERATURES

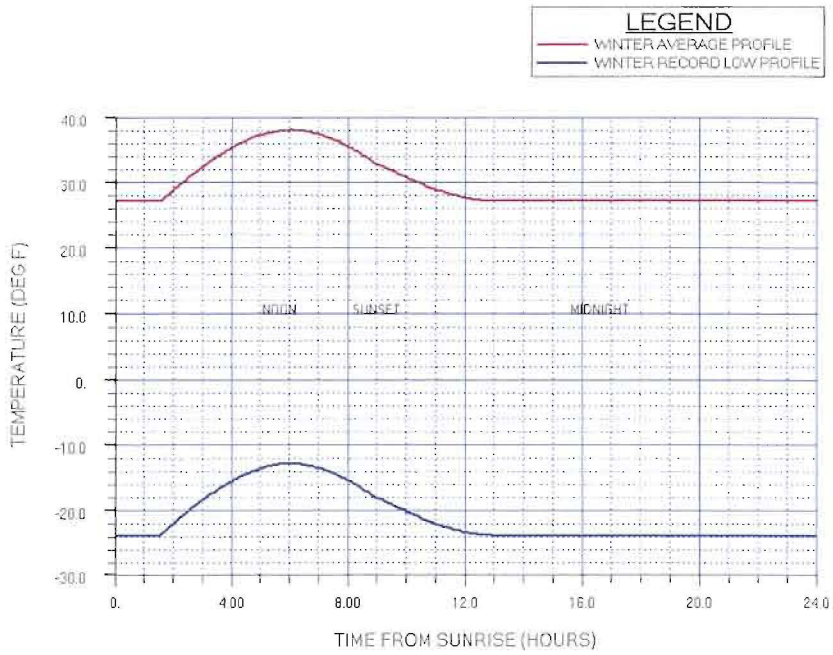

FIGURE 7. WINTER SOLSTICE AVERAGE AND RECORD HIGH HOURLY TEMPERATURES

These transient temperature profiles defined the ambient temperatures that were used to compute the heat transfer to the exterior of the concrete shield building due to either radiation, free convection or forced convection. The base of the concrete shield building was assumed to be grounded to a large thermal mass whose temperature remained constant and fixed at the daily minimum. This behavior is consistent with temperatures at deep subterranean levels which typically are unaffected by short term hourly changes in air temperature or solar heating.

2.3 CONVECTION

The principal source of heat loss from the concrete shield building is due to wind. Winds in the Toledo, Ohio and surrounding area are predominantly southwesterly as shown in Table 3, especially in the winter and spring. During the summer and fall the incidence of winds from the west and northwest increases, but they are far less intense. The average winds are quite light, with winds speeds of less than 10 mph. In comparison the record wind speeds are considerably higher, often in excess of 60 mph, and generally are from the southwest. This can be seen in Figure 8 where the record high wind speeds for the period of 1998 through 2011 complied by

NOAA are shown plotted as well as in Table 3 where the corresponding record and average wind speeds as well as wind directions are listed for the same time period.

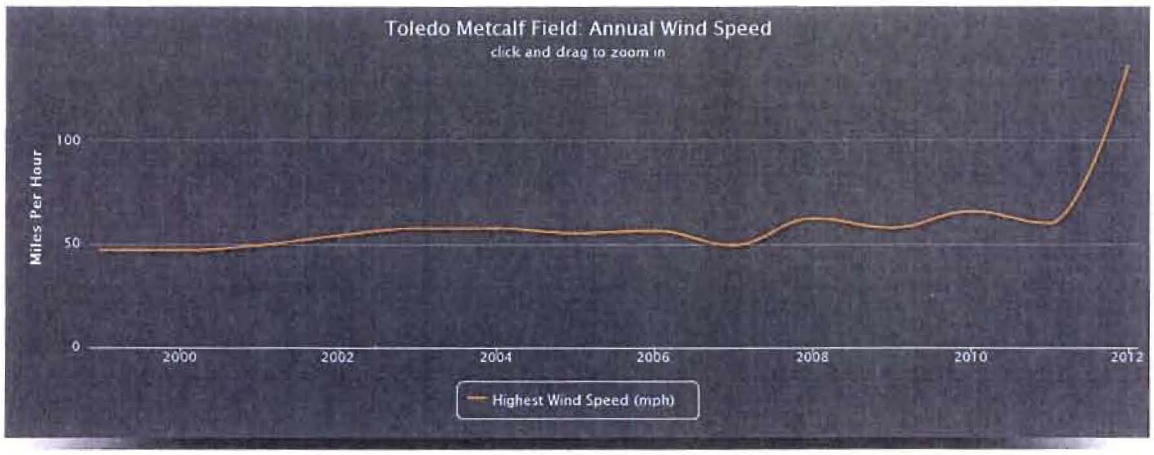

FIGURE 8. TOLEDO AVERAGE ANNUAL RECORD HIGH WIND SPEED (1998 TO 2011)

Year	High Wind Speed	Mean Avg. Wind Speed	Low Wind Speed	Prevailing Wind
2011	134.64	8.52	0.00	from the southwest
2010	59.84	8.24	0.00	from the southwest
2009	65.40	8.32	0.00	from the southwest
2008	57.54	9.09	0.00	from the southwest
2007	62.14	8.86	0.00	from the southwest
2006	49.48	9.83	0.00	from the southwest
2005	56.59	8.59	0.00	from the southwest
2004	55.24	9.21	0.00	from the southwest
2003	57.54	8.98	0.00	from the southwest
2002	57.54	9.36	0.00	from the southwest
2001	54.09	9.10	0.00	from the southwest
2000	49.48	8.98	0.00	from the southwest
1999	47.18	9.40	0.00	from the southwest
1998	47.18	8.10	0.00	from the southwest

TABLE 3. TOLEDO ANNUAL WIND DATA FOR 1998 TO 2011

The primary intent of this thermal analysis effort was to determine the maximum range in temperatures that occur during the course of the year as well as during a given season. Consequently, the decision was made to use wind speeds that were more frequently encountered but not necessarily equal to the record wind speed. Consequently, the following wind speeds and directions were chosen at each of the solstices and equinoxes (based upon historical wind data available from http://weathersource.com).

Summer Solstice

No wind with average and record high temperatures

34 mph Northwest wind with average and record high temperatures

Winter Solstice

No wind with average and record low temperatures

76 mph Southwest wind with average and record low temperatures

105 mph Southwest wind with record low temperatures (1978 Blizzard)

Autumn Equinox

No wind with average and record high temperatures

34 mph Northwest wind with average and record high temperatures

Vernal Equinox

No wind with average and record high temperatures

34 mph Southwest wind with record low temperatures

The choice of a northwest wind during the summer and autumn would minimize the convective heat loss on the southwest wall which is always the warmest. Conversely, a southwest wind would maximize the heat loss on the southwest wall. This would maximize the effect that wind has on the temperatures in the southwest wall during the course of a single year.

To maximize the effect of radiant heat loss at night as well as to better simulate the effect of large bodies of water on local wind patterns, it was assumed that winds diminished by 80 % after midnight. Typically onshore winds prevail during the day and gradually diminish after sunset. This is primarily due to the high specific heat of water which causes any large body of

water to heat up more slowly than the surrounding coastal areas during the day and cool off more slowly at night. Consequently air over the coastal land will heat up faster and rise, creating a daytime onshore convection pattern. Conversely, after sunset the gradient in air temperature over water and land will weaken and the winds will abate.

One event that was of particular interest was the 1978 blizzard which struck the Toledo area on January 25th through January 27th 1978. This blizzard is listed as one of the worst on record to hit the Great Lakes area. According to NOAA records, wind speeds in the Toledo area attained 105 mph and were from the southwest. The 850mb temperature contours for this event are shown in Figure 9 for midnight January 27, 1978. This plot reveals a temperature of approximately -20 °F in the Toledo area. This matches up very favorably with the winter solstice temperature profile shown in Figure 9 which had a -24 °F nighttime low with a -14°F daytime high. . This is approximately equal to the -16 °F daytime record low shown in Figure 9 for January. Consequently, this temperature profile was used to simulate this event. It must be emphasized that this is not the surface temperature but rather the temperature associated with elevation where the pressure is 850mb, or approximately 4500 feet. This was done since the primary mechanism for heat loss at night in the absence of any strong wind will be radiation to the night sky and not the surface air which is transparent to radiation. To ensure an accurate calculation of the radiant heat loss, it is imperative that a value for the temperature of the night sky be used which is more indicative of a higher elevation.

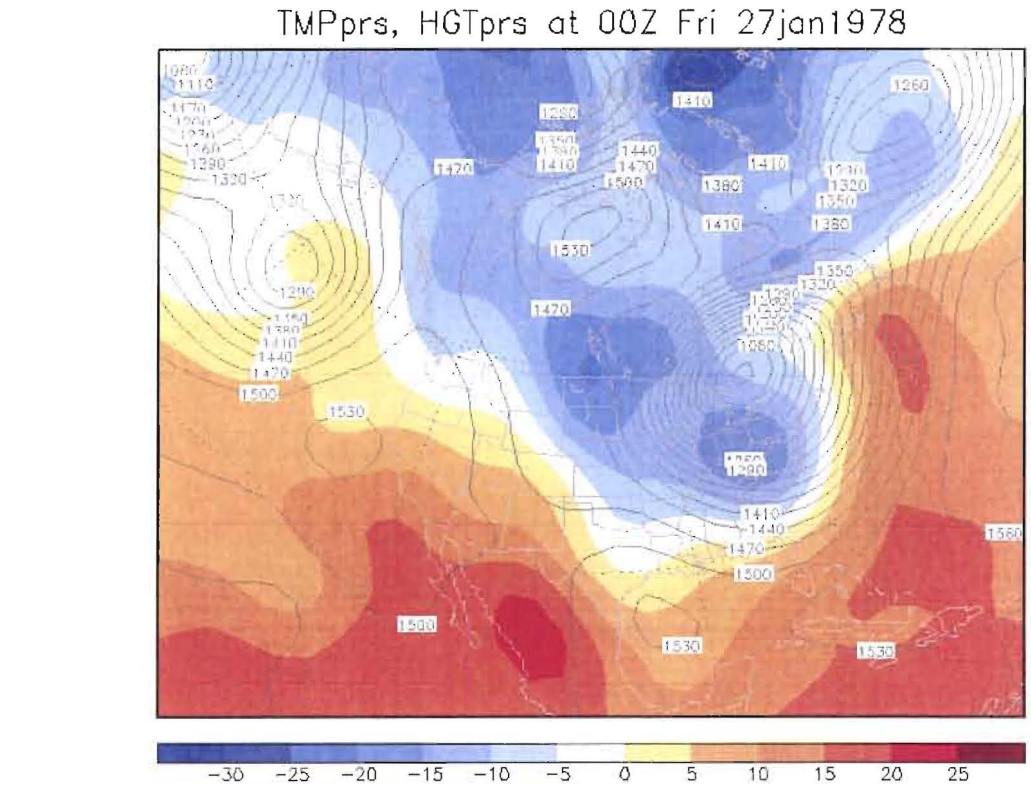

FIGURE 9. 850mb TEMPERATURES FOR JANUARY 27, 1978 (°F)

Another event of significance that was examined was the January 1977 blizzard which struck the Toledo area on January 28th and 29th. The minimum daily and noontime temperatures for January 29th are shown in Figures 10 and 11. The peak wind gust and direction recorded for this blizzard is shown in Figure 12. An examination of these figures reveals that the minimum temperature for this event was approximately -8°F and the daytime high temperature was between 10 and 20 °F. This was accompanied by peak wind gusts of 73.5 knots, or about 84mph. For the purposes of modeling this event, a -8 °F minimum temperature was assumed which occurred after midnight. A max daytime temperature of 20 °F was used which was once again assumed to occur at 1:30 pm in the afternoon. The ambient temperature was gradually decreased to its minimum at about 2:00 am and remained constant until sunrise when it gradually increased to its peak daytime value. Since the max sustained wind speed will be less than the peak gust speed, a slightly lower 76 mph southwest wind was assumed. The daily temperature profile that was used to model this blizzard is shown in Figure 13. In comparison to the winter solstice record low profile shown in Figure 7, it can be seen that this blizzard had considerably warmer temperatures.

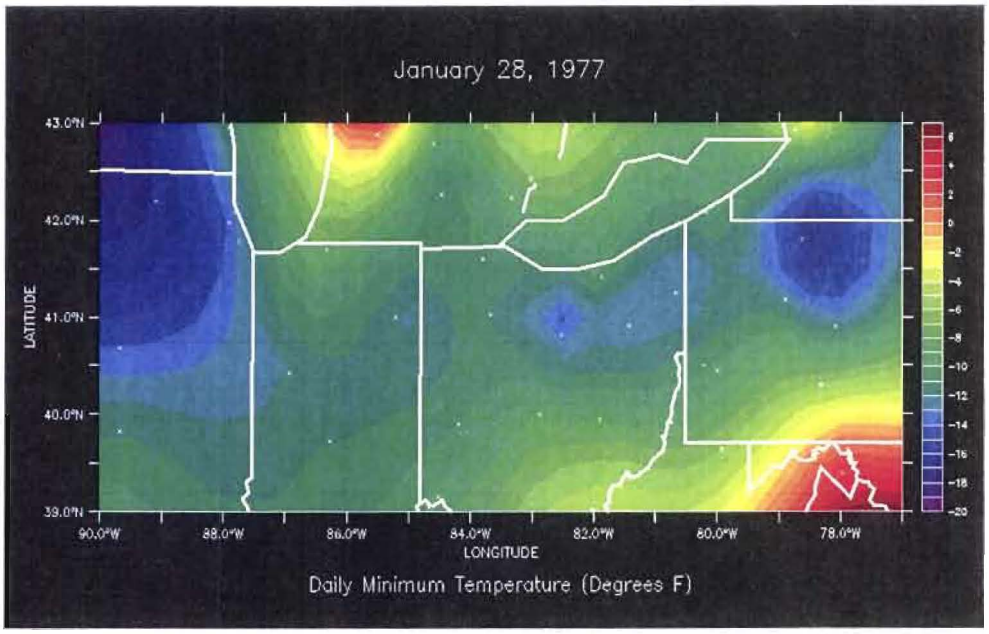

FIGURE 10. JANUARY 28, 1977 BLIZZARD MINIMUM DAILY TEMPERATURES (°F)

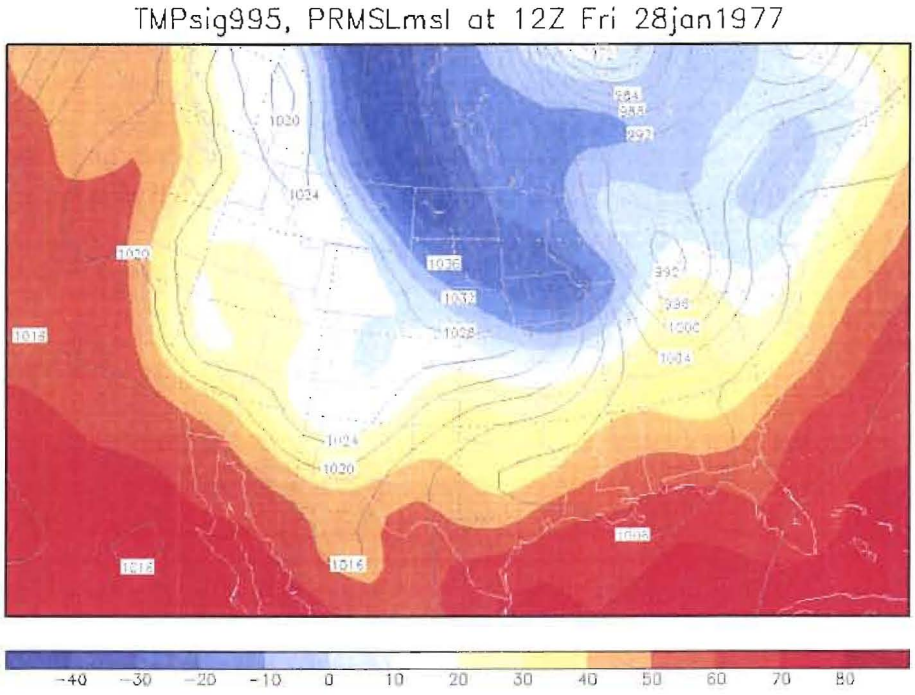

FIGURE 11. JANUARY 28, 1977 BLIZZARD NOON TEMPERATURES (°F)

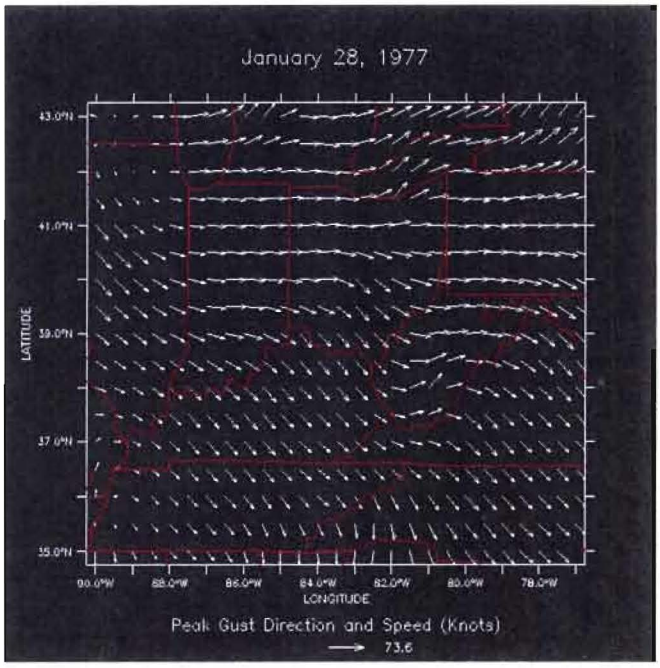

FIGURE 12. JANUARY 28, 1977 BLIZZARD PEAK WIND GUST DIRECTION AND SPEED

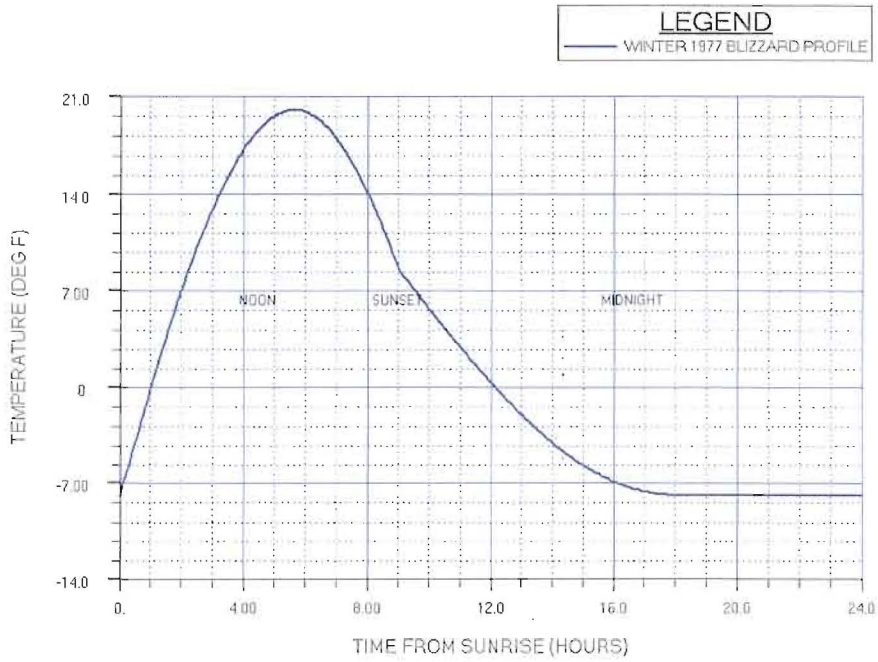

FIGURE 13. JANUARY 1977 BLIZZARD DAILY TEMPERATURE PROFILE

To determine the surface convection loss due to wind, a detailed FLUENT based computational fluid dynamic (CFD) model was generated. This model incorporated not only the concrete shield building but also the auxiliary building as well. The auxiliary building was needed since its close proximity would strongly affect the flow field. Individual analyses were run for each of the wind conditions that were being examined. FLUENT has the ability to export the surface mesh that was used for concrete shield building CFD analysis along with the corresponding pressures and convective heat transfer surface film coefficients in a standard NASTRAN bulk data format. This permitted importing the surface mesh with the pressures and heat transfer coefficients directly into the PATRAN database containing the thermal model. The pressures and convective heat transfer coefficients could then be mapped onto the exterior of the NASTRAN thermal model as well as the NASTRAN and ABAQUS [redacted] structural models using mapping routines specifically designed to accommodate dissimilar meshes. An example of the convective heat transfer coefficient that was calculated for a 105 mph southwest wind is shown plotted on the concrete shield building in Figures 14 and 15. Here the convection coefficient on the windward southwest face and the leeward northeast face are plotted. Note the drop in the magnitude of the coefficient on the leeward side as well as the swirling pattern induced by flow separation. In addition for the flute located approximately 90 degrees from the flow direction, there is a sharp augmentation in the heat transfer coefficient. This marks the onset of flow separation. The extreme non-uniformity in the heat transfer coefficient clearly illustrates the high degree of inaccuracy that would have been introduced by assuming a simple uniform value obtained from an empirically derived relationship for a cylinder subjected to simple cross flow.

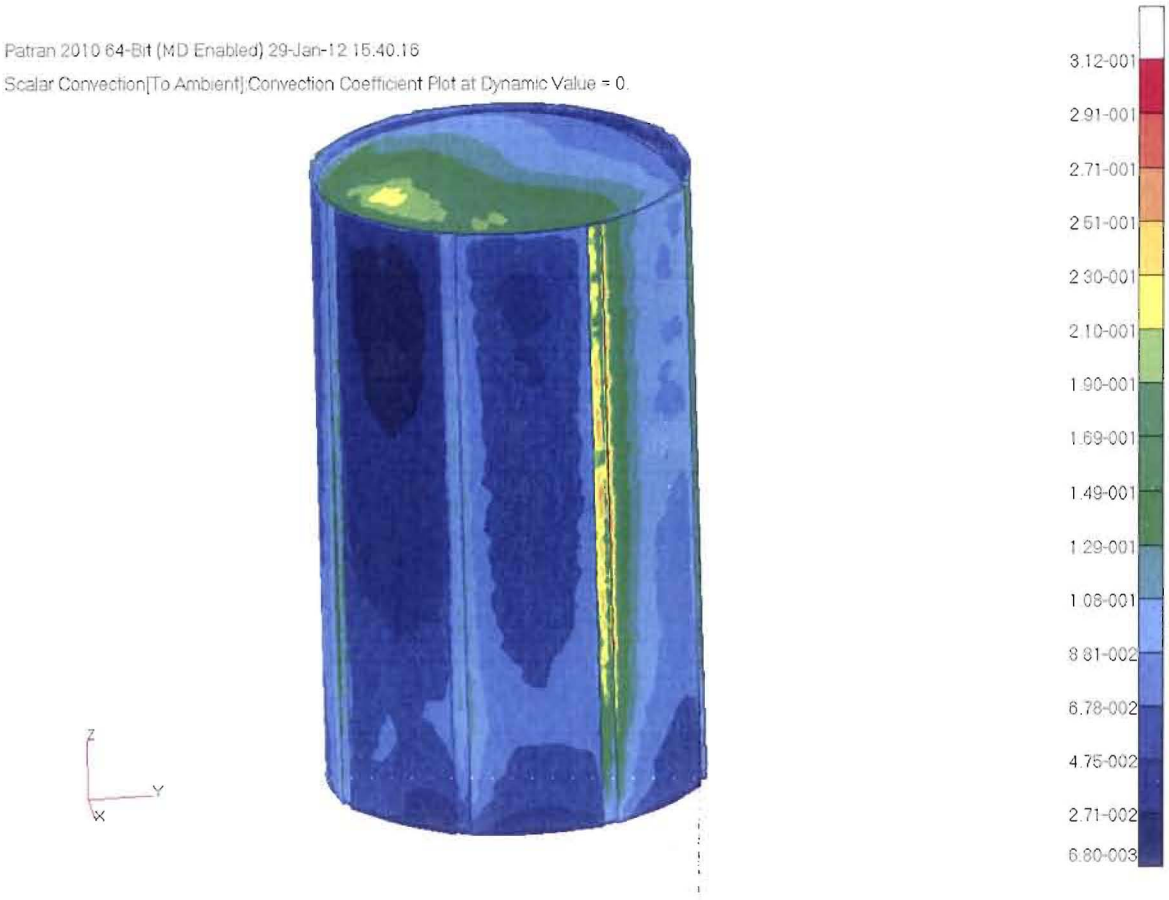

FIGURE 14. WINDWARD SIDE FORCED CONVECTION COEFFICIENT (BTU/HR-IN^2°F) FOR A 105MPH SOUTHWEST WIND

FIGURE 15. LEEWARD SIDE FORCED CONVECTION COEFFICIENT (BTU/HR-IN^2°F) FOR A 105MPH SOUTHWEST WIND

In the absence of any wind, the free convection will occur along the exterior of the concrete shield building. Using empirical derived relationships for free convection from vertical walls and horizontal plates (see Heat Transfer by J.P. Holman, 1972 McGraw-Hill), the free convective coefficients were calculated. Initial estimates were made for the difference in ambient and concrete surface temperatures in deriving these coefficients. In general, the free convection coefficients were on the order of .004 Btu/hr-in^2 °F for the dome and .006 Btu/hr-in^2 °F for the lateral sides. The small magnitude of these coefficients resulted in only a minor amount of heat transfer to and from the exterior of the concrete shield building. Rather radiation heat transfer effects dominated in conditions of little or no wind. Similarly, the air flow in the interior annular air passage between the outer concrete shield building and the inner steel containment was included, but had little if any effect on the interior temperatures of the concrete. Based upon a 55,000 cfm flow rate (Bechtel CALC 68-011r1, January 1968) and an approximate 1900 ft^2 cross-sectional annular area (based upon a 834 and 780 outer and inner radius) resulted in an average flow speed of only .48 ft/sec. Using the properties for 80 °F air, this gave a convective heat transfer coefficient of only .00054 Btu/hr-in^2 °F. Once again the

radiant heat transfer from the 120 °F inner steel containment would dominate and dictate the temperature at the inner face of the concrete shield building.

2.4 THERMAL PROPERTIES

Initially the Crystal River CR3 measured thermal properties were used. These properties are summarized in Table 4. These properties compared closely with the published generic properties for concrete. Based upon these thermal properties, transient thermal analyses were conducted for both the solstices and equinoxes using the average and record temperature profiles with and without wind. The time of day when temperatures peaked on the southwest wall were subsequently mapped onto both the NASTRAN and ABAQUS [redacted] structural models as well as selected detailed ABAQUS [redacted] featuring a highly refined mesh to improve stress recovery. These temperatures were then used to conduct thermo-structural analyses to determine the radial stress in the outer concrete shield building. Based upon these initial analyses, those ambient conditions were identified that produced the highest tensile radial stresses in the southwest wall of the concrete shield building. [redacted]

[redacted]

From "Davis-Besse" Drop Box "Material_Properties_Comparision.xls" dated 10/31/2011

Davis-Besse Concrete Thermal Data per Dr. Xi

Temperature	Density, w	Conductivity, K	Diffusivity, α	Specific Heat, c_p	Emissivity, ε	Mechanical Properties Davis-Besse Calc C-CSS-099.20-054 r0 Thermal Expansion	Young's Modulus,E	Poisson's Ratio, v
(°C)	(kg/m³)	(W/m-°K)	(m^2/sec) x 10^6	KJ/kg-°K		per °C		
43.0	2400.73	1.920	0.8597	0.928	0.93	6.80E-06	n/a	n/a
(°F)	(lb/in³)	(Btu/hr-in-°F)	(in^2/hr)	Btu/lb-°F		in/in/°F (x10^{-6})	lbs/in^2 (x10^6)	
109.4	0.0867	0.092	4.797	0.222	0.93	3.80	3.60	0.25

$\alpha = K/(w^*c_p)$ (1.) Assumed Brick/Mortar

Eckert & Drake Table A-10

Generic Steel - Rebar & Liner

Eckert & Drake, "Heat & Mass Transfer"

Temperature	Density, w	Conductivity, K	Diffusivity, α	Specific Heat, c_p	Emissivity, ε	Mechanical Properties Davis-Besse Calc C-CSS-099.20-054 r0 Thermal Expansion	Young's Modulus,E	Poisson's Ratio, v
(°F)	(lb/in³)	(Btu/hr-in-°F)	(in^2/hr)	Btu/lb-°F		in/in/°F (x10^{-6})	lbs/in^2 (x10^6)	
80.0	0.282	2.670	86.074	0.110	0.25	6.80	29.00	0.30

$\alpha = K/(w^*c_p)$ (2.) Assumed LCS (3.) CR3 Highlighted

Note: When material density is in Mass Units $c_p = c_p * 386.4$ in/sec²

Stefan-Boltzmann Constant for Radiation

1.190E-11 Btu/hr-in²-°R⁴

TABLE 4. INITIALLY ASSUMED DAVIS-BESSE THERMAL PROPERTIES

During the later phases of this project, the actual thermal properties for the Davis-Besse concrete were measured. These are shown in Table 5. Compared to the initial CR3 based properties, the new properties were considerably different and atypical of concrete. The thermal conductivity and specific heat were considerably higher and exhibited an increased sensitivity to temperature. The higher conductivity would result in a greater depth of heat penetration characterized by less steep thermal gradients through the wall of the concrete shield building. The higher specific heat would result in a lower rate of temperature change. This was reflected in subsequent thermal analyses conducted with these revised properties. With the initial CR3 properties, repetitive 24 hourly daily temperatures could be achieved in about 2 days after beginning from a uniform soak temperature equal to the seasonal minimum. In comparison, with the revised properties, it took nearly 3 days to achieve repetitive 24 hours temperatures.

Material Properties for Davis-Besse Overall Global Finite Element Model [FEM] Idealizations Revised 12 Jan 2012

USBR Test Values per e-mail memorandum 11 January 2012

	Thermal Properties					*Mechanical Properties*			*Failure Criteria*	
	29-Nov-11	11-Jan-12	11-Jan-12	11-Jan-12		11-Jan-12	9-Dec-11	29-Nov-11	12-Jan-12	12-Jan-12
Temperature	Density, w[a,1]	Conductivity, K[b,1]	Diffusivity, α[b,1]	Specific Heat, c_p	[2,1] Emissivity, ε	Thermal Expansion, Υ	Young's Modulus, E	Poisson's Ratio, ν[a,1]	Failure Stress, P_f	Fracture Energy, G_f
(°F)	(lb/in³)	(Btu/hr-in-°F)	(in²/hr)	Btu/lb-°F[b,1]		in/in/°F (x10⁻⁶)	lbs/in² (x10⁶)		(lbs/in²)	(lbs/in)
≤ 50	0.0868	0.308	7.632	0.478	0.93	5.20	4.34	0.20	600	0.54
100	"	0.243	6.624	0.428	"	"	"	"	"	"
≥ 150	"	0.185	5.760	0.378	"	"	"	"	"	"
	[a.] 150 lb/ft³ CR3 Legacy Value per Dr. Xi	[b.] Conversion to inch units	α = K/(w*c_p)			USBR e-mail note dated 11 Jan 12	f_u = 7,500 psi Ave Telecom 9 Dec 11	Legacy Value per Dr. Xi		

Generic Steel - Rebar & Inner Steel Containment

Eckert & Drake, "Heat & Mass Transfer"

	Thermal Properties					*Mechanical Properties*		
Temperature	Density, w	Conductivity, K	Diffusivity, α	Specific Heat, c_p	[2,1] Emissivity, ε	[3,1] Thermal Expansion	Young's Modulus, E	Poisson's Ratio, ν
(°F)	(lb/in³)	(Btu/hr-in-°F)	(in²/hr)	Btu/lb-°F[3,1]		in/in/°F (x10⁻⁶)	lbs/in² (x10⁶)	
80	0.282	2.670	86.074	0.110	0.25	6.80	29.00	0.30
			α = K/(w*c_p)		[2.] Assumed LCS	[3.] Legacy CR3		

Table 1. Concrete & Steel

4.] Note: When material density ω in Mass Units c_p = c_p * 386.4 in/sec²

Stefan-Boltzmann Constant for Radiation 1.190E-11 Btu/hr-in²-°R⁴

Notes on Radiation used on Transient Thermal Analysis

For thermal transient heat transfer models radiation between the steel and the concrete is treated as a simple radiation to ambient temperature of 120°F. It was assumed the steel temp was invariant. The view factor was set to 1 and the absorptivity of the concrete was set to 0.6. This avoids iterate on the element by element view factor which speeds up the transient analysis. Also this avoids having to consider the properties of the steel for radiation.

Note: Material property values for submodels representative of specific regions may reflect localized measurements.

TABLE 5. FINAL MEASURED DAVIS-BESSE THERMAL PROPERTIES

Thermal analyses were repeated using the measured properties. A temperature dependent conductivity and specific heat were substituted that matched the measured data. For temperatures less than or equal to 50 °F , the lowest temperature where measurements were made, constant values were used equal to the 50 °F values. Similarly, the 250 °F values were used for all temperatures greater than or equal to 250 °F. Rather than rerun all of the original cases, only those previously identified six cases were rerun with the new properties where tensile radial stresses were greatest. The winter solstice with a 105mph wind and record low temperatures as well as with no wind and average temperatures were also rerun. These last two runs corresponded to the 1978 severe blizzard conditions and the warmest typical winter conditions where freeze/thaw could occur daily. An additional run was also made of the January 1977 blizzard, the second worst blizzard on record in the Toledo area. This blizzard was characterized by high winds but significantly warmer temperatures compared to 1978 event. Initially, all winter runs produced compressive radial stresses when the expansion effects due to the freezing of entrapped water were ignored. The intent of the winter runs was to determine if the compressive radial stresses were eliminated with the new concrete properties.

To facilitate the determination of the time of day when radial stresses maximized, a highly detailed NASTRAN plane strain model was generated of the entire cross-section of the concrete shield building that corresponded to an elevation 8202 inches. This model featured a highly refined meshed that greatly improved the recovery of stresses. Initial thermo-structural analyses conducted with this model revealed the presence of local maxima in the radial stress in the vicinity of the shoulders on the southwest wall where cracking was observed. Consequently this provided confidence that the plane strain model could be used to determine when radial stresses peaked.

Temperatures that were obtained from the 3D transient thermal analysis model were mapped onto the plane strain model at 1 hour intervals that spanned an entire day beginning and ending at sunrise. Since this model used a plane strain formulation, it could be quickly run, typically less than a few minutes. The resultant time when the radial stresses peaked was determined and the corresponding temperatures were subsequently mapped onto the ABAQUS and NASTRAN [redacted] models to determine the radial stresses in the concrete shield building.

Subsequent thermo-structural analyses were performed using a temperature dependent CTE that attempted to simulate the expansion due to freezing of entrapped moisture in the concrete. For these analyses, a negative CTE was assigned at those temperatures where the freezing of water and expansion of ice would be the most pronounced. Results performed with freezing effects indicated the presence of high radial stresses located in regions adjacent to the shoulders where cracking was observed. This condition occurred when the temperatures associated with both the 1977 and 1978 blizzard were used with the revised thermal properties. This insinuated that the observed cracking may have been a product of the low temperatures that accompanied these events coupled with high moisture content in the concrete.

To ascertain if existing cracks would have a propensity to propagate, the NASTRAN [redacted] model was modified to incorporate a 30 x 30 foot crack located just below the ring girder and that spanned a flute located on the southwest wall where cracking was observed. Additional thermal analyses were performed with this cracked model using those conditions that produced the highest and lowest temperatures: [redacted] The temperatures obtained from these analyses were mapped onto the cracked NASTRAN [redacted] model in order to ascertain if the stresses induced by thermal effects at the crack tip were sufficient to induce further crack propagation.

Exhibit 66: Toledo 1978 Weather

1978 TOLEDO BLIZZARD WEATHER SUMMARY

The blizzard of 1978 occurred on January 25-27, 1978 and has been classified as the storm of the century for the Great Lakes and Ohio Valley. This storm was characterized by severe blizzard conditions with 12 inches of snowfall reported at Toledo and 22 inches at Saginaw, Michigan. Constant wind speeds of 45 mph with gusts to 75 mph were recorded in Toledo. Larger snow amounts and higher winds speeds in excess of 105 mph were recorded just west of Toledo.

This blizzard was characterized by a rapid drop in temperature. This can be seen in Figures 1 through 6 where the surface temperatures for this event are shown beginning at 12 noon on January 25th and ending at midnight January 27$^{th.}$. An examination of these temperature maps reveals that as late as 6:00pm on January 25th temperatures were at the seasonal daily average of approximately 30 to 40°F. However, by midnight the temperatures had fallen to -5° F in the Toledo area. Daily temperatures were below 20° F by noon the next day. Surface temperatures continued to drop to near zero degrees by midnight on January 27th.

The corresponding 850mb high altitude temperature contours show an even more dramatic decline in temperature. These are shown in Figures 7 through 10. These temperature contour maps reveal that just prior to the onset of the blizzard, the 850mb temperatures were between 0 and -5 ° F. However, by noon on January 26th, the 850mb temperatures were less than -10° F and approximately -15 to -20° F by midnight on January 27th. The 850mb are of special significance, especially with regards to radiant heat transfer at night. In the absence of any appreciable cloud cover, any solar heating will be radiated to the distant night sky. The 850mb temperatures are more indicative of this temperature, not the surface air temperature. Conversely, in the presence of heavy low lying cloud cover, heat will be radiated to the sky at a temperature that is more indicative of the surface temperature.

Near the winter solstice, the sun in the Toledo area is very low in the sky, more than 60 degrees from vertical at noon. In addition, during winter at the Toledo latitude, the solar flux is reduced more than fourfold from the summer solstice value. Coupled with this is amount of daylight, approximately nine hours of which the southwest face of the shield building receives less than six hours of direct sunlight. In the presence of a 105mph southwesterly wind as recorded during the 1978 blizzard, the majority of the solar heat would be convected away. The peak temperatures on the exterior of the southwest face of the shield building would increase

slightly during the day. Instead the exterior temperatures would be defined more by the temperature of the night sky since the primary mechanism for heat loss would be radiation.

For the purposes of assessing the worst case effects of thermal gradients in the absence of any freezing and expansion of entrained moisture in the concrete, an ambient temperature profile was selected that was more indicative of the 850mb temperatures recorded toward the peak of the blizzard late on January 26th and early January 27th. For this reason an ambient temperature profile was chosen that had a -14° F daytime max and a -24° F nighttime minimum. This would be the same as assuming a clear sky prevailed at night. This would necessarily make this analysis extremely conservative with regards to just thermal gradient effects.

Had the night sky been extremely cloudy, the ambient temperatures as well as the exterior concrete temperatures would have been significantly warmer and more representative of the surface air temperatures that were recorded for this event. Since radiation at night would still dominate, the peak temperatures in the exterior of the concrete would be approximately 15 to 20° F warmer. In the presence of entrained moisture and its expansion, selecting this higher temperature would make any thermal stress analysis more conservative.

Unfortunately, the amount of precise meteorological data available from NOAA, especially with regards to hourly cloud cover, is somewhat sparse for this blizzard. Consequently, the decision was made to choose those ambient conditions that would produce the worst case results when assessing thermal effects.

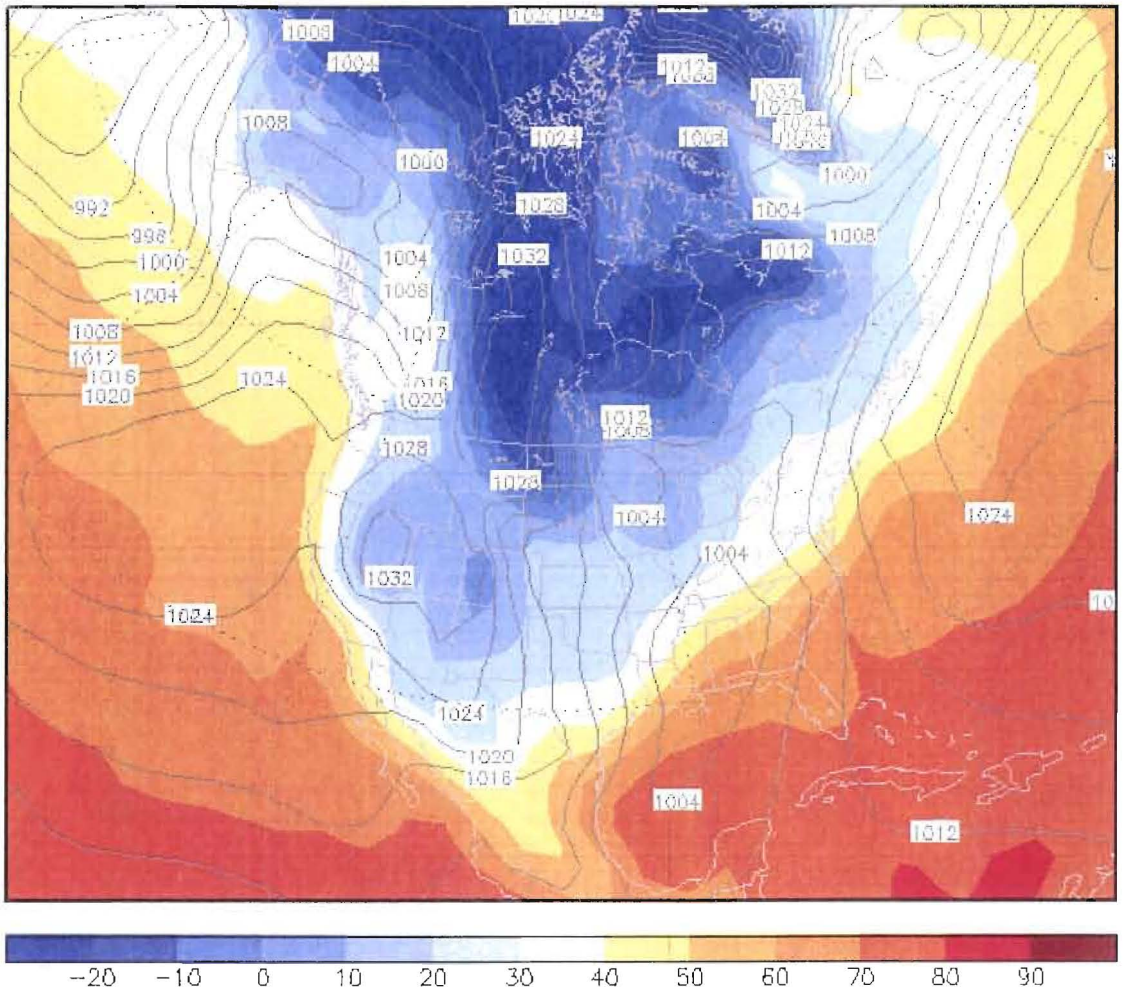

FIGURE 1: JANUARY 25, 1978 12:00pm SURFACE AIR TEMPERATURES

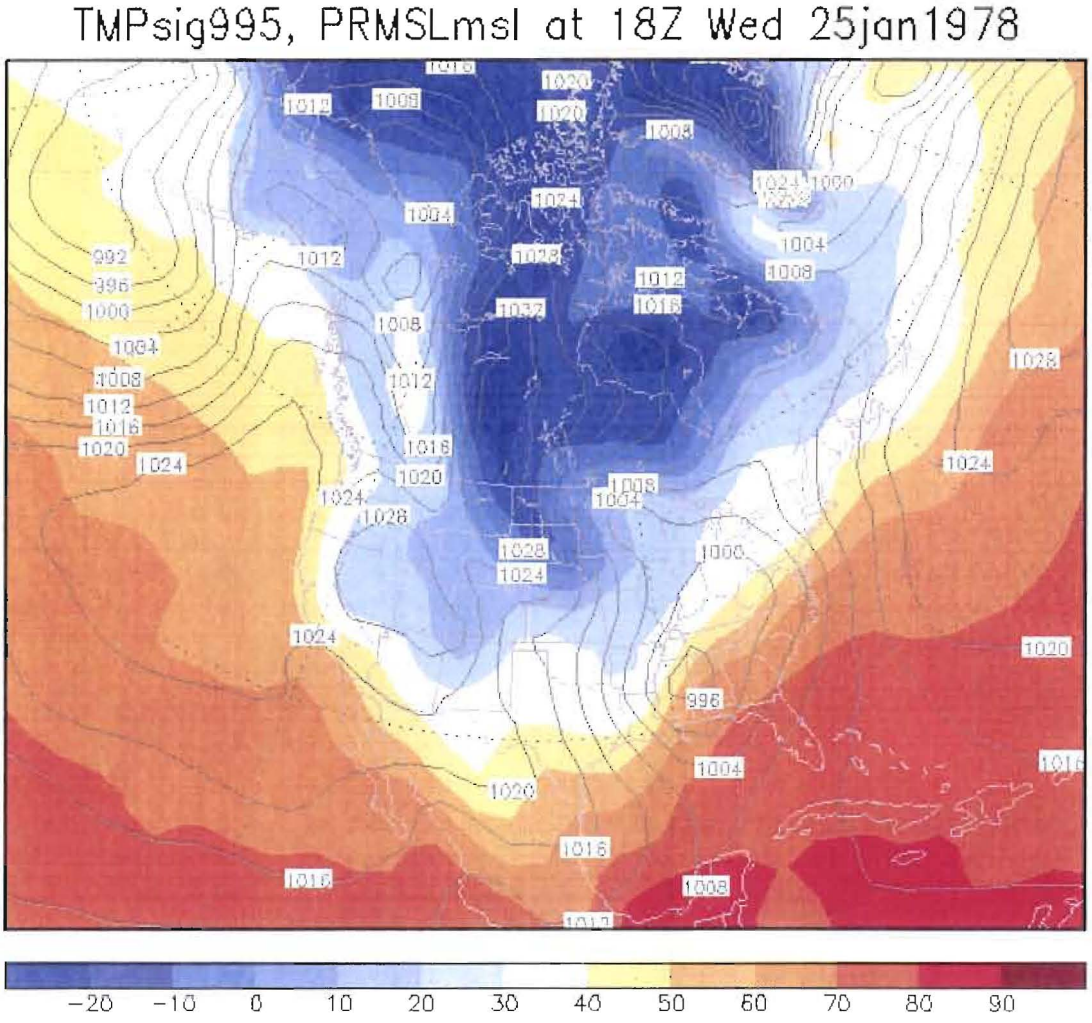

FIGURE 2: JANUARY 25, 1978 6:00pm SURFACE AIR TEMPERATURES

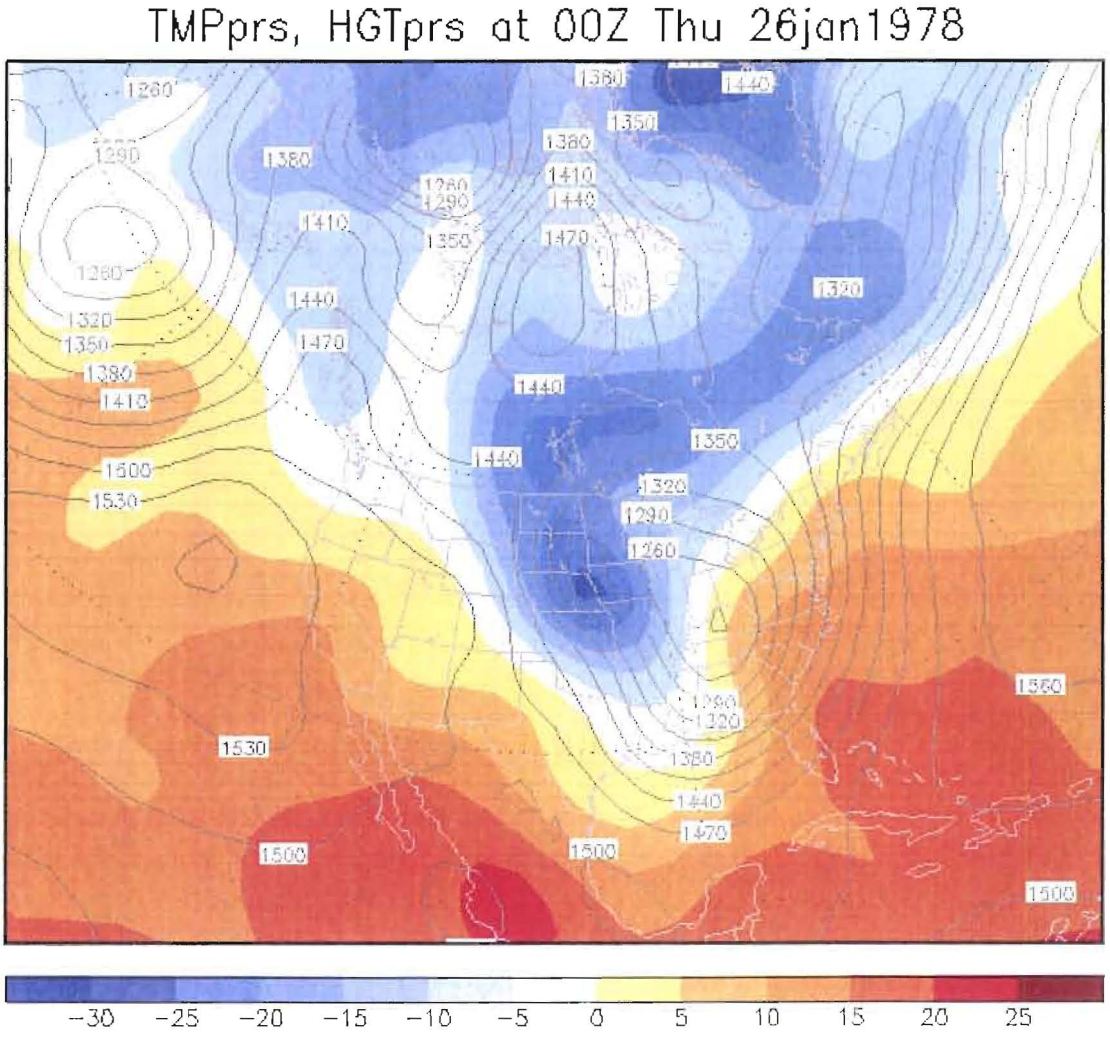

FIGURE 3: JANUARY 26, 1978 12:00am SURFACE AIR TEMPERATURES

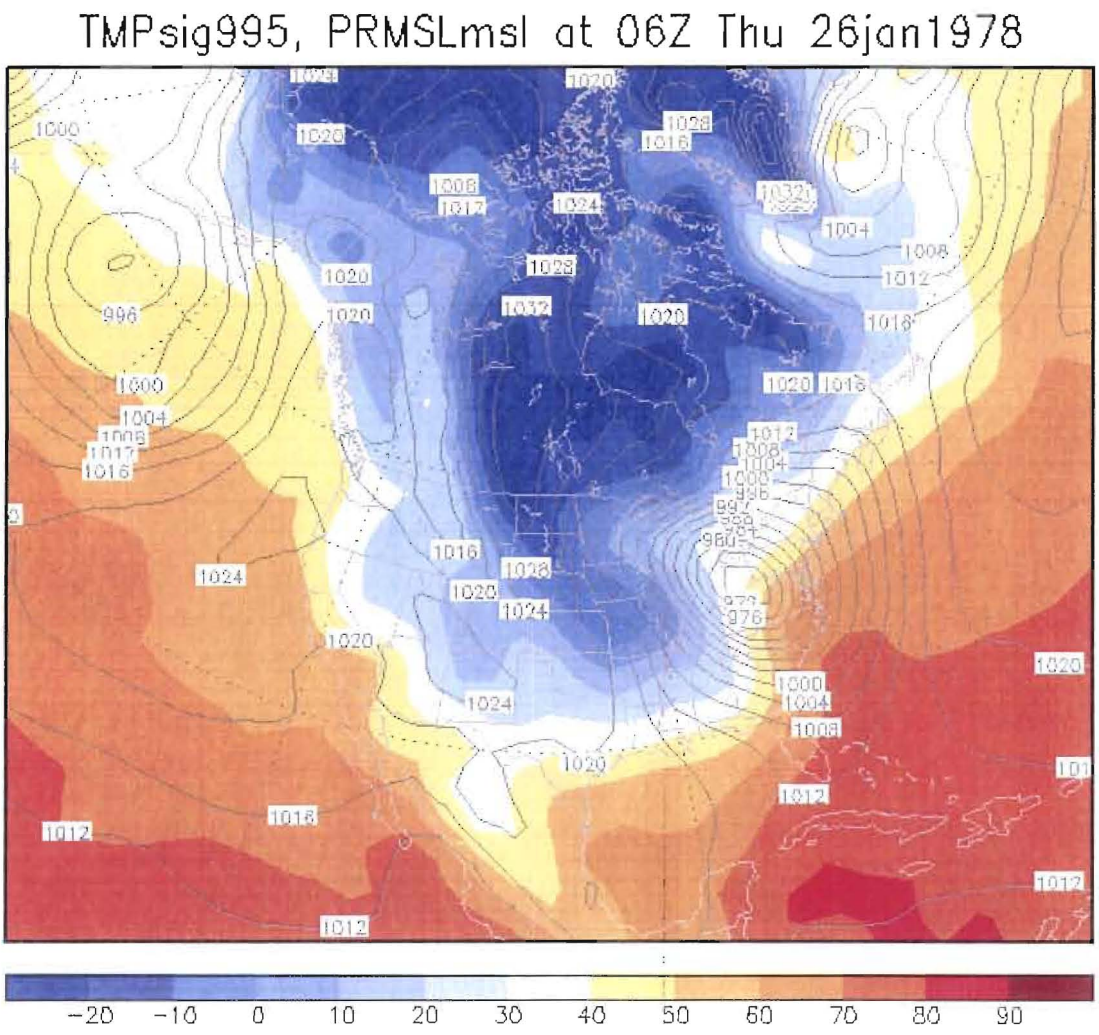

FIGURE 4: JANUARY 26, 1978 6:00am SURFACE AIR TEMPERATURES

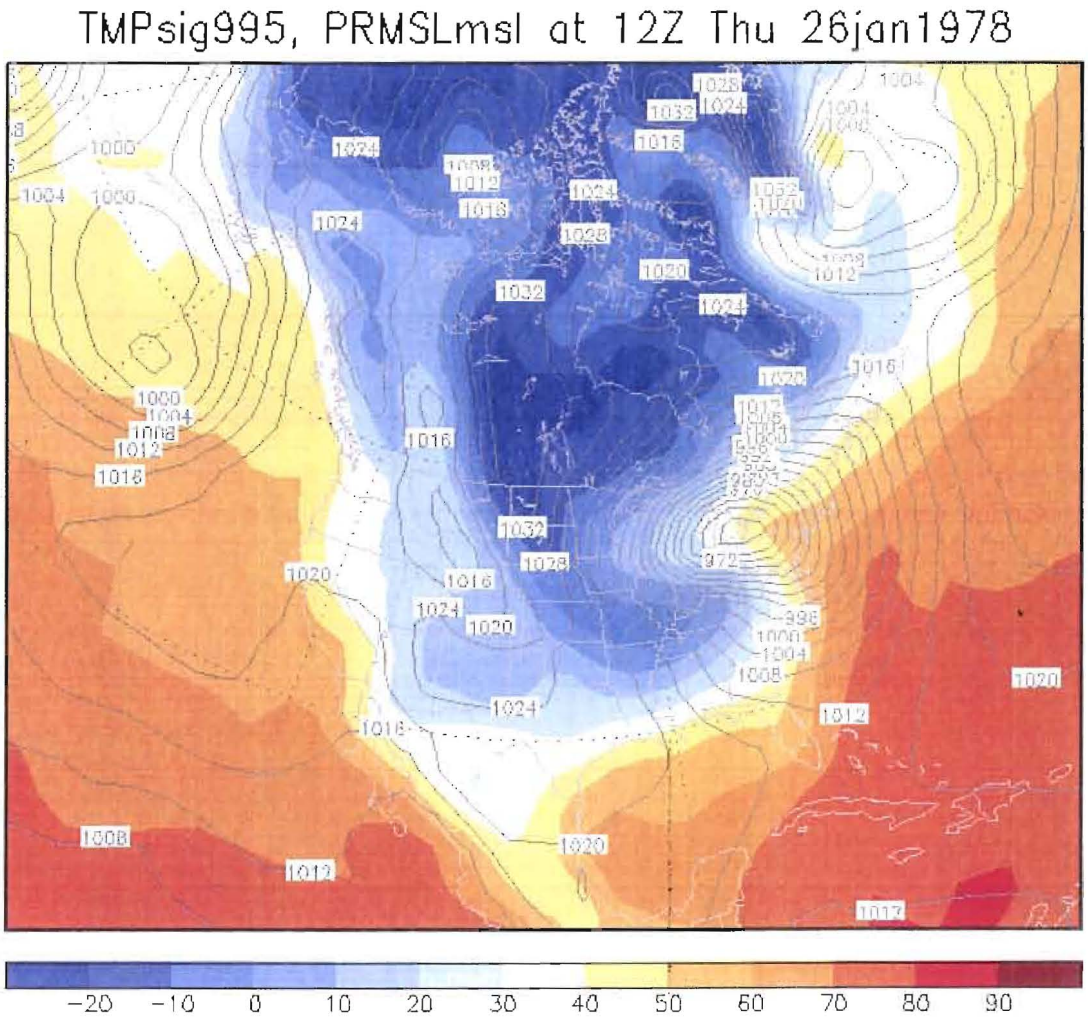

FIGURE 5: JANUARY 26, 1978 12:00pm SURFACE AIR TEMPERATURES

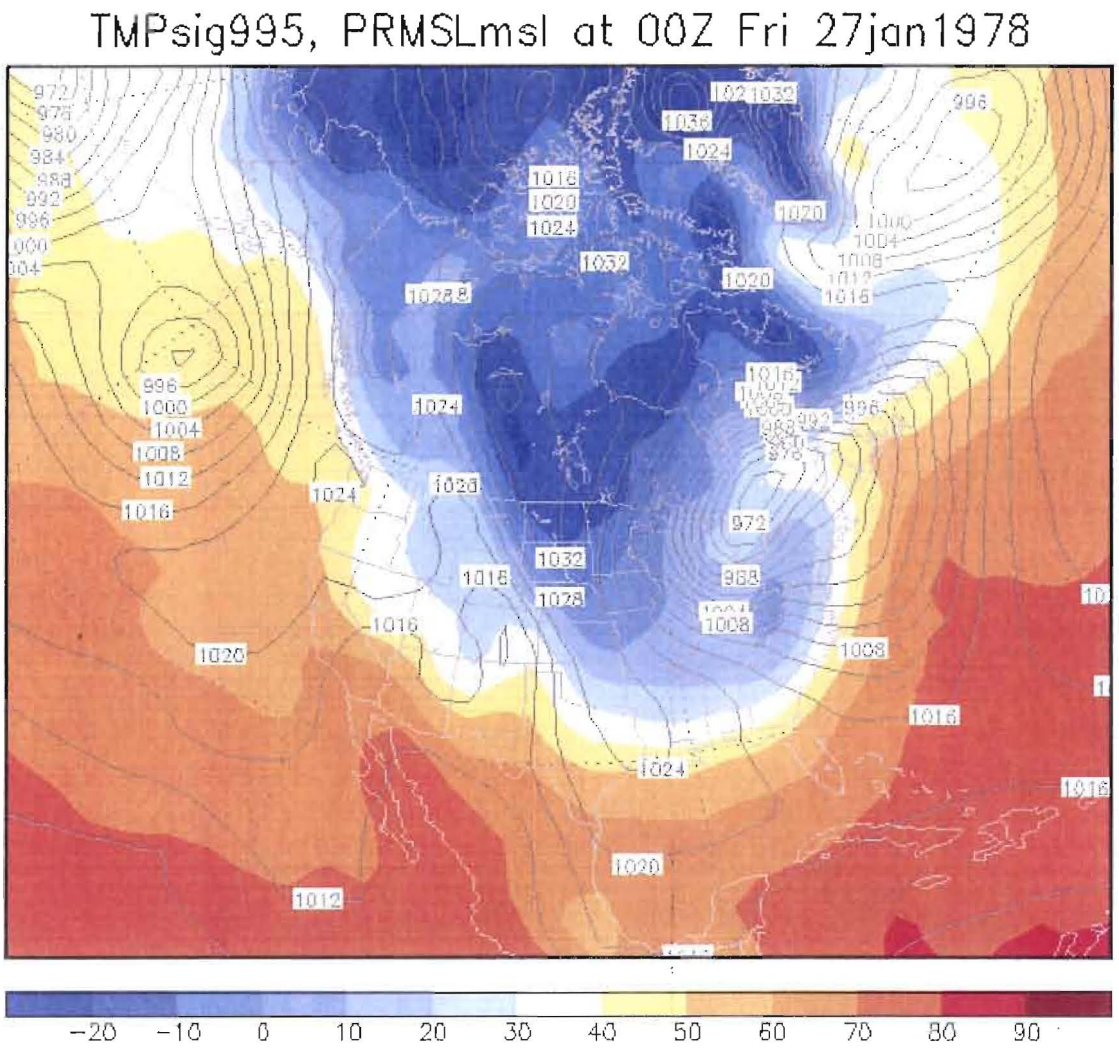

FIGURE 6: JANUARY 27, 1978 12:00am SURFACE AIR TEMPERATURES

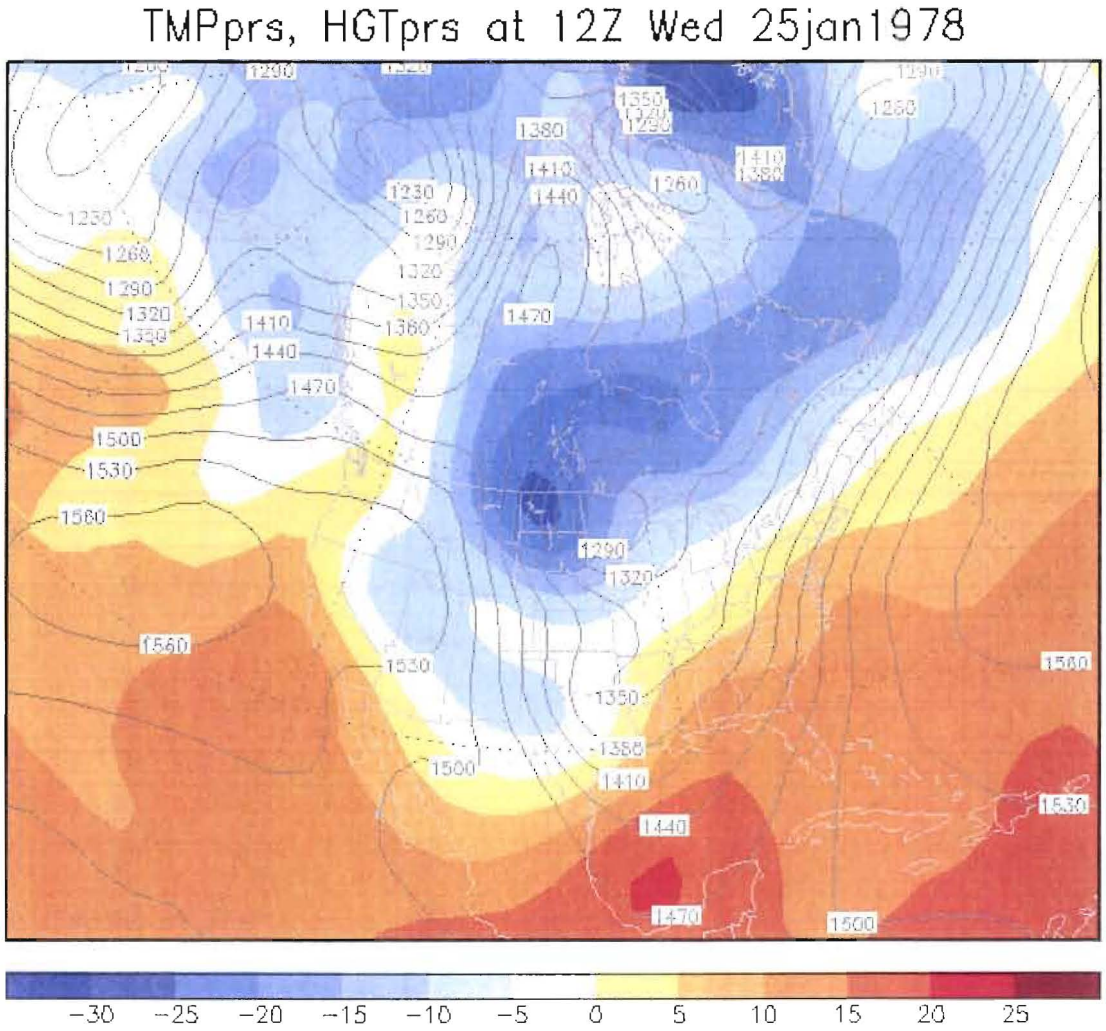

FIGURE 7: JANUARY 25, 1978 12:00pm 850mb AIR TEMPERATURES

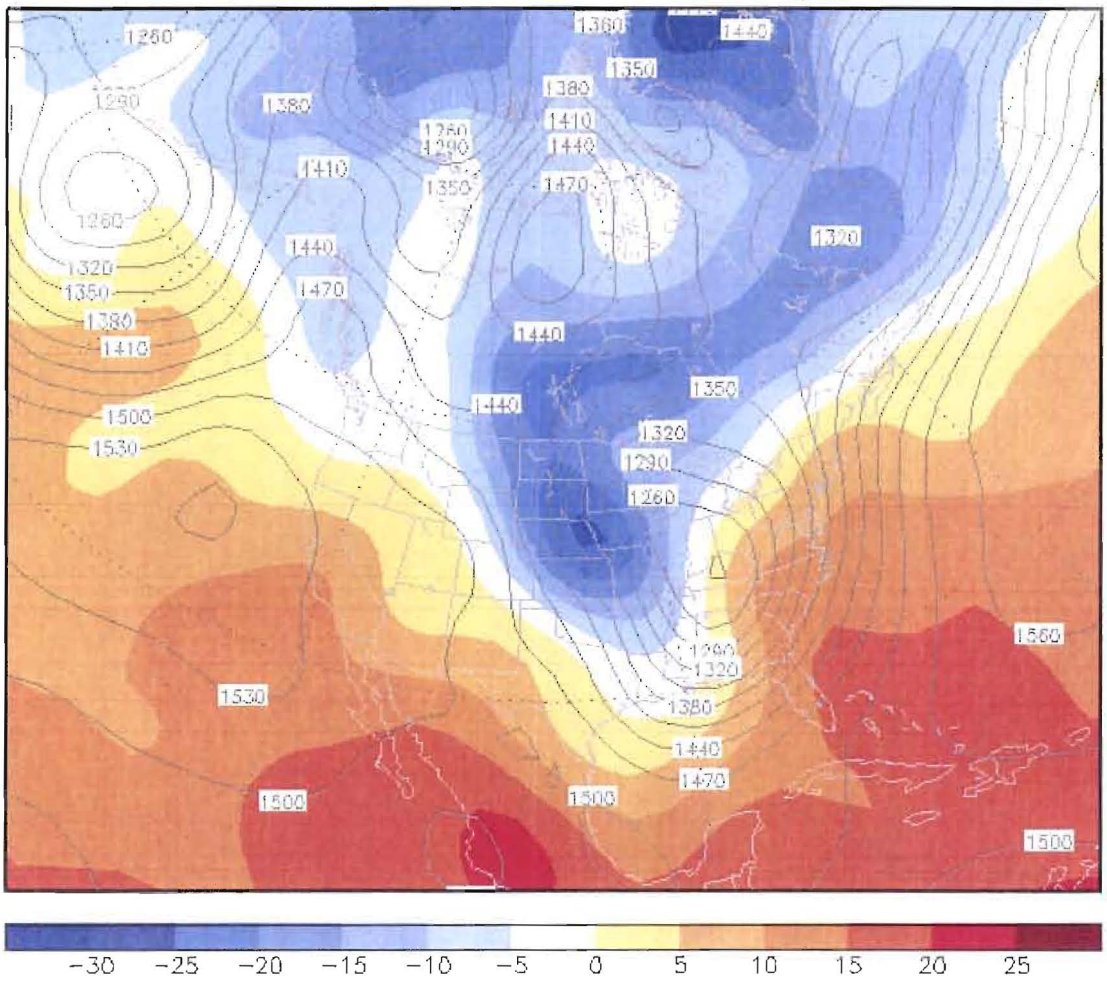

FIGURE 8: JANUARY 26, 1978 12:00am 850mb AIR TEMPERATURES

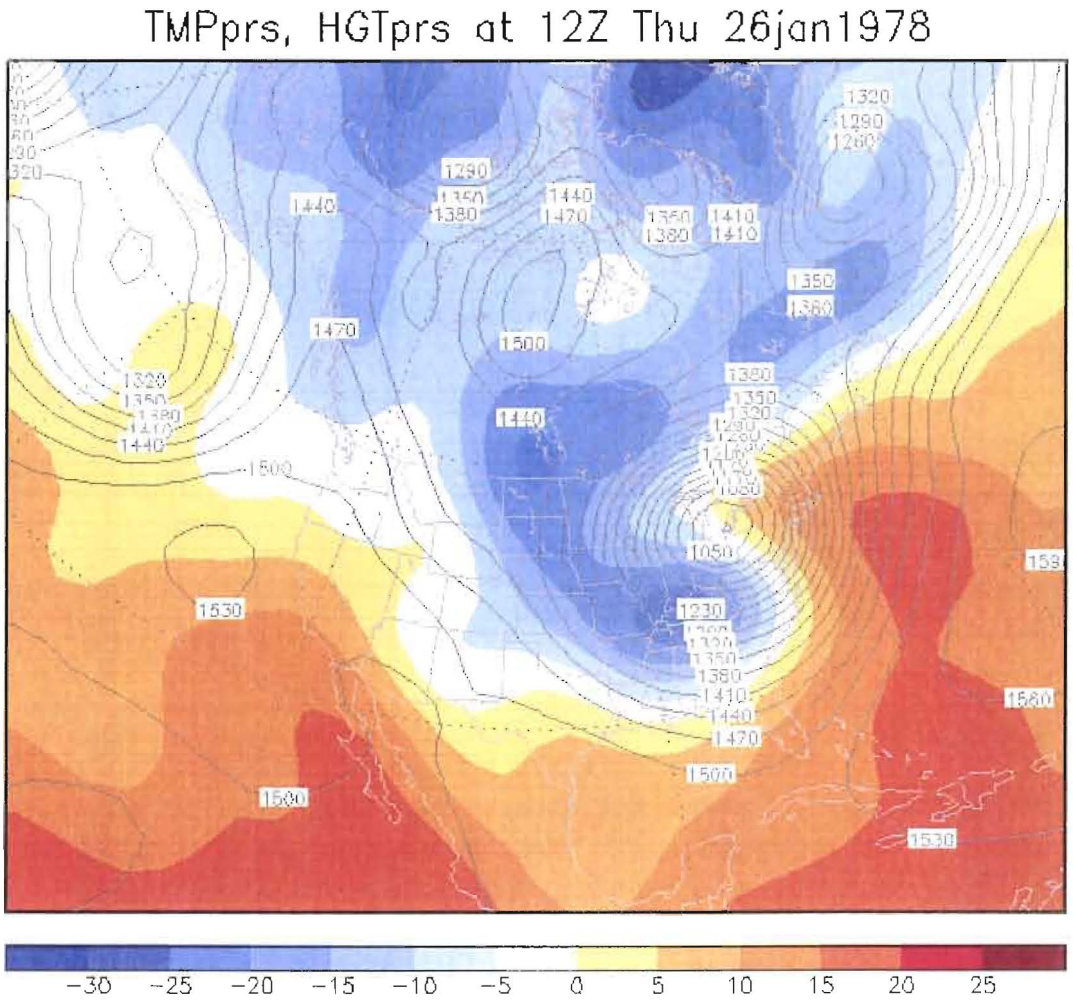

FIGURE 9: JANUARY 26, 1978 12:00pm 850mb AIR TEMPERATURES

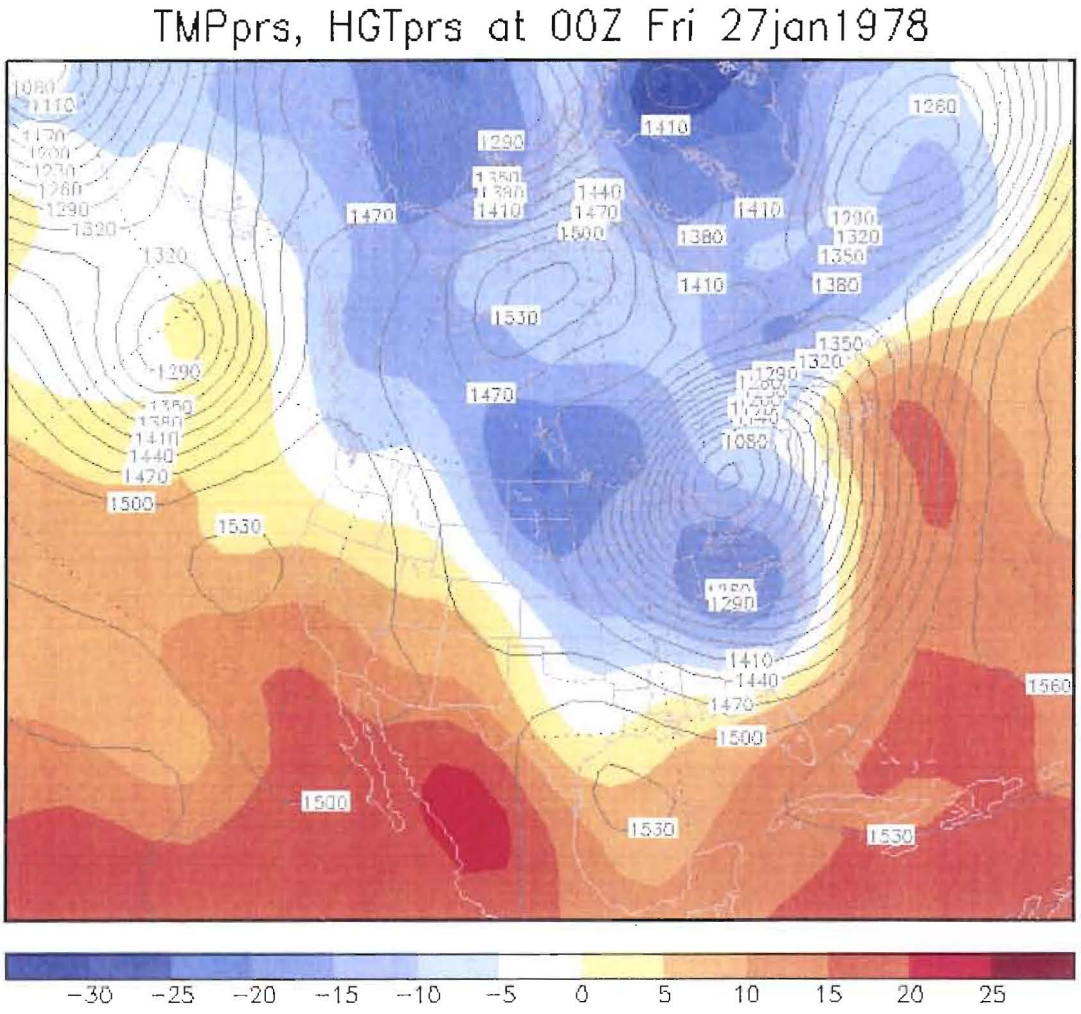

FIGURE 10: JANUARY 27, 1978 12:00am 850mb AIR TEMPERATURES

Exhibit 67: CFD Analysis Summary

DAVIS-BESSE SHIELD BUILDING [redacted] ANALYSIS

The [redacted] performed for this report includes:

- No surrounding buildings
  - 34mph from the Northwest (summer)
  - 34mph from the Southwest (winter)
  - 72mph from the Southwest (winter)
- Surrounding buildings
  - 34mph from the Northwest (summer)
  - 72mph from the Southwest (winter)
  - 105mph from the Southwest (winter)
- Tornado
  - Category F2
  - Traveled from the Northwest to Southeast

Boundary Conditions for the problem consisted of:

- Winter
  - Ambient temperature of -13°F.
  - Temperature of the shield building remained at a constant 7°F.
- Summer
  - Ambient temperature of 104°F.
  - Temperature of the shield building remained at a constant 130°F.

Results extracted from the CFD:

- Pressure distributions on the surface.
- Heat transfer coefficients.
- Vorticity shedding calculated on the 72mph case.

Model Generation

The CFD mesh consisted of [redacted] to create the air volume. The total size of the air volume was a 2,500 ft. diameter with a height of 670 ft. Using a large air volume eliminates any wall effects that might be caused from flow interacting to close to a wall boundary (Figure 1). The element mesh size used for the model was [redacted]. Using a [redacted] mesh size allows the vorticity shedding to be captured more accurately.

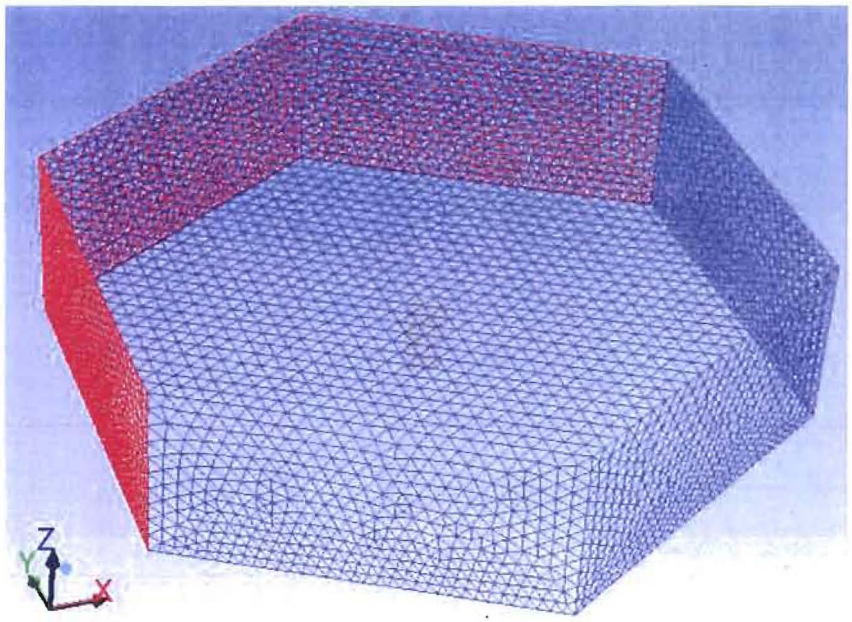

FIGURE 1: AIR VOLUME FOR CFD MODEL

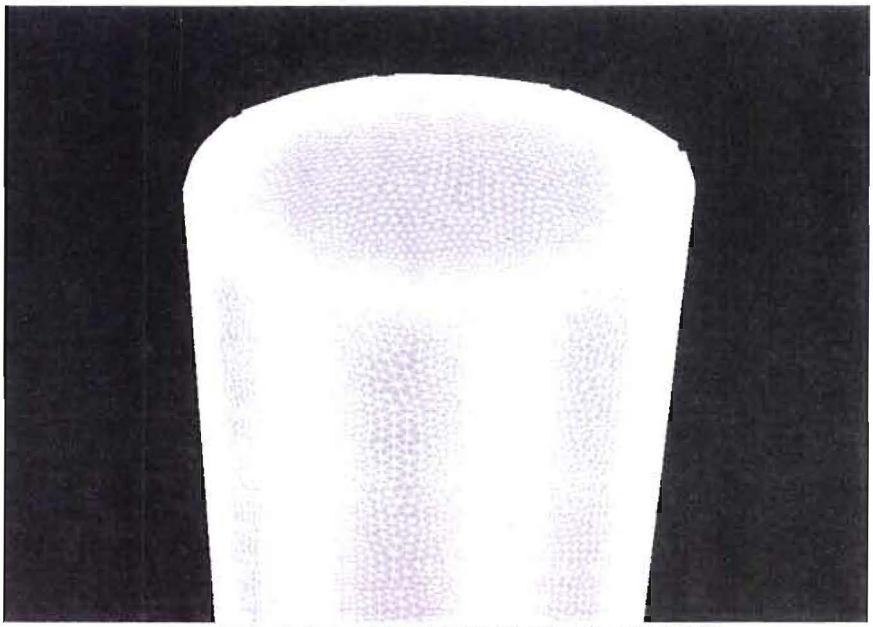

FIGURE 2: SHIELD BUILDING CFD SURFACE MESH

Solution Method

The CFD program used for this analysis was FLUENT version 13, an industry standard and proven analytical code. Some documentation from the website states "To address the stringent quality requirements of the nuclear industry, ANSYS has well-documented development processes and verified software releases. The comprehensive, best-in-class software solutions comply with NQA-1 standards for developing software for the nuclear industry, including ANSYS WORKBENCH, ANSYS FLUENT, ANSYS CFX and ANSYS MECHANICAL. The capability of FLUENT is used throughout the Aerospace and Defense, Nuclear, Automotive and Materials and Chemical processing. The code has been certified by numerous lab tests and code validations. [redacted] The energy and turbulence model was turned on for the solution. With the wind speed being below Mach 0.55 the incompressible ideal gas law was used. The shield building analysis without the buildings was done using a steady state solution. The reason for this method was there is not a lot of fluid interaction between structures. The shield building analysis with the building was done using a transient analysis solution.

Analysis

The first analysis performed was the 34mph case from the Northwest with summer conditions. Figure 3 below show the pressure loads on the windward side of the shield building.

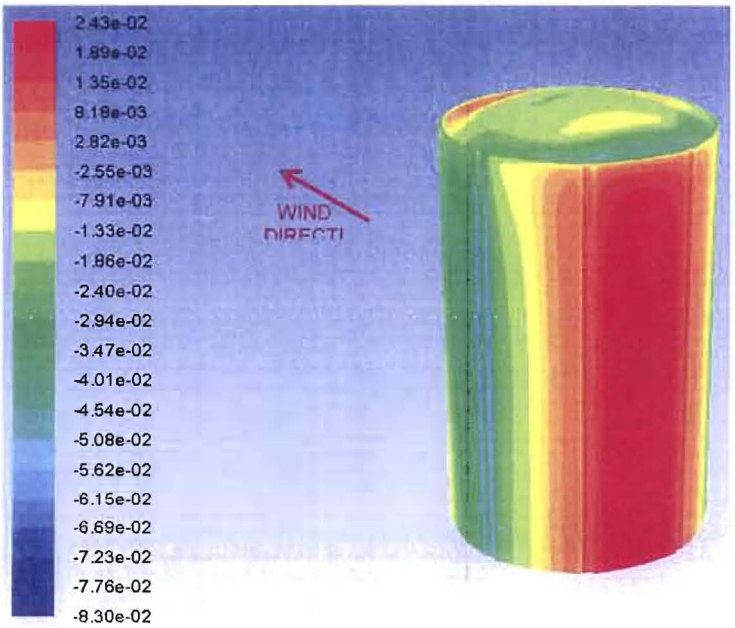

FIGURE 3: 34MPH NW SURFACE PRESSURES (Psi)

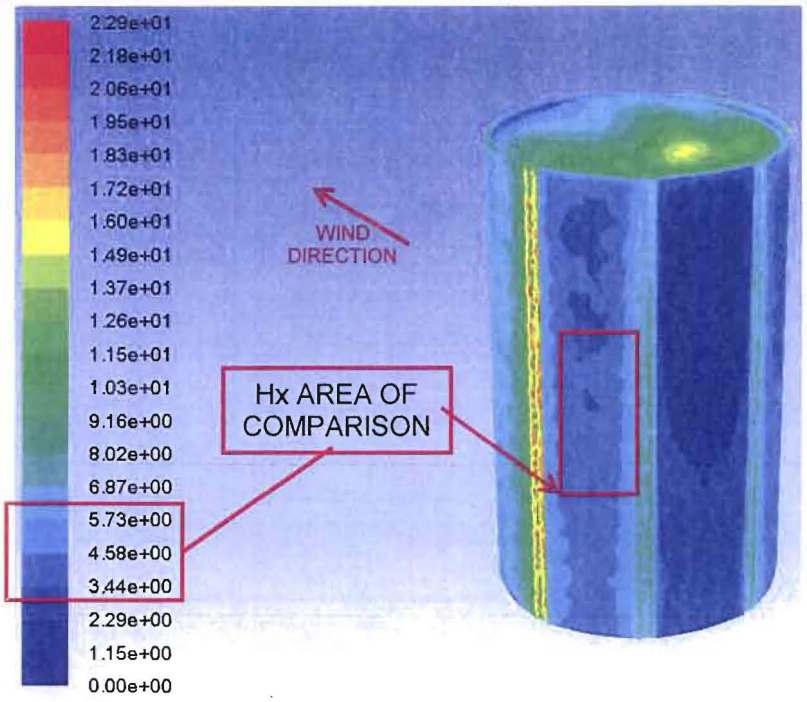

FIGURE 4: 34MPH SURFACE HEAT TRANSFER COEFFICIENT (Btu/Hr-Ft^2-°F)

Heat Transfer Coefficient Analytical Comparison

TOWER = 130°F (54.4°C)
AIR TEMP = 104°F (40°C)
TEMP AVERAGE = 117°F (42.22°C)
ν = 0.1693 cm^2/s
k = 0.027 w/m*k
Pr = 0.71
U = 15.20 m/s (34mph)
D = 44.73m
Re = U*D / ν
Re = 40,159,244
Nu = h*D/k
Nu = 0.3 + (0.62*Re^0.5*Pr^0.33)/([1+(0.4/Pr)^0.67]^0.25) *
[1+(Re/282,000)^0.625]^0.8
Nu = 38,092
h = (38,092*0.027 w/m*k) / 44.73m
h = 22.99 w/m^2*k * 0.1761 BTU / h*ft^2* °F
h = 4.05 BTU / h*ft^2* °F (This number compares to the front surface of the tower. Region of comparison is the light blue and cyan). This indicates the CFD model has predicted the correct surface heat transfer coefficients shown in Figure 4.
The cross section picture below (Figure 5) shows the velocity contours as the wind impacts the shield building. At slow wind speeds, the flow mainly stays attached except along the top front and aft edge. The flow tries to stay attached while passing by the

tower, but flow separation happens at the bottom half due to a lower pressure region. The top dome has a profound effect on the flow separation caused from the raised lip. Another contributor of flow separation is the architectural flute located on the side of the building.

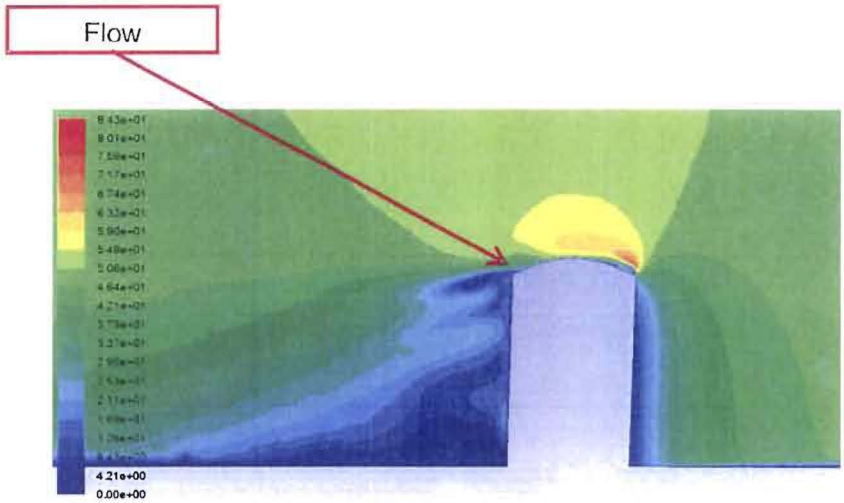

FIGURE 5: CROSS-SECTION OF 34MPH NW VELOCITY CONTOURS (Ft/Sec)

The second analysis performed was the 34mph case from the Southwest winter conditions. Figure 6 below shows the pressure loads on the shield building.

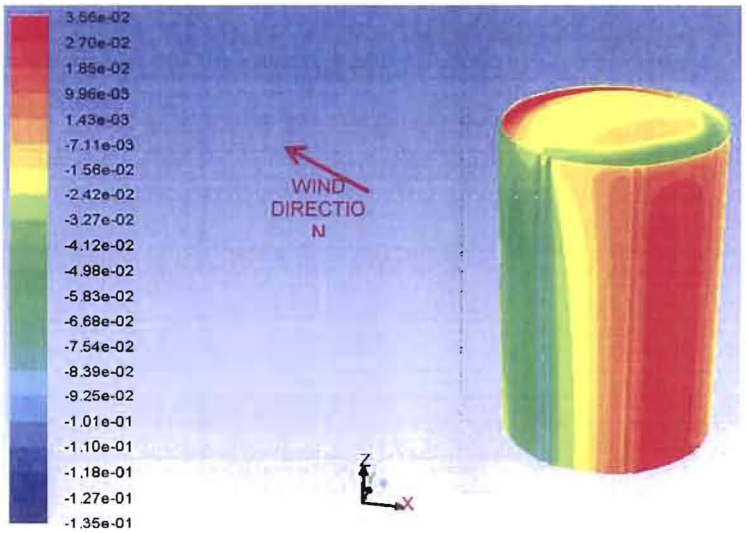

FIGURE 6: FRONT VIEW

FIGURE 6: 34MPH SW SURFACE PRESSURES (Psi)

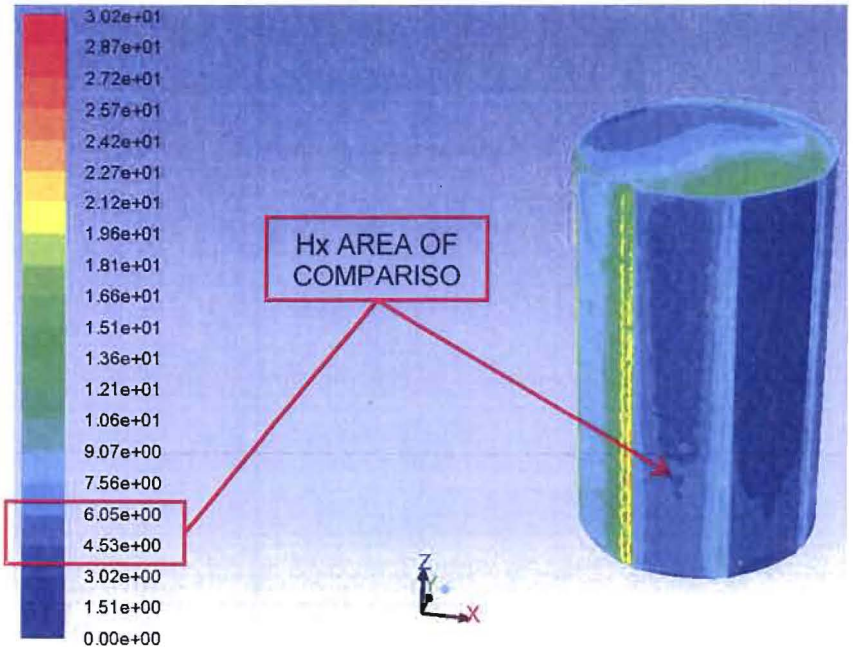

FIGURE 7: 34MPH SURFACE HEAT TRANSFER COEFFICIENT (Btu/Hr-Ft^2-°F)

Heat Transfer Coefficient Analytical Comparison

TOWER = -13°F (-25°C)
AIR TEMP = 7°F (-13.9°C)
TEMP AVERAGE = -3°F (-19.4°C)
ν = 0.1168 cm^2/s
k = 0.02248 w/m*k
Pr = 0.72
U = 15.20 m/s (34mph)
D = 44.73m
Re = U*D / ν
Re = 58,210,273
Nu = h*D/k
Nu = 0.3 + (0.62*Re^0.5*Pr^0.33)/([1+(0.4/Pr)^0.67]^0.25) *
[1+(Re/282,000)^0.625]^0.8
Nu = 55,111
h = (55,111 * 0.02248 w/m*k) / 44.73m
h = 27.7 w/m^2*k * 0.1761 BTU / h*ft^2* °F
h = 4.87 BTU / h*ft^2* °F (This number compares to the front surface of the tower. Region of comparison is the light blue and cyan). This indicates the CFD model has predicted the correct surface heat transfer coefficients shown in Figure 7.

The cross section picture below (Figure 8) shows the velocity contours as the wind

impacts the shield building. A cold dense air has a tendency to shed from structures more easily due to a higher Reynolds number. During winter conditions, the flow separates completely from the tower at 34mph. A result of this is sever vorticity shedding. An effect of flow separation at lower speeds will cause a cyclic pressure load on the containment tower. The top dome has increased the effect of flow separation. Another contributor of flow separation is the architectural flutes located on the side of the building.

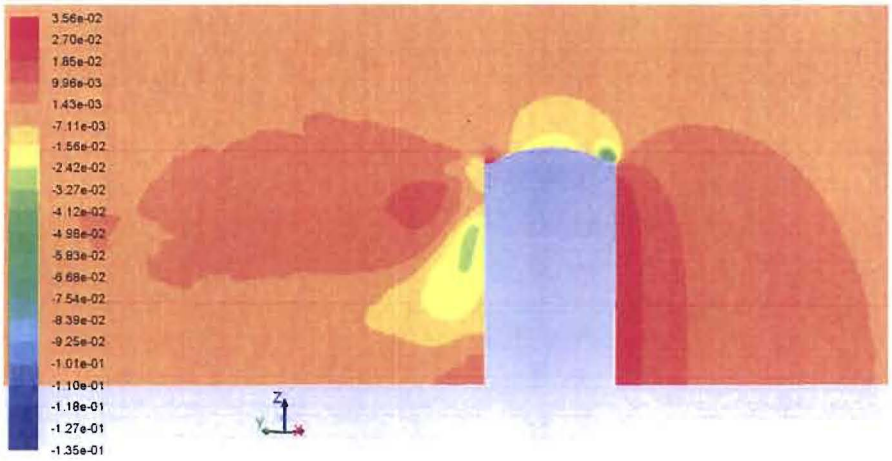

FIGURE 8: CROSS-SECTION OF 34MPH SW PRESSURE CONTOURS (Psi)

The third analysis performed was the 72mph case from the Southwest with winter conditions. Figure 9 below show the pressure loads on the windward side of the shield building.

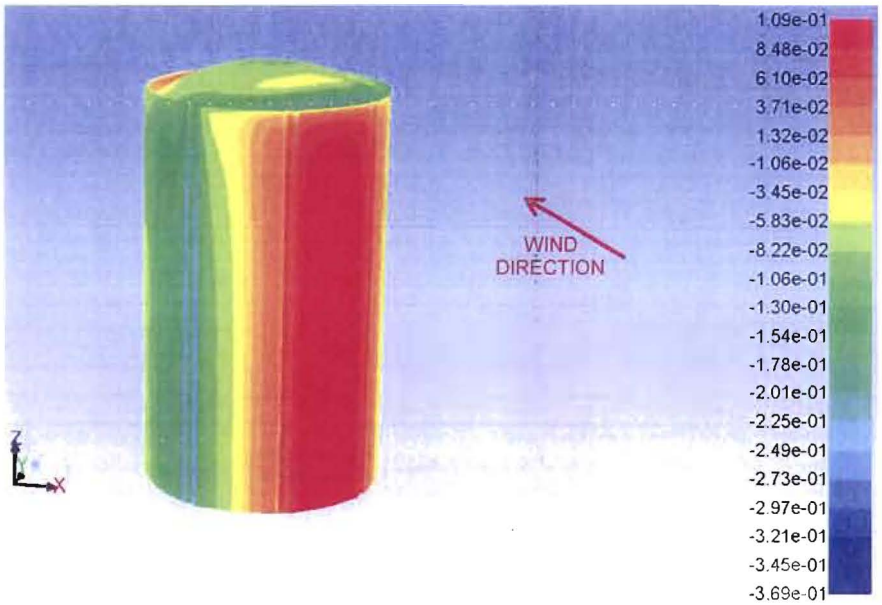

FIGURE 9: 72MPH SW SURFACE PRESSURES (Psi)

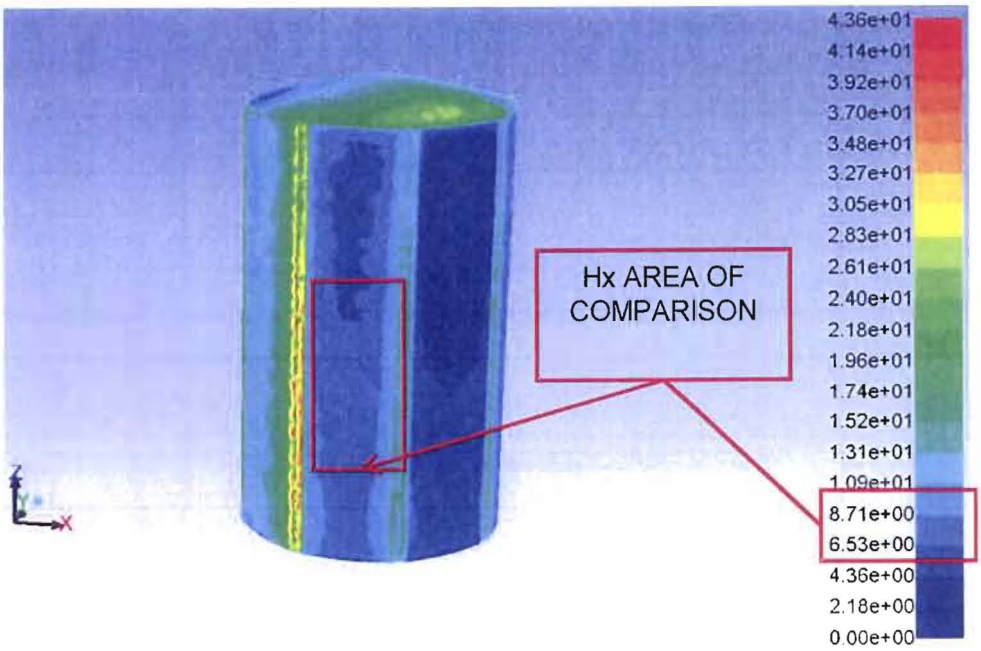

FIGURE 10: 72MPH SURFACE HEAT TRANSFER COEFFICIENT (Btu/Hr-Ft^2-°F)

Heat Transfer Coefficient Analytical Comparison

TOWER = -13°F (-25°C)
AIR TEMP = 7°F (-13.9°C)
TEMP AVERAGE = -3°F (-19.4°C)
ν = 0.1168 cm^2/s
k = 0.02248 w/m*k
Pr = 0.72
U = 32.63 m/s (72mph)
D = 44.73m
Re = U*D / ν
Re = 124,960,607
Nu = h*D/k
Nu = 0.3 + (0.62*Re^0.5*Pr^0.33)/([1+(0.4/Pr)^0.67]^0.25) *
[1+(Re/282,000)^0.625]^0.8
Nu = 97,032
h = (97,032 * 0.02248 w/m*k) / 44.73m
h = 48.76 w/m^2*k * 0.1761 BTU / h*ft^2* °F
h = 8.587 BTU / h*ft^2* °F (This number compares to the front surface of the tower. Region of comparison is the light blue and cyan). This indicates the CFD model has

predicted the correct surface heat transfer coefficients (Figure 10).

The pressure contours have not dramatically changed from the 34mph, but the pressure load and suction has increased (Figure 11). Cold dense air has a tendency to shed from structures more easily due to a higher Reynolds number. During winter conditions, the flow separates completely from the tower at 72mph (Figure 12). An effect of the flow separation at higher speeds will cause more cyclic pressure loads on the containment tower. The top dome has increased the effect of flow separation. Another contributor of flow separation is the architectural flutes located on the side of the building.

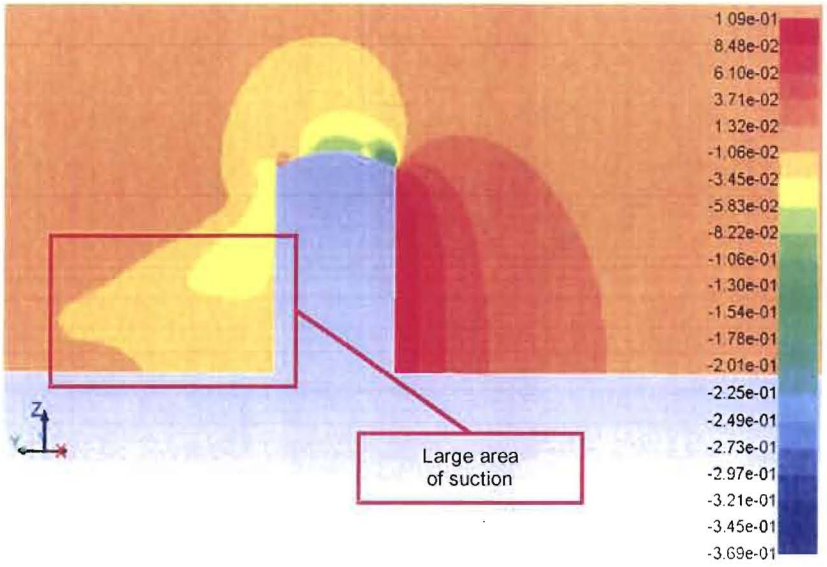

FIGURE 11: CROSS-SECTION OF 72MPH SW PRESSURE CONTOURS (Psi)

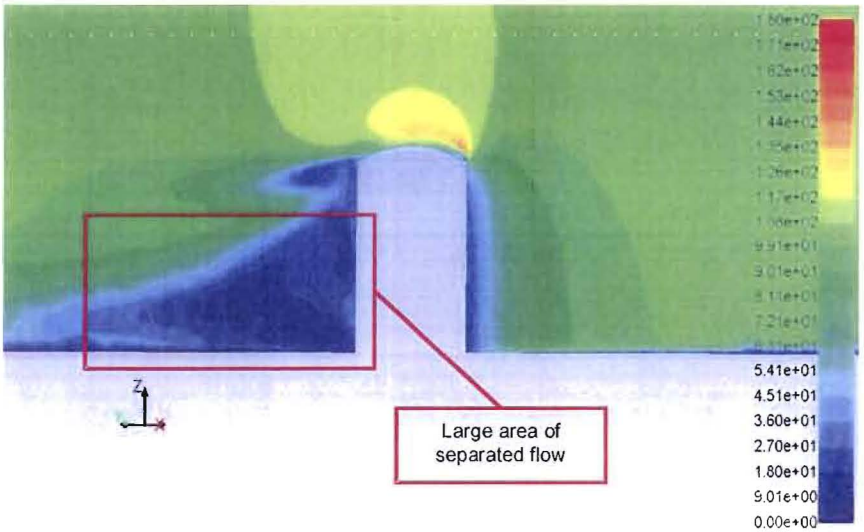

FIGURE 12:CROSS-SECTION OF 72MPH SW VELOCITY CONTOURS (Ft/Sec)

Creation of Combined Shield and Auxiliary Building CFD Model

The CFD mesh for the combined model consisted of 3.26 million cells to create the air volume. Total size of the air volume was a 2,500 ft. diameter and a height of 670 ft. Using a large air volume eliminates any wall effects (Figure 13). [redacted] Using a small mesh size will allow vorticity shedding to be captured more accurately.

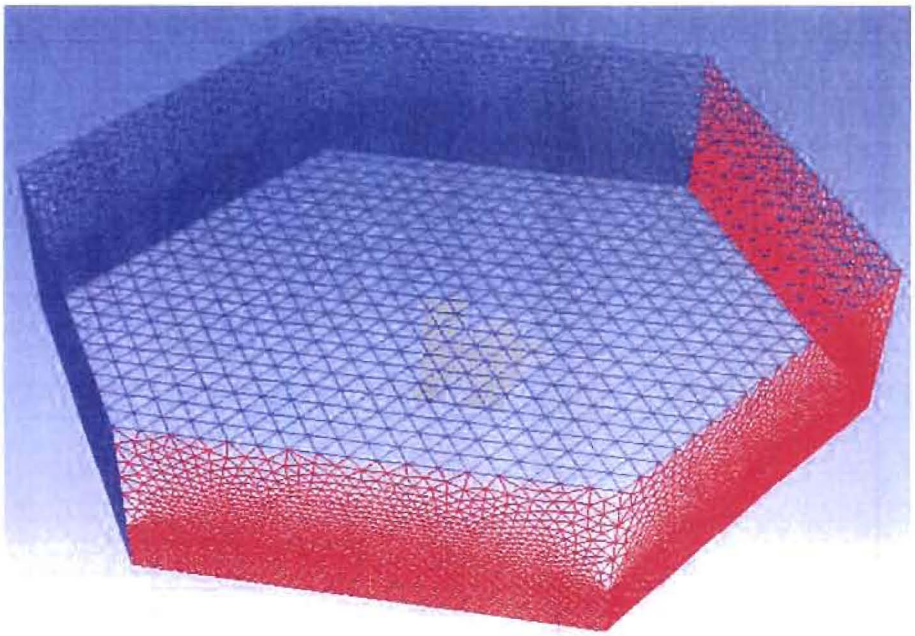

FIGURE 13: AIR VOLUME FOR COMBINED SHIELD AND AUXILIARY BUILDING CFD MODEL

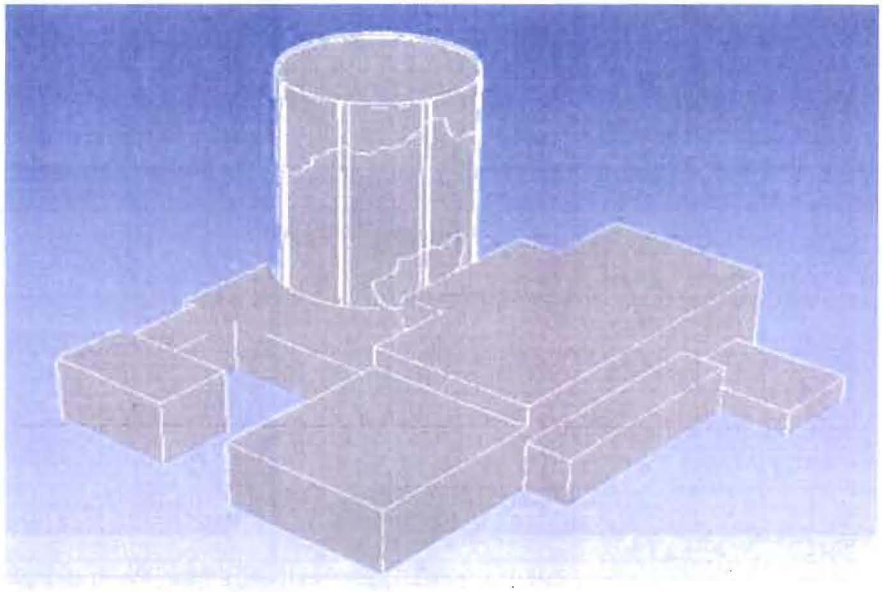

FIGURE 14: CONCRETE SHIELD BUILDING WITH ADJACENT AUXILIARY BUILDING

The fourth analysis consisted performing the same previous analysis with the auxiliary building present. This analysis was run at 34mph from the Northwest with summer conditions.

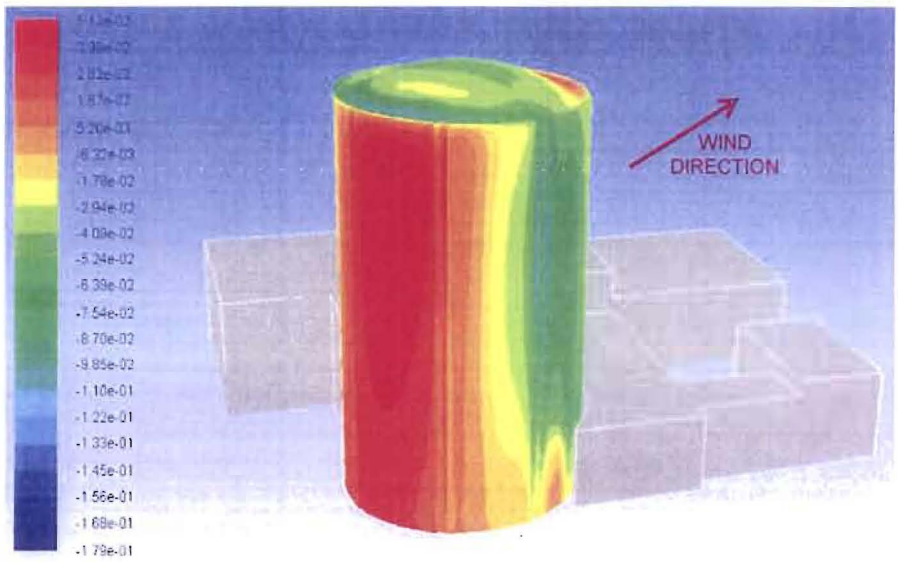

FIGURE 15: 34MPH NW SURFACE PRESSURES (Psi)

With the addition of the surrounding buildings, the pressure has increased by 0.027psi

from the previous analysis without the buildings (Figure 15). With the addition of the surrounding buildings, the heat transfer coefficients on the backside of the tower are not as uniform (Figure 16).

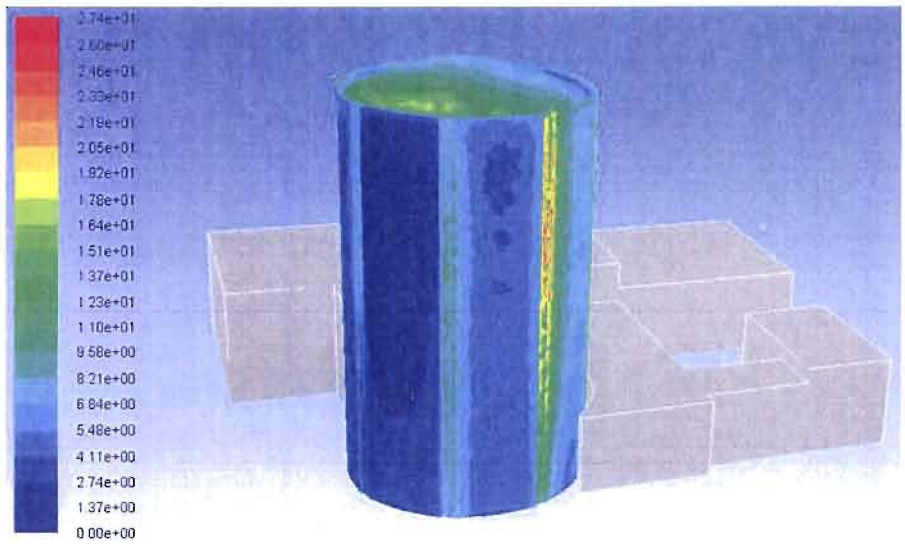

FIGURE 16: 34MPH SURFACE HEAT TRANSFER COEFFICIENT (Btu/Hr-Ft^2-°F)

Pressure contours have dramatically changed with the addition of surrounding buildings. There is a large low pressure region located above the buildings on the aft side of the containment tower (Figure 17). The velocity vectors are disrupted from the buildings causing the flow to separate at lower wind speeds (Figure 18).

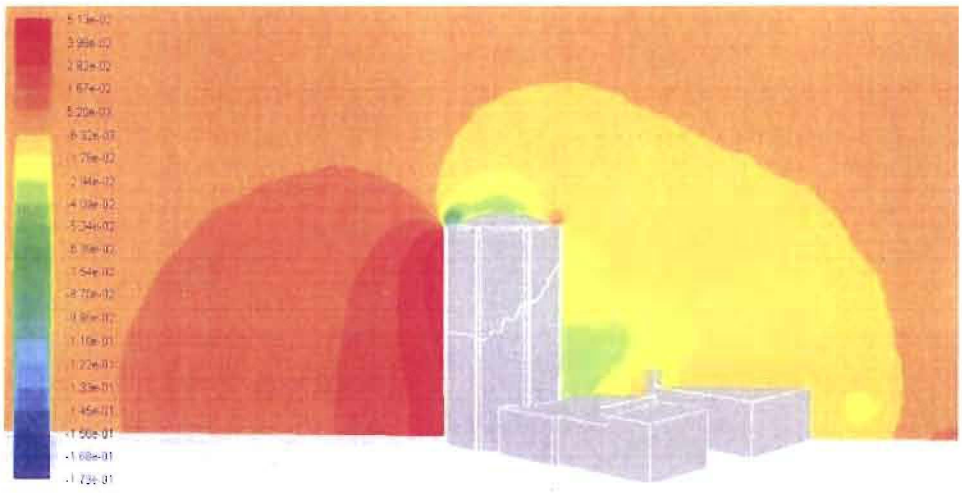

FIGURE 17: CROSS-SECTION OF 34MPH NW PRESSURE CONTOURS (Psi)

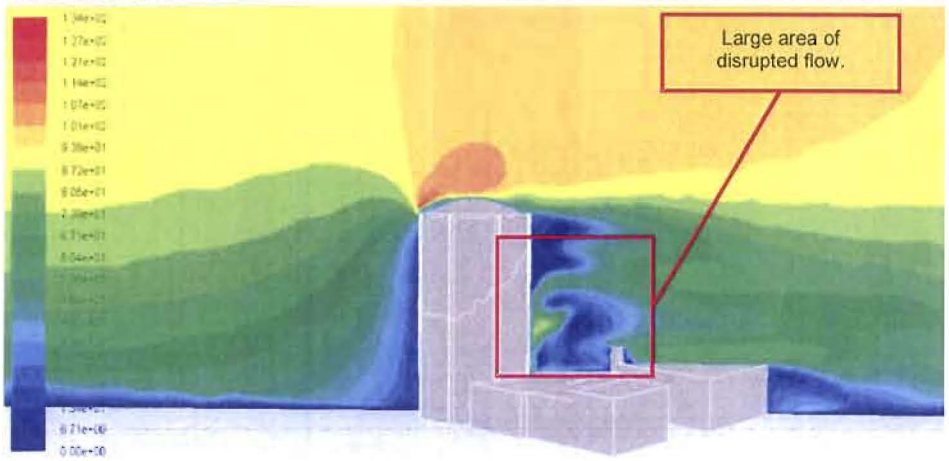

FIGURE 18: CROSS-SECTION OF 34MPH NW VELOCITY CONTOURS (Ft/Sec)

The fifth analysis consisted of setting the boundary conditions to 72mph from the Southwest with the buildings at winter conditions. With the addition of the surrounding Auxiliary building, the pressure has increased by 0.054psi (Figure 19). With the addition of the Auxiliary building and the resultant increased wind speed, the heat transfer coefficients are more disrupted (Figure 20).

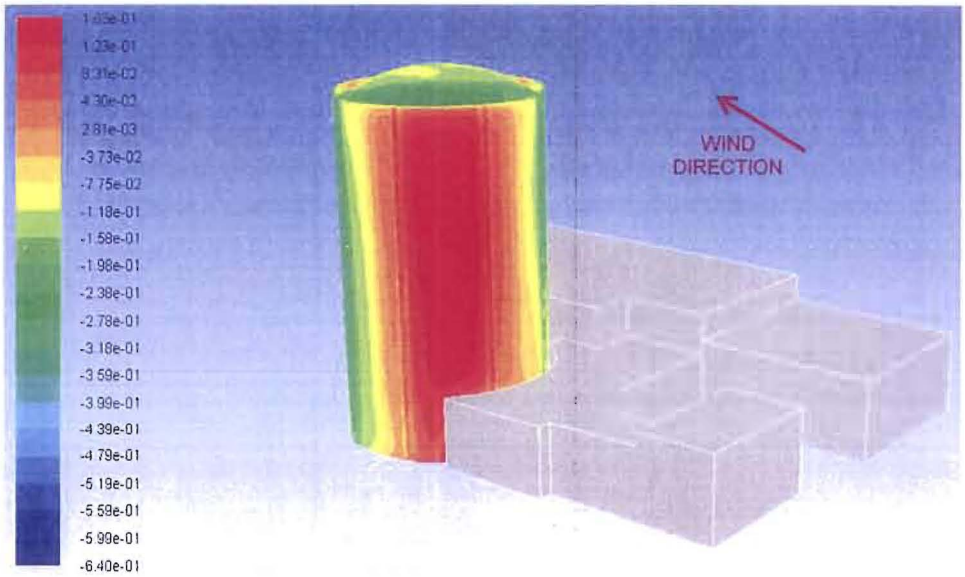

FIGURE 19: 72MPH SW SURFACE PRESSURE CONTOURS (Psi)

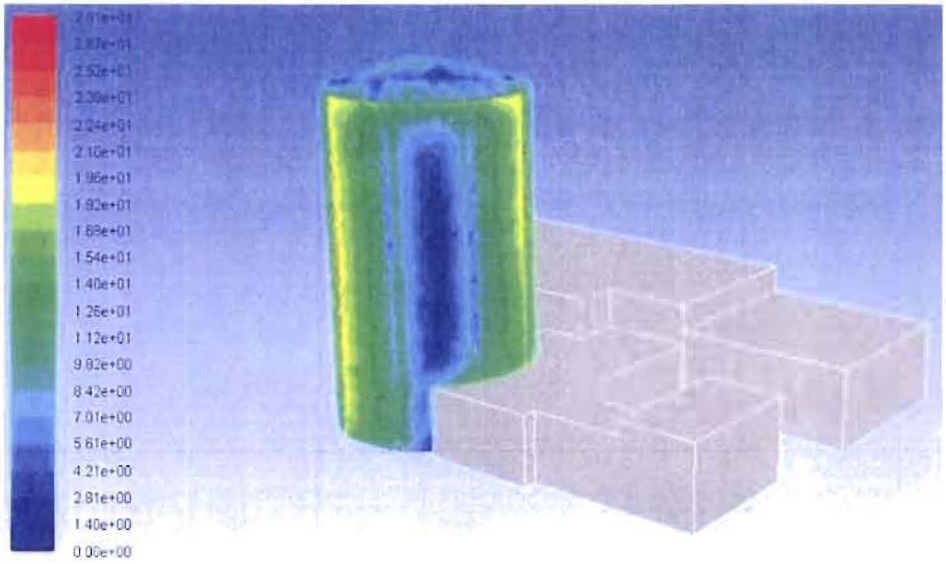

FIGURE 20: 72MPH SURFACE HEAT TRANSFER COEFFICIENT (Btu/Hr-Ft^2-°F)

The stagnation pressure region has shifted up towards the top of the containment tower (Figure 21). This is a result of the surrounding Auxiliary building being partially in front of containment tower. The flow on the aft side of the tower is turbulent compared to the case with no Auxiliary building (Figure 22).

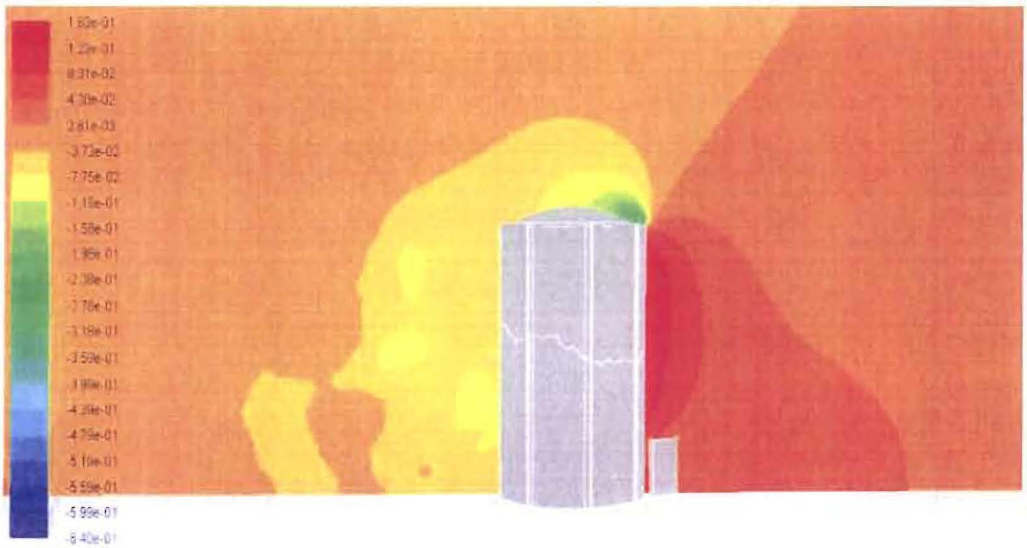

FIGURE 21: CROSS-SECTION OF 72MPH PRESSURE CONTOURS (Psi)

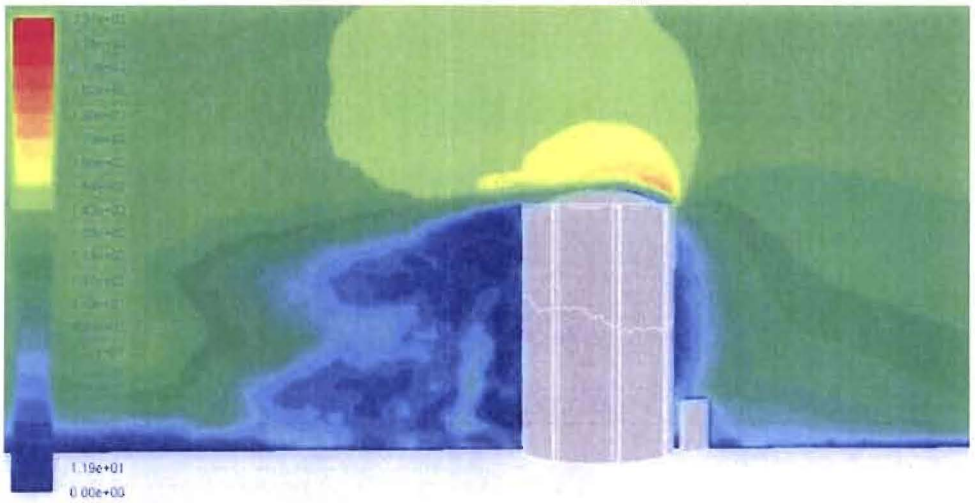

FIGURE 22:CROSS-SECTION OF 72MPH SW VELOCITY CONTOURS (Ft/Sec)

The sixth analysis consisted of setting the boundary conditions to 105mph from the Southwest with buildings at winter conditions. The pressure on the windward side of the containment tower has significantly increased (Figure 23). In addition, the heat transfer coefficient stagnation area for the 105mph case has dramatically decreased on the windward side (Figure 24).

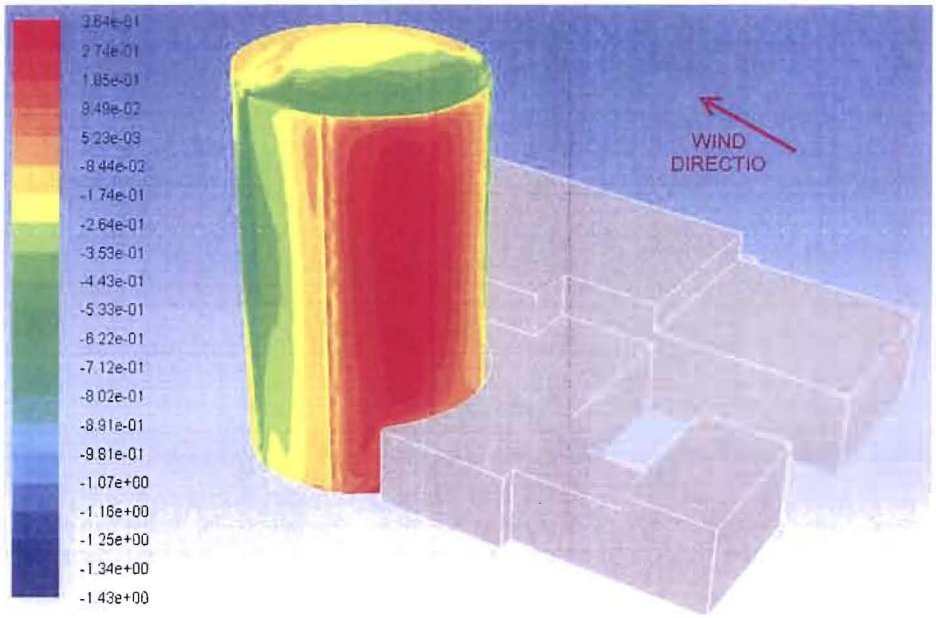

FIGURE 23: 105MPH SW SURFACE PRESSURE CONTOURS (Psi)

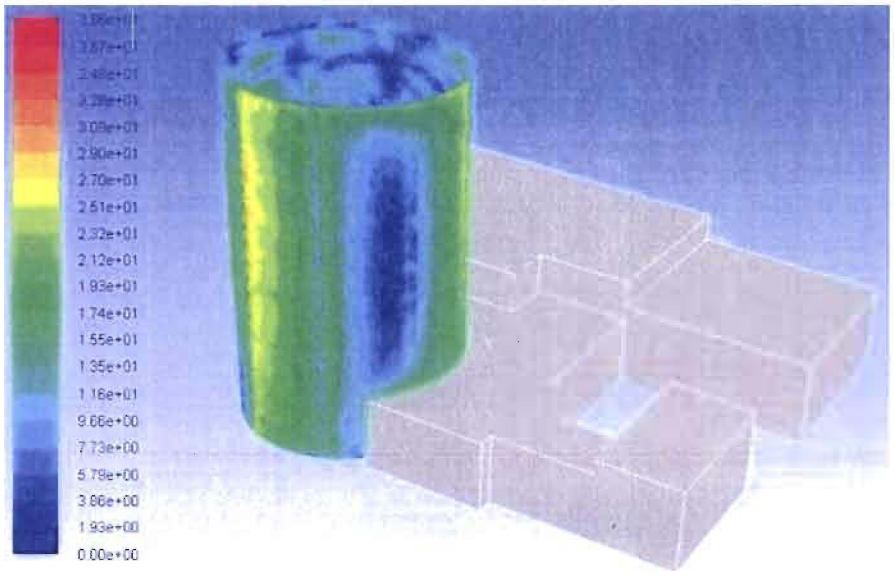

FIGURE 24: 105MPH SURFACE HEAT TRANSFER COEFFICIENT (Btu/Hr-Ft^2°F)

The stagnation pressure region has shifted up towards the top of the containment tower (Figure 25). This is a result of the Auxiliary building being partially in front of containment tower. The flow on the aft side of the tower is unsteady and turbulent (Figure 26). The addition of the Auxiliary building has caused the flow to rise due to the pressure increase just before the shield building. This results in a higher pressure region at the midpoint causing a larger overturning moment. The two figures below show pressure and velocity contours at 105mph during winter conditions.

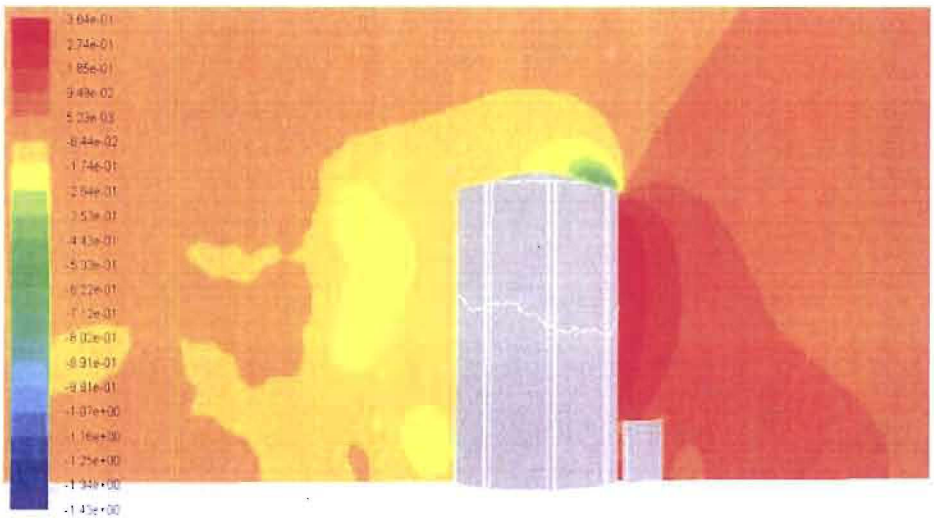

FIGURE 25: CROSS-SECTION OF 105MPH SW PRESSURE CONTOURS (Psi)

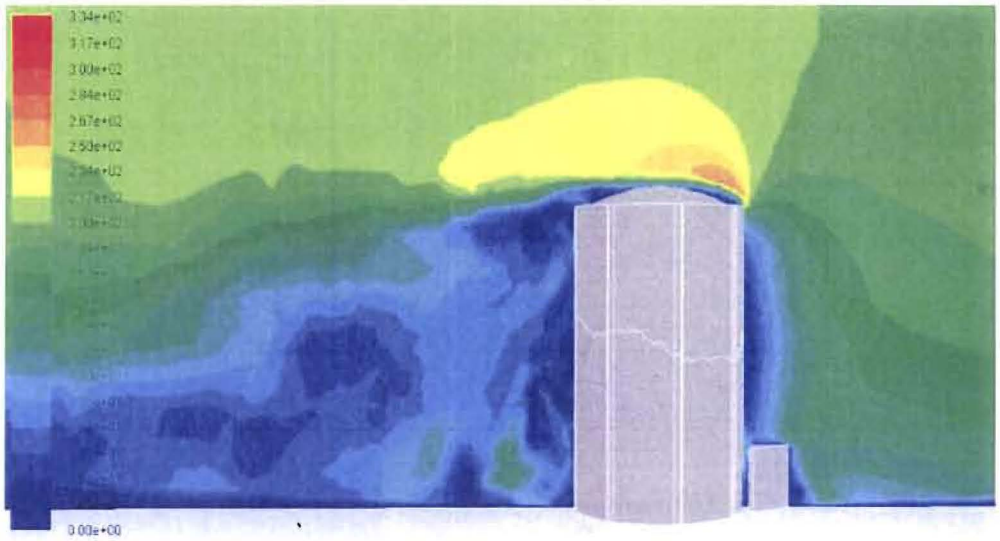

FIGURE 26: CROSS-SECTION OF 105MPH SW VELOCITY CONTOURS (Ft/Sec)

To show the flow disturbance created by the containment tower and Auxiliary building, two figures are shown below of the velocity streamlines (Figure 27). A large wake is created downstream and the flow does not reattach within the fluid boundary defined for the analysis model (Figure 28).

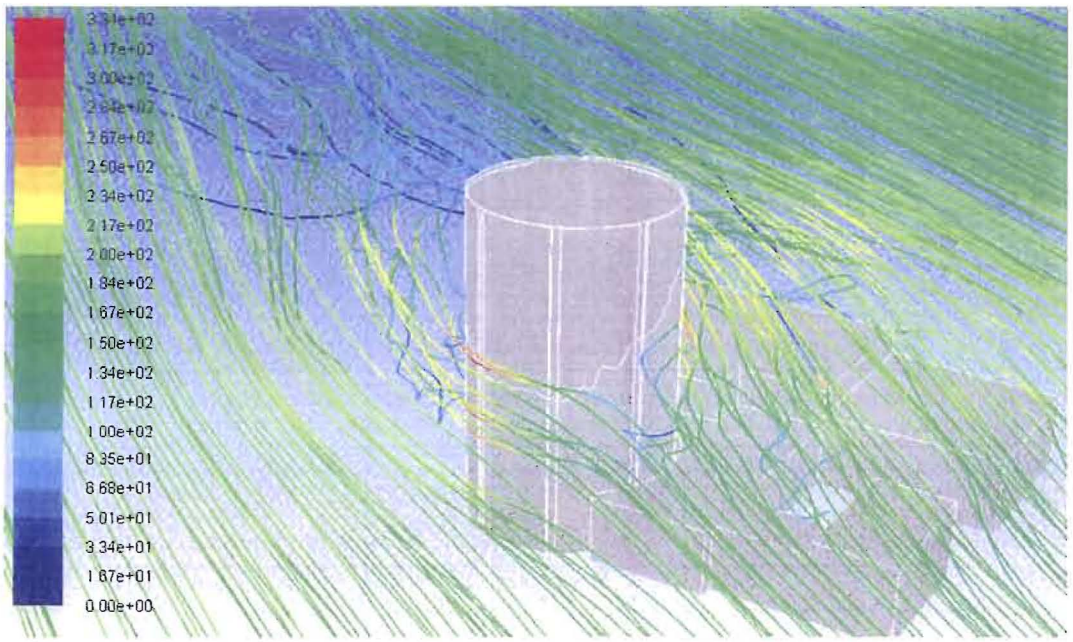

FIGURE 27: 105MPH SW VELOCITY STREAMLINES (Ft/Sec)

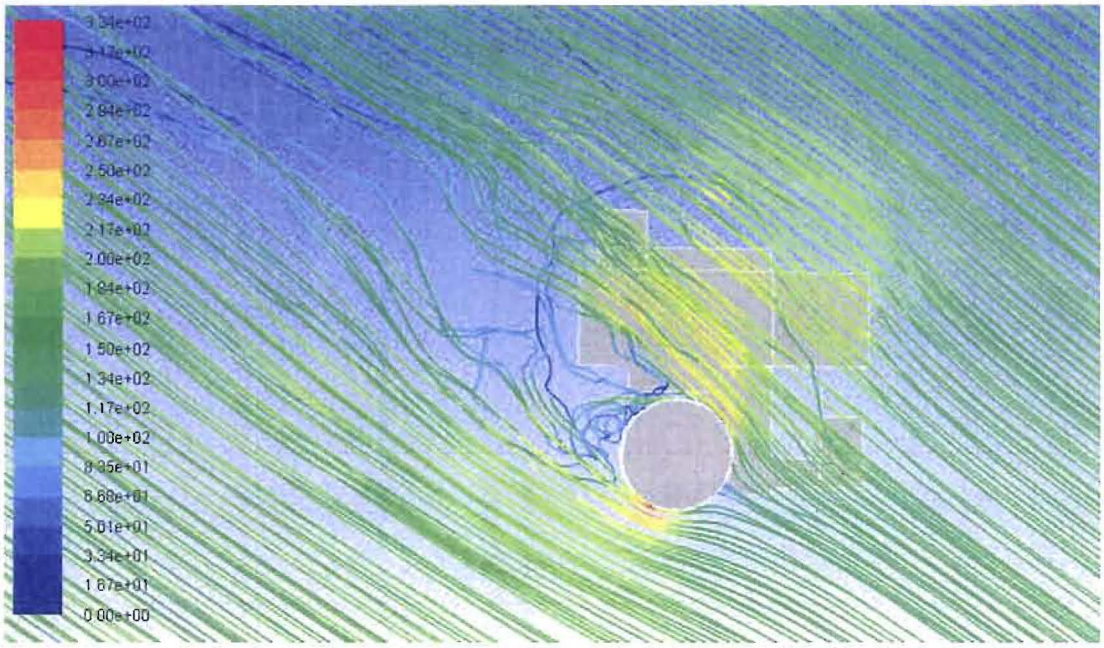

FIGURE 28: TOP VIEW OF 105MPH SW VELOCITY STREAMLINES (Ft/Sec)

The last analysis that was performed for the Davis-Besse shield building was of the 1998 tornado. This tornado was classified as F2 tornado with wind speeds between 113 and 157 mph. The base of the tornado was estimated at 100 yards wide and touched down just west of the Davis-Besse facility between 8:45 and 9:00pm on June 24, 1998. The tornado traveled just past the shield building in a southeasterly direction for a distance of 3.5 miles.

The tornado was a much more complicated analysis. To properly model the tornado, a transient analysis was performed using the FLUENT large eddy solver. This allows the user to capture data at selected time steps vs. a simple steady state solution. [redacted] The tornado was created using a 300 foot wide circular face on the ground and top boundary surfaces of the CFD model control volume. This allowed a rotational boundary condition to be used to start the spinning of the tornado. [redacted].

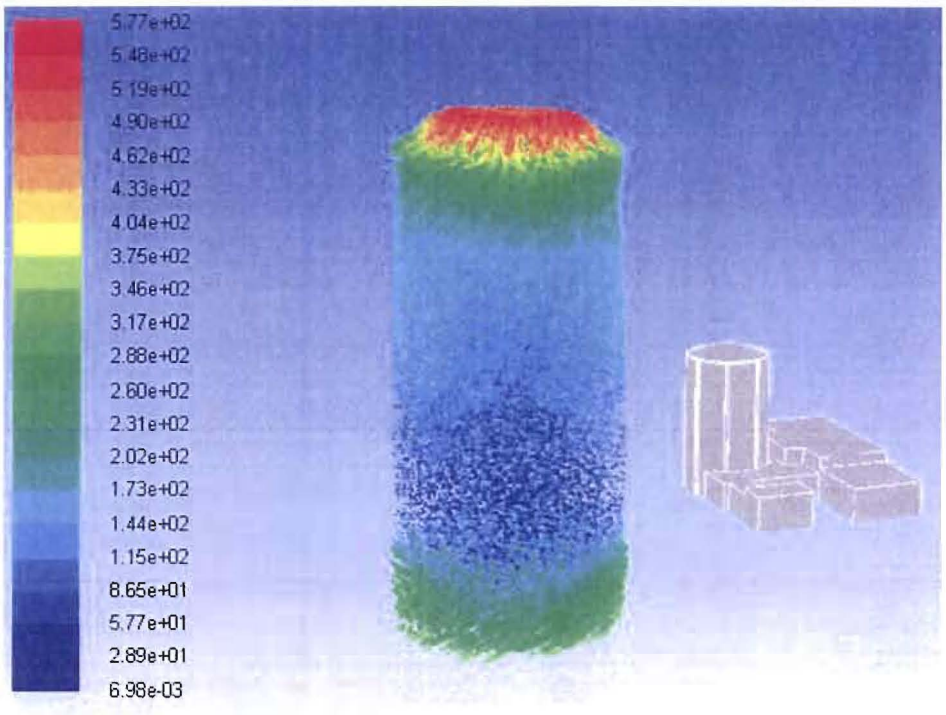

FIGURE 29: VELOCITY VECTORS SIMULATING A TORNADO (Ft/Sec)

Once the tornado was stable, the process began to move the domain with the tornado towards the buildings. The tornado characteristics were obtained from the NOAA website where the direction and forward velocity were listed. These boundary conditions were used to move the tornado pass the containment tower. To capture 9 seconds of data, the FLUENT CFD analysis ran for about 30 hours. During this time, FLUENT was programmed to capture pressure contours every second so a MPEG video could be created at the end of the analysis. Also during the analysis, data was exported to capture the pressure loads as well as the heat transfer coefficients.

During the analysis, one could observe when the tornado got closer to the buildings as the vortex structure of the tornado started to break down. This results when the vortex flow at the base of the tornado is disrupted by the presence of the buildings. Since the shield and auxiliary building are comparable to the width of the base of the tornado, they constituted a major impediment to the flow of the tornado. Consequently, at its closest approach, which was assumed to be 100 yards, the pressures induced by the tornado were attenuated. If there is enough energy, the tornado will reform once any obstruction is gone. This behavior is evident below in the images of the pressure contours as the tornado passed by the shield and auxiliary buildings (Figure 30 and 31)

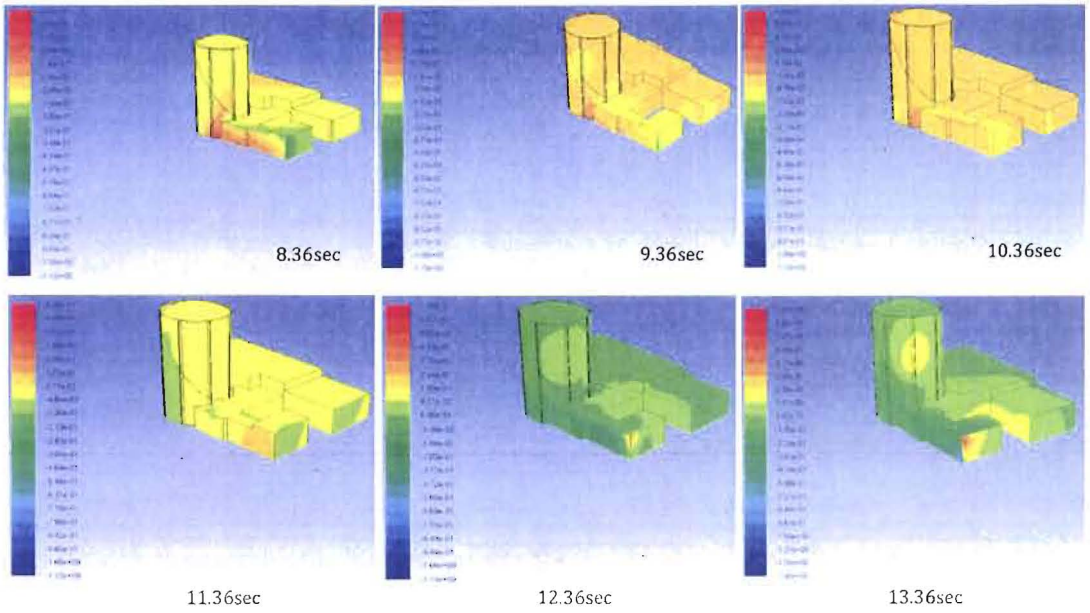

FIGURE 30: SURFACE PRESSURE CONTOURS DURING THE PASSAGE OF THE 1998 F2 TORNADO

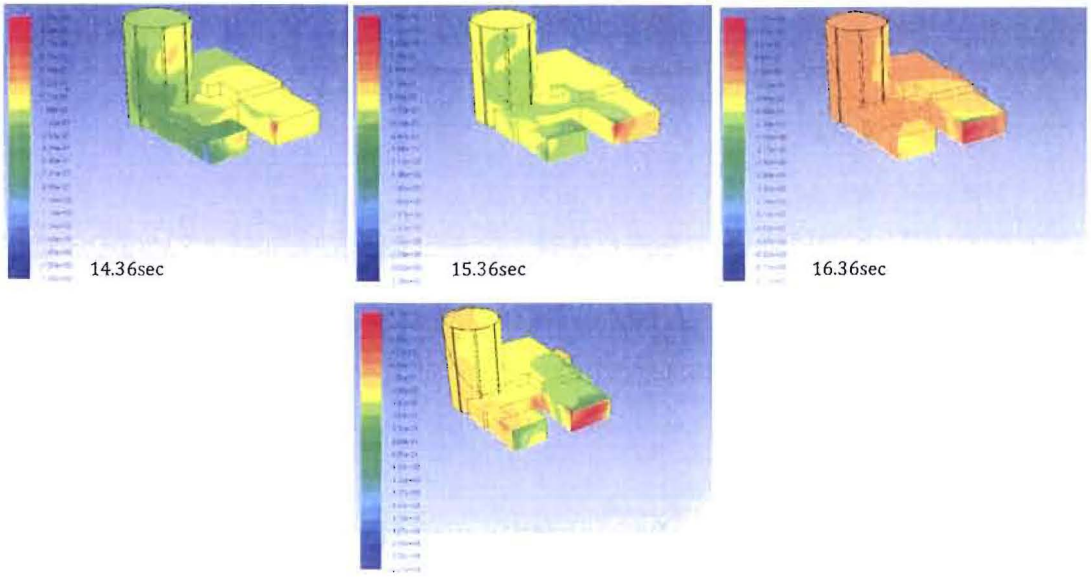

FIGURE 31: SURFACE PRESSURE CONTOURS DURING THE PASSAGE OF THE 1998 F2 TORNADO

Estimation of Surface Pressures and Convection Coefficients for Other Wind Speeds

CFD analyses were performed only for 34, 72 and 105 mph speeds. However, thermal stress analyses were also performed for 36 and 76 mph south and north westerly winds as well. If there is no change in the wind direction, then the surface heat transfer coefficients derived from the CFD analyses can be scaled to estimate the corresponding values for slightly higher or lower velocities.

For a free standing cylinder subjected to a cross flow, the convection coefficient is proportional to $Re^{.8}$ where Re denotes the Reynolds number and is given by the expression:

$$Re = \frac{\rho V D}{\mu}$$

where:

ρ = density
v= velocity
μ = viscosity

Since the Reynolds number is proportional to the velocity, the surface convection coefficient will scale as the ratio of the velocities to .8 power. In this way, the convection surface coefficients at other velocities could be derived from the CFD analyses for winds traveling in the same directions analyzed.

Similarly, the surface pressure on shield building will vary as the square of the velocity. Consequently, the surface pressure at slightly different wind speeds was derived by scaling the CFD derived pressures by the square of the velocity ratio. Once again, this methodology will only work if the direction of the wind remains unchanged and the change in wind speed is not appreciable.

Exhibit 68: Debonding of Rebar/Concrete Lab Testing

Performance Improvement International

Providing a competitive advantage through research and applications

To: [redacted]

From: [redacted]

Date: 02/27/2012

Subject: Laminar Cracking of the Davis-Besse Shield Building – Concrete Sample Testing for Debonding

[redacted]

Based on my observation and examination of concrete-core samples received from the Davis-Besse Shield Building, my findings for Debonding are detailed in what follows.

[redacted]

Concrete/Rebar Interaction

Concrete/Rebar Interaction

Laboratory testing and examination was conducted on the only two concrete/rebar-interaction samples received from Davis-Besse, F2-790.0-4.5 and S13-633.08. The evidence indicates that there is potentially a lack of bonding between the concrete and rebar on both samples.

Testing and examination of the concrete/rebar-interaction samples shows the imprint from the rebar onto the concrete as well as iron oxide transfer.

Concrete/Rebar Interaction: Lack of Adhesion

The following plant photo shows the imprint of rebar onto concrete. The photo documents the measured distance between the crests as 1.0 inches. In addition, it also points out possible rust transfer. To confirm that the imprint originated from concrete/rebar interaction, Figure A2 is a confirmatory photo of a 1.25 inch diameter rebar that shows the same pattern as the imprint. The figure also illustrates the 1.0 inch crest to crest measurement.

Figure A 1: Shield Building Concrete Sample Illustrating Rebar Imprint

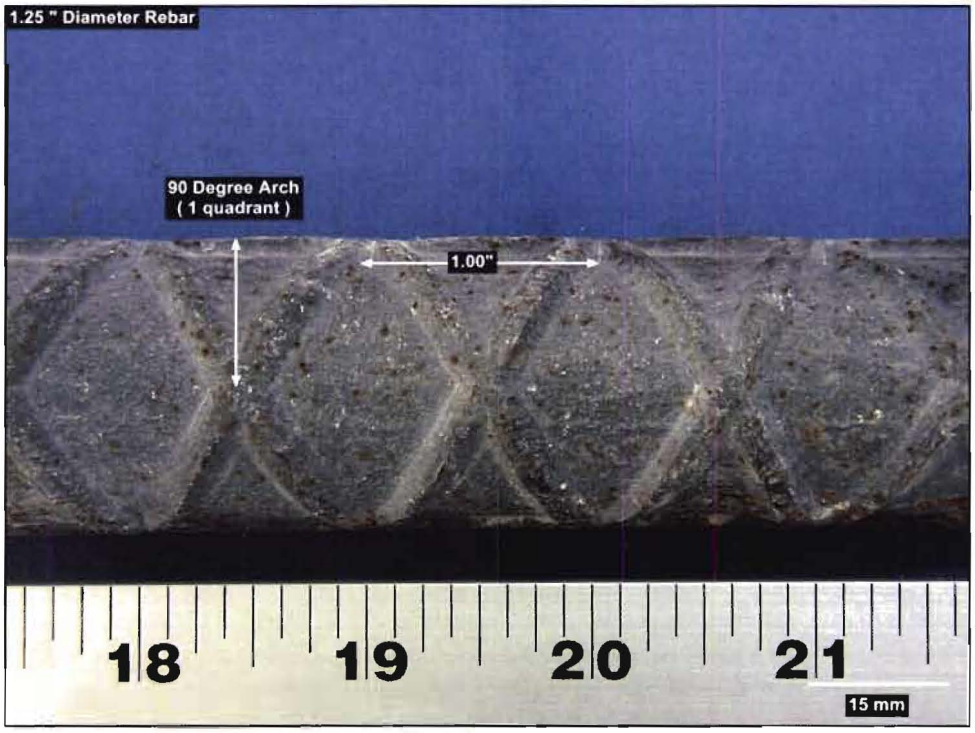

Figure A 2: 1.25" Diameter Rebar with 1.0" Crest-to-Crest Measurement

Figures A3 – A5, which show different views of Core F2-790.0-4.5, illustrate the lack of adhesion between the concrete and rebar, as rebar rib groove imprints are found on the sample.

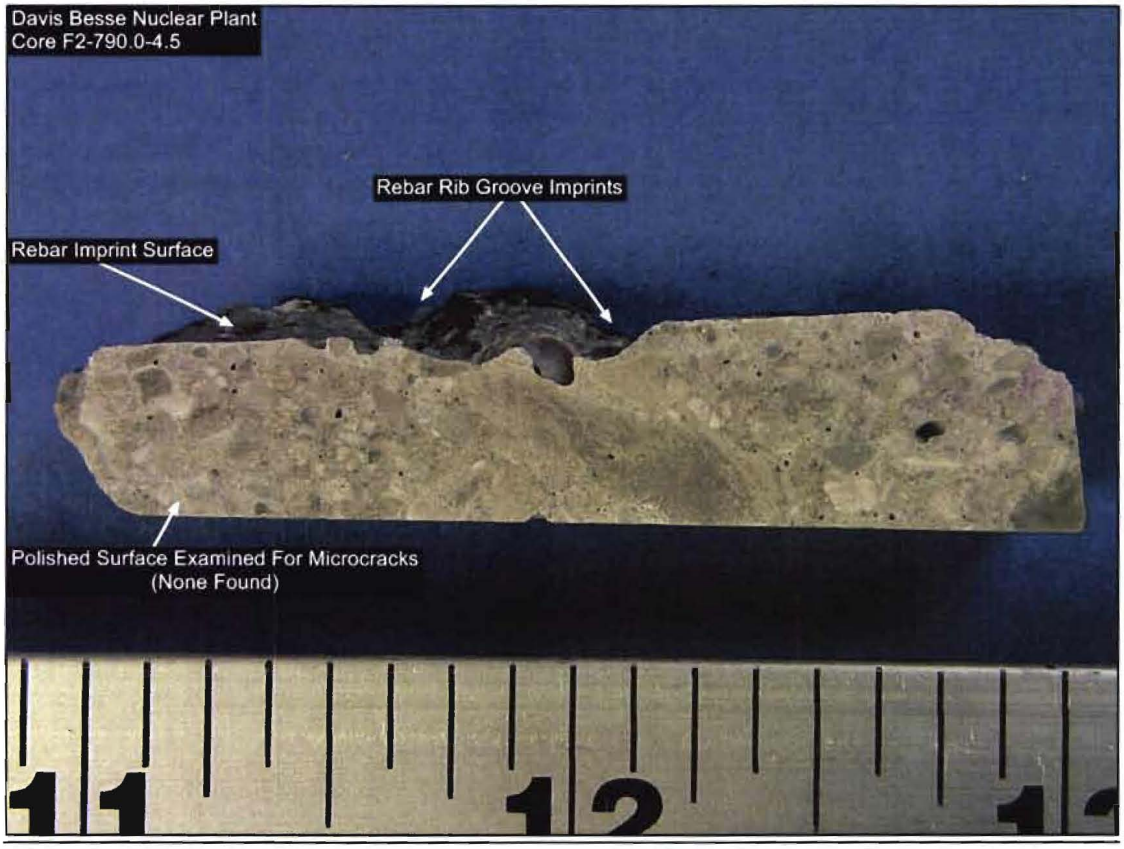

Figure A 3: Rebar Rib Groove Imprints (Core F2-790.0-4.5)

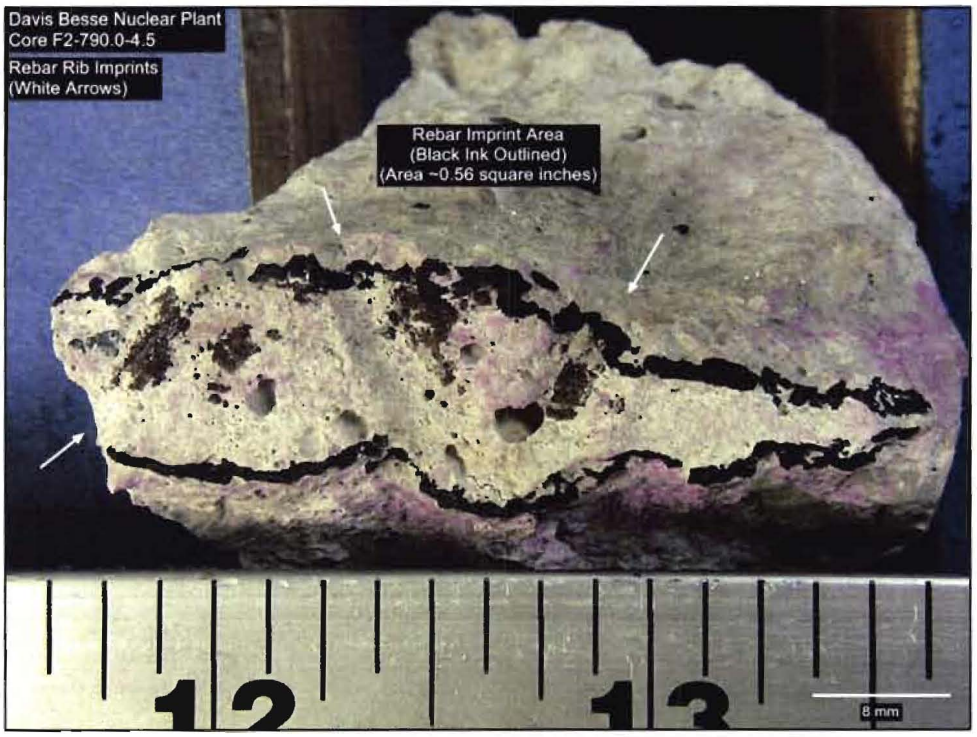

Figure A 4: Rebar Rib Groove Imprints (Core F2-790.0-4.5)

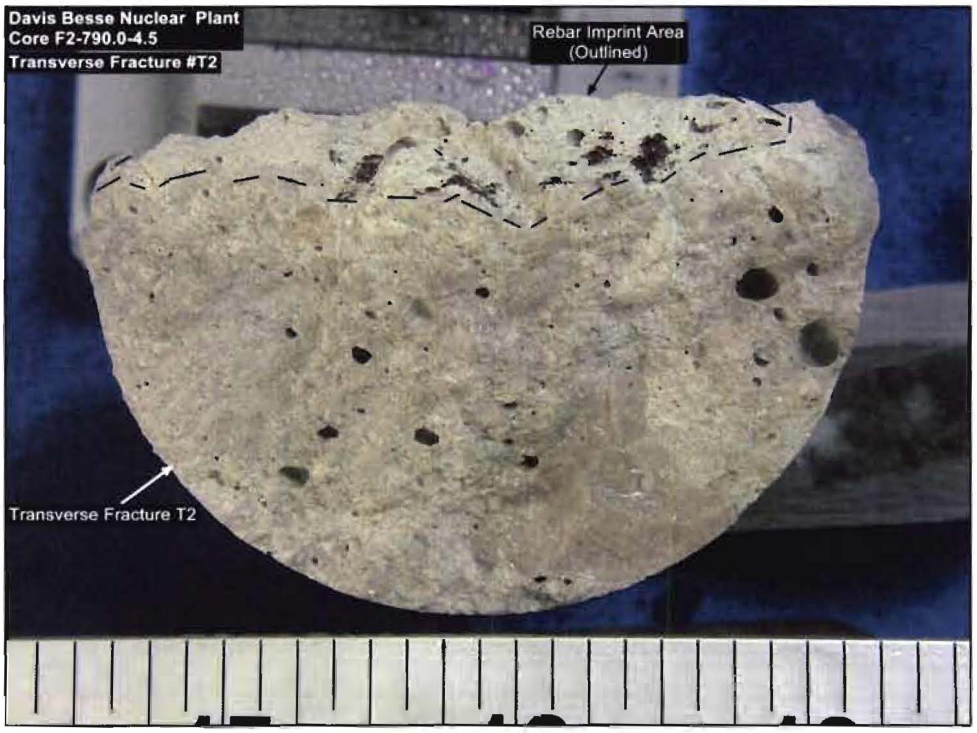

Figure A 5: Rebar Rib Groove Imprints (Core F2-790.0-4.5)

Concrete/Rebar Interaction: Iron Oxide Transfer

. Figures A6 – A8 and Figures A9 – A13, respectively show in sequential order

1. Possible iron oxide on the fracture surface,
2. A potential iron oxide deposit removed and measured for thickness
3. Energy-dispersive X-Ray Spectroscopy (EDS) performed on the prospective iron oxide deposit to confirm iron oxide.

Energy-dispersive X-Ray Spectroscopy is an investigative technique that involves X-ray excitation of a sample. The identification of the samples chemical characterization stems from the interaction between the X-ray and the element's atomic structure. According to the EDS tests performed, iron oxide was determined to exist on the concrete surfaces under examination.

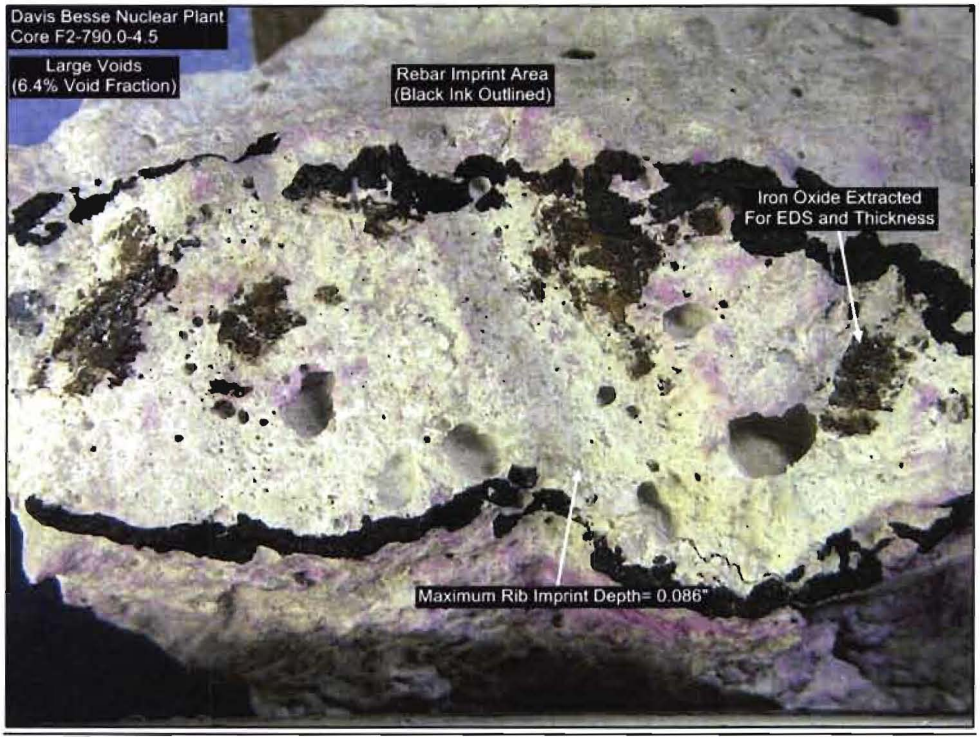

Figure A 6: Iron Oxide Transfer onto Concrete (Core F2-790.0-4.5)

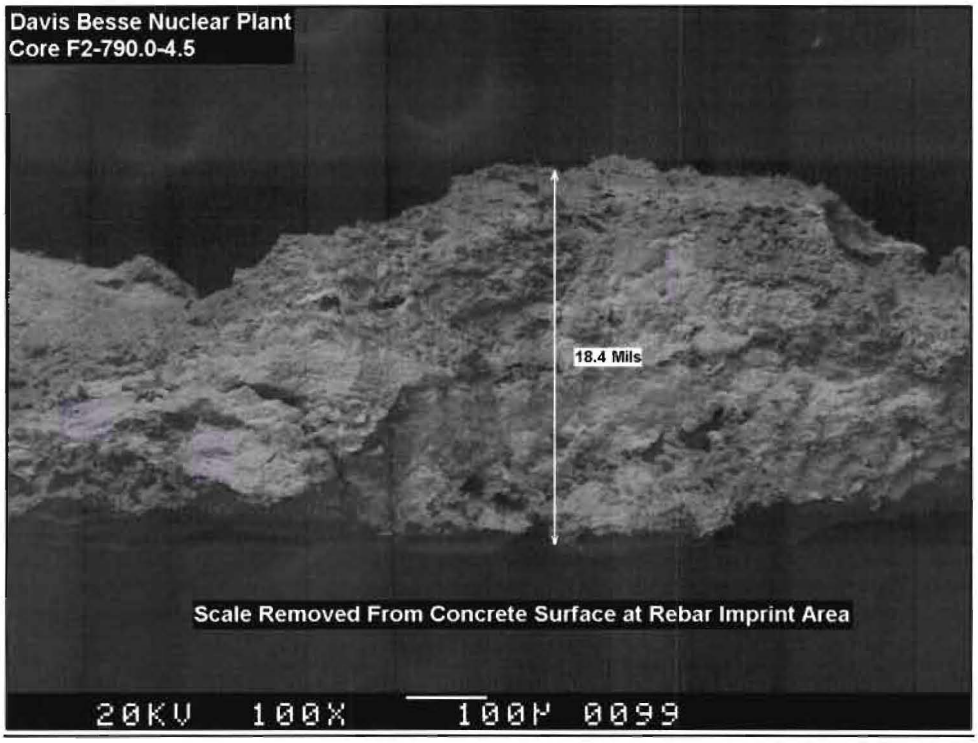

Figure A 7: Iron Oxide Deposit taken from Sample (Core F2-790.0-4.5)

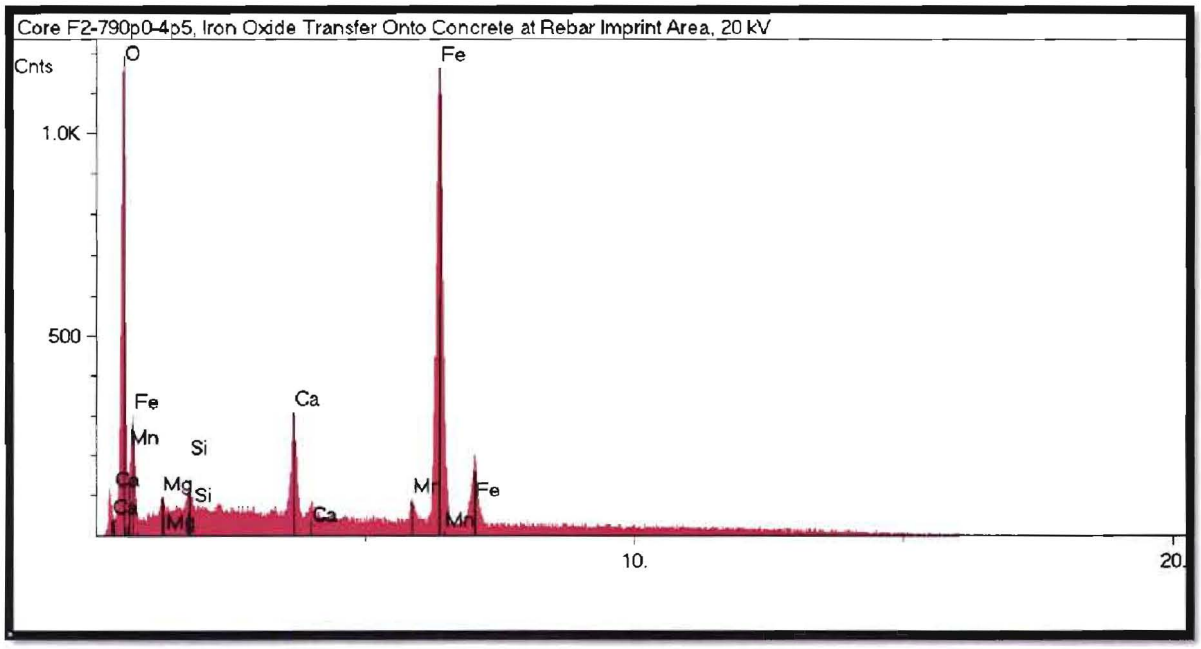

Figure A 8: Energy-dispersive X-Ray Spectroscopy Results from Iron Oxide Deposit (Core F2-790.0-4.5)

Figure A 9: Iron Oxide Transfer to Concrete (Core S13-633.08)

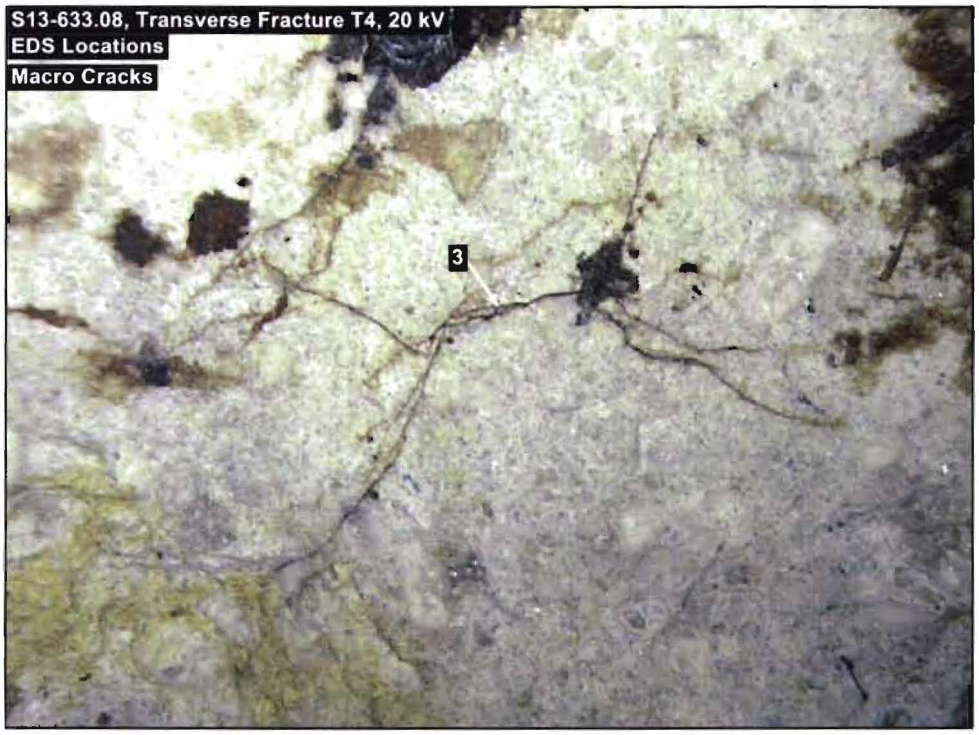

Figure A 10: Iron Oxide Transfer into Macro Cracks of Concrete (Core S13-633.08)

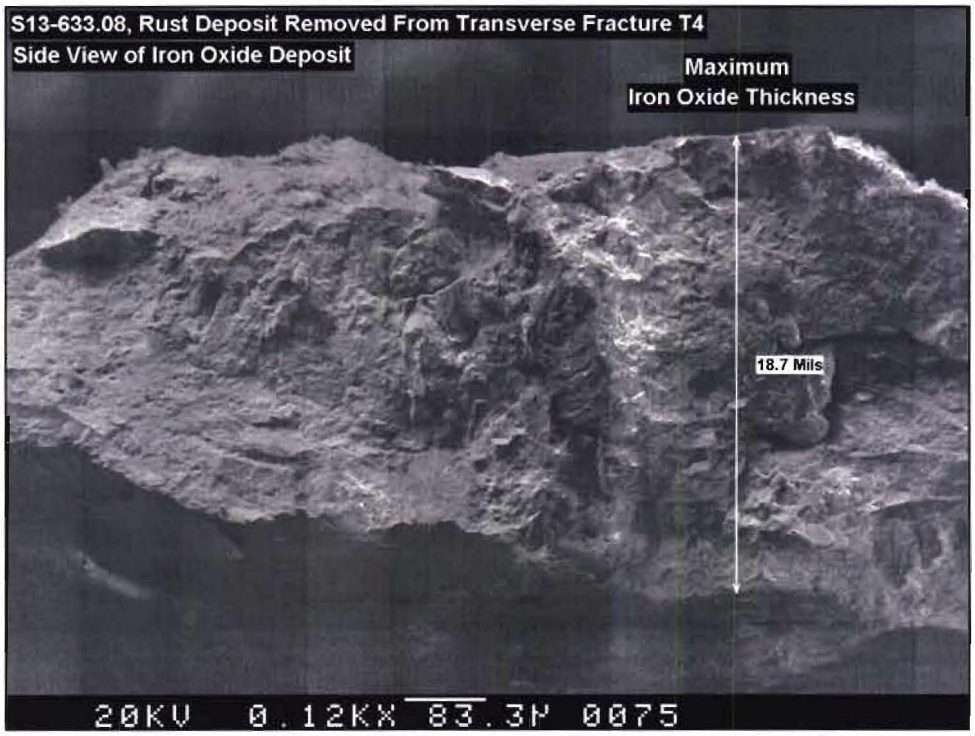

Figure A 11: Iron Oxide Deposit taken from Sample (Core S13-633.08)

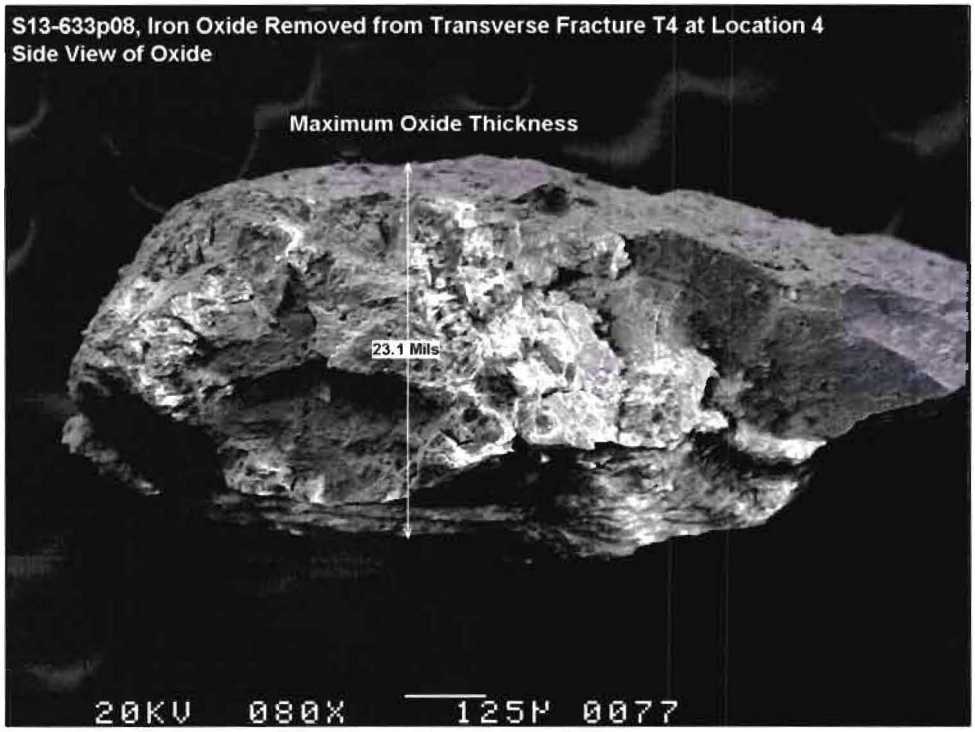

Figure A 12: Iron Oxide Deposit taken from Sample (Core S13-633.08)

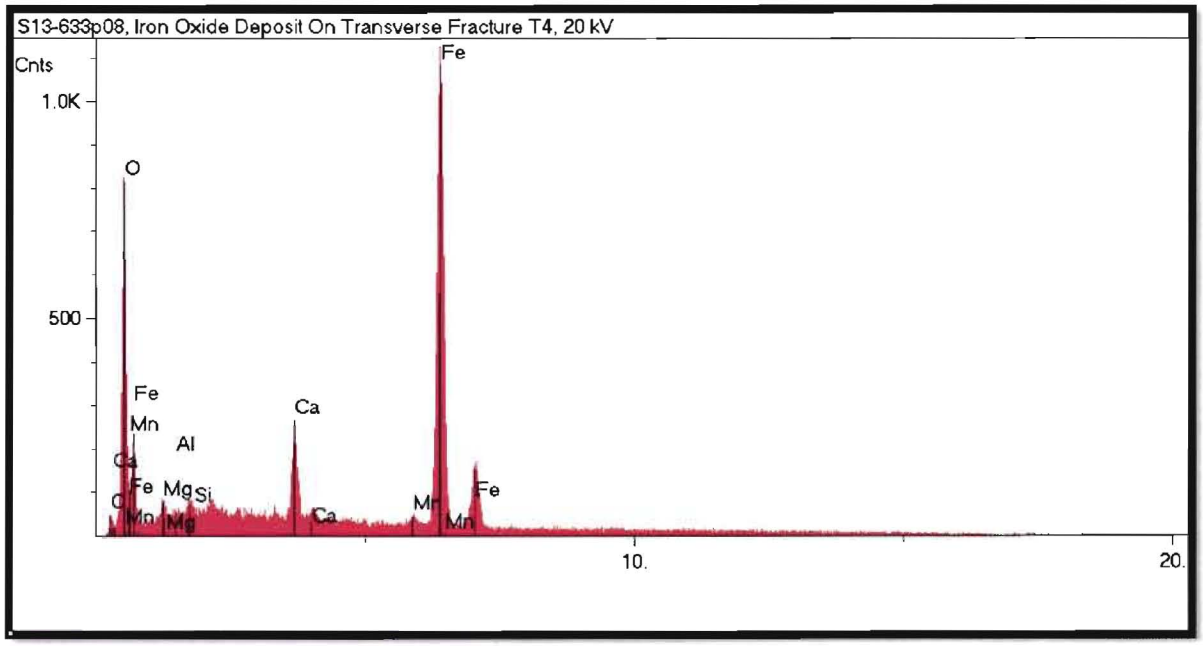

Figure A 13: Energy-dispersive X-Ray Spectroscopy Results from Iron Oxide Deposit (Core S13-633.08)

Exhibit 69: M-284a

Exhibit 69

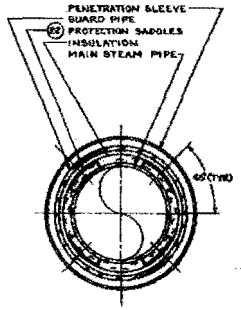

SECTION A-A
SCALE: 3/4"=1'-0"

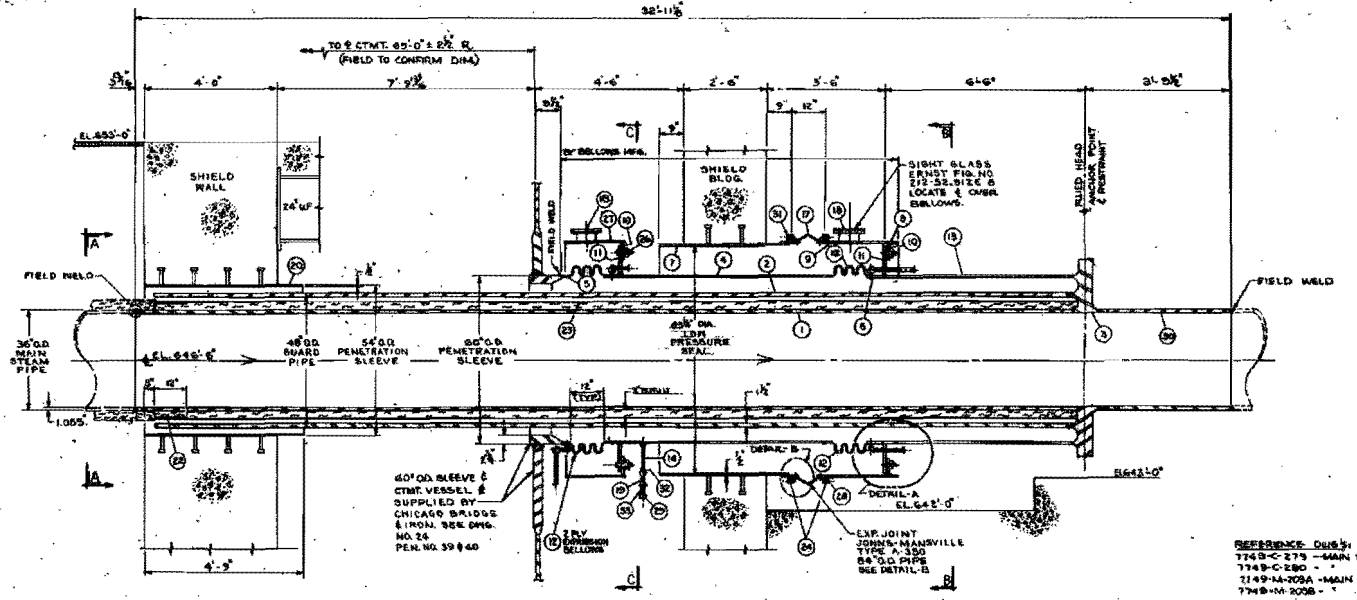

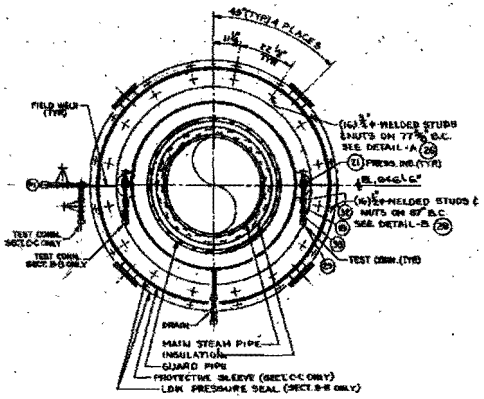

SECTION C-C
SECTION B-B
SCALE: 3/4"=1'-0"

MAIN STEAM FROM STM. GEN. PER [illegible]
SCALE: 3/4"=1'-0"

MAIN STEAM PENETRATION — BILL OF MATERIAL

ITEM	NO. REQ'D	DESCRIPTION	MATERIAL SPECIFICATION	CLASS	[illegible]	CODE	[illegible]	WEIGHT LBS	REMARKS
1	1	PIPE - 36 O.D. X 1.055" WALL	STL.	M-201 (M48.6-60)	A53 B	115.5	ASME SEC. III NC	YES	
2	1	PIPE - 48 O.D. X 1.50" WALL	STL.	M-201 (M48.6-60)	A53 B	115.5	ASME SEC. III NC	YES	
3	1	PILED HEAD	PWPL WT.	M-231		115.5	ASME SEC. III NC	YES	
4	1	60" O.D. PIPE - ¾" WALL	STL.	M-202		65	ASME SEC. III NC	YES	
5	1	60" O.D. PIPE - ¾" WALL	STL.	M-202	A53B	65	ASME SEC. III NC	YES	
6	1	60" O.D. PIPE - ¾" WALL	STL.	M-203	A53B	65	ASME SEC. III NC	YES	
7	1	54" WALL PIPE - ¾" WALL	STL.	CC-8		3	-	NO	
8	1	54" O.D. PIPE - ¾" WALL	STL.	M-206		3	-	NO	SPLIT FOR FIELD INST.
9	1	63 ¾" I.D. RING - 6 ½" X ¾"	STL.	M-206, M-220		3	-	NO	" " " "
10	2	50" O.D. X 36" I.D. X ¾" FLANGE	STL.	M-203		3	-	NO	" " " "
11	2	65" O.D. X 60" I.D. X 1 ¼" FLANGE	STL.	M-206		3	-	NO	" " " "
12	2	60" O.D. - 2 PLY BELLOWS	S.S.	M-238	1	90	ASME SEC. III NB	YES	
13	1	60" O.D. PIPE - ¾" WALL	STL.	M-202 (M48.6-60)	A53B	65	ASME SEC. III NC	YES	
14	1	8" SCH. 80 SMLS. PIPE	S.S.	M-253	1	90	ASME SEC. III NG	YES	
15	1	8" SCH. 80 SMLS. PIPE	S.S.	M-253	1	90	ASME SEC. III NG	YES	
16	4	8" 3000# FSE	S.S.	M-256	1	65	ASME SEC. III NG	YES	
17	1	54" I.D. CAP, WELD-IN TYPE A-350		CC-8		3	-	NO	
18	6	[illegible]		M-253		3	-	NO	
19	9	8" GATE VALVE, 900# BTG.	STL.	M-253, D-70		90	ASME SEC. III NG	YES	FURNISHED BY CLIENT
20	1	54" O.D. PIPE - ¾" WALL X 4'-9" LG.	STL.	CC-8		-	-	NO	
21	4	PRESSURE GAUGES	S.S.	M-253		46	-	NO	
22	4	8" S.S. SCH. 80 WELDING NIPPLE	S.S.	M-253		-	ASME SEC. III NC	YES	
23	1	¾" THICK INSUL. ON 54" PIPE	THERMOMASTER	M-[illegible]		-	[illegible]	NO	SEE NOTE 6
24	2	50" I.D. X 52" O.D. X ¼" GASKET	ASBESTOS	M-260		3	-	NO	-
25	1	62" O.D. X 56" I.D. X ¼" GASKET	ASBESTOS	M-260		45	-	NO	-
26	32	¾"ø WELDED STUDS (UNITS)	STL.	M-238		-	-	NO	SEE NOTE 5
27	1	54" O.D. PIPE - ¾" WALL	STL.	M-202		-	-	NO	SPLIT FOR FIELD INST.
28	32	¾"ø WELDED STUDS, NUTS & WASHERS	STL.	M-260		-	-	NO	
29	9	54" 3000 LB. SCRD. CAP	STL.			46	-	NO	PURCHASED BY CLIENT
30	1	54" O.D. - LOSS WALL PIPE	STL.	M-202 (M48.6-60)	A53B	115.5	ASME SEC. III NB	YES	
31	1	64 ¼" I.D. RING - 1 ½" X ¾"	STL.	CC-8		3	-	NO	
32	9	2½" NPT 3000# SW PEN. INSERT	STL.			46	-	YES	FURNISHED BY CLIENT
33		2½" SCH. 80 SMLS. PIPE	STL.			46	-	NO	" " "
34	4	2½" NPT 3000# SCRD. TEE	STL.			46	-	NO	" " "
34A		¾" THICK GASKET	GRAPHITE			45	-	NO	SEE NOTE 5

NOTES:

1. LOCATION OF ℄ OF PENETRATION NOZZLE HAS ½" TOLERANCE AROUND TRUE ℄ AND RADIAL TOLERANCE OF CONTAINMENT VESSEL IS ± 2½".
2. SLEEVES, ITEM 39 & 40 SHALL BE GROUTED BY CONTRACTOR 7749-B AFTER ALIGNMENT & WELDING OF ASSEMBLY.
3. BILL OF MATERIAL IS FOR ONE ASSEMBLY. 2 ASSEMBLIES REQUIRED.
4. FOR DETAILS OF THE BELLOWS ASSEMBLY SEE DWGS. 7749-M-238-1 & 2.
5. THE WELD ONLY AND WELD NUT CONFIGURATION SHOWN IN DETAIL "C" IS ACCEPTABLE INSTEAD OF A WELDED STUD AND NUT CONFIGURATION.
6. REPLACEMENT INSULATION SHALL BE PER SPECIFICATION [illegible]

REFERENCE DWGS:
7749-C-279 - MAIN STEAM LINE RESTRAINTS.
7749-C-280 - " " "
7749-M-209A - MAIN STEAM SYS. ISOMETRIC.
7749-M-209B - " " "

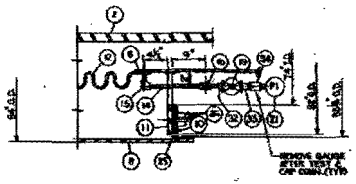

DETAIL-A
SCALE: ½"=1'-0"
FOR TRUE ORIENTATION OF BELLOWS TEST CONNECTIONS SEE SECTION B-B & C-C

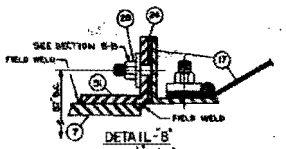

DETAIL-B
SCALE: ½"=1'-0"

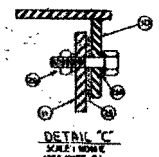

DETAIL "C"
SCALE: NONE
(SEE NOTE 5)

BECHTEL COMPANY
SAN FRANCISCO, CALIFORNIA

DAVIS-BESSE NUCLEAR POWER STATION
THE TOLEDO EDISON COMPANY
THE CLEVELAND ELECTRIC ILLUMINATING COMPANY

MAIN STEAM PENETRATION DETAILS

JOB NO.	DRAWING NO.	REV.
7749	M-284A	5

Exhibit 70: M-284b

Exhibit 70

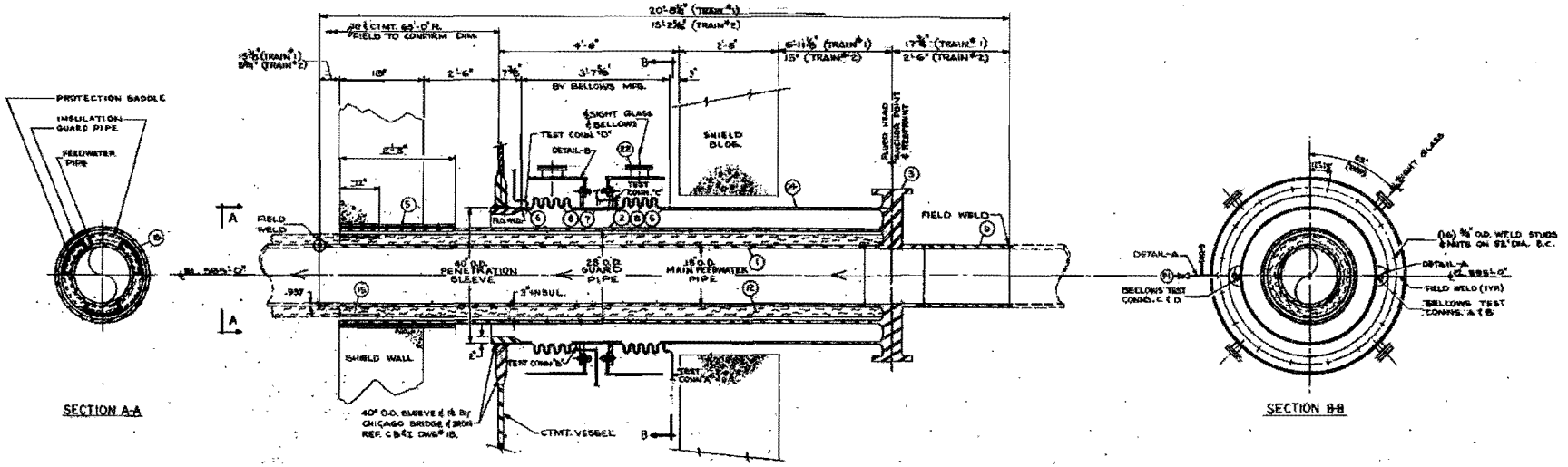

MAIN FEEDWATER TO STEAM GEN.
SCALE: 1" = 1'-0"
PEN. # 36, TRAIN "A"
PEN. # 37, TRAIN "B"

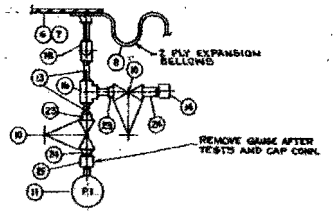

DETAIL-A
TYP. 8 PLACES
FOR TRUE ORIENTATION OF BELLOWS TEST CONNECTION SEE SECTION B-B

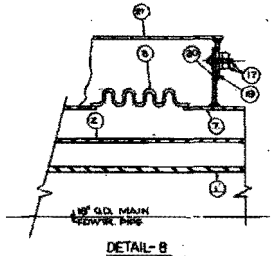

DETAIL-B
SCALE: 1" = 1'-0"
DETAIL OF BELLOWS PROTECTIVE SHUT SLEEVE.

MAIN FEEDWATER - BILL OF MATERIAL

ITEM	REQ'D	DESCRIPTION	MATERIAL	SPECIFICATION	CLASS	WEIGHT (LBS.)	CODE	WELDED	HEIGHT LOC.	REMARKS
1	1	PIPE-18" O.D. x .937" WALL	STL.	M-170 & SMLS-A106	E&S	1155	ASME SEC III NC	YES		
2	1	PIPE-25" O.D. x 1.058" WALL	STL.	M-170 & SMLS-A106	E&S	1155	ASME SEC III NC	YES		
3	1	FLUED HEAD	FOR STL.	M-252		1159	ASME SEC III NC	YES		
4	1	40" O.D. PIPE X .375" WALL	STL.	M-252 & SMLS-A106	H&S	49	ASME SEC III NC	YES		
5	1	54" OD. SLEEVE X .375" WALL	STL.	CC-8		-		NO		
6	2	40" O.D. PIPE X .375" WALL	STL.	M-252	H&S	49	ASME SEC. III NC	YES		
7	1	40" O.D. PIPE X .375" WALL	STL.	M-252	H&S	49	ASME SEC. II, NC	YES		
8	2	40" I.D. - 2 PLY BELLOWS	S.S.	M-280 &		99	ASME SEC. III NC	YES		
9	1	PIPE-18" O.D. X .937" WALL	STL.	M-252 & SMLS-A106	E&S	1155	ASME SEC III NC	YES		
10	0	GLOBE VALVE, 600# STD.	STL.	M-218A (D-70)		95	ASME SEC III NC	YES		FURNISHED BY CLIENT
11	4	PRESSURE GAUGE		M-198		99		NO		
12		3" THK. INSUL. ON 18" O.D. PIPE	THERMOCOUPLE	M-197A		-	ASTM C 533 TYPE I	NO		CBI WHITE-X-TA
13		NOM. 80 SMLS. PIPE	S/STL.	M-252		45	ASME SEC III, NC	YES		
14	4	3/4" 3000 LB. SCRD. CAP	STL.			49		NO		FURNISHED BY CLIENT
15	3	[illegible]	STL.	M-190		-	ASME SEC VI NC	YES		
16	4	18"-3000 TEE	S/STL.	M-252		95	ASME SEC III NC	YES		
17	32	3/4" OD. WELDED STUDS & NUTS	STL.	M-253		-		NO		
18	8	18"-90° ELBOW	S/STL.	M-252		69	ASME SEC II, NC	YES		
19	4	48"-I.D. x 50"-O.D. x 3/4" R. FLANGE	STL.	M-235		-		NO		SPLIT FOR FIELD INSTALLATION
20	2	40" I.D. x 56"-O.D. x 1" R. FLANGE	STL.	M-203		-		NO	" " "	" " "
21	2	58" O.D. x 57 1/2" THICK SLEEVE	STL.	M-203		-		NO	" " "	" " "
22	4	SIGHT GLASS, 3000 LB. CL. 316 SS		M-255		-		NO		
23	6	3/4"-1/4" 3000 LB. S.W. RED. INSERT	STL.			45		YES		FURNISHED BY CLIENT
24		36" SCH. 80 SMLS. PIPE	STL.			49		NO	" " "	" " "
25	4	3/4"-1/4" 3000 LB. SCRD. RED.	STL.			49		NO	" " "	" " "

REFERENCE DWGS:
7749-M-307C - MAIN FEEDWATER, AUXILIARY & CONTAINMENT BUILDING.
7749-C-281 MAIN FEEDWATER LINE RESTRAINTS PLAN & DETAILS.
7749-C-284 THRU C-287 - MAIN FEEDWATER LINE MISC. RESTRAINT DETAILS.

NOTES:
1. LOCATION OF & OF PENETRATION NOZZLE HAS ½" TOLERANCE AROUND TRUE & AND RADIAL TOLERANCE OF CONTAINMENT VESSEL IS ±2½".
2. BILL OF MATERIAL IS FOR ONE ASSEMBLY. TWO ASSEMBLIES REQ'D.
3. FOR DETAILS OF THE BELLOWS ASSEMBLY SEE DWGS. 7749-M-255-S & 4.
4. CALCIUM SILICATE, BLACK AND CELLULAR FIBER BLANKET MATERIAL IS CURRENTLY INSTALLED IN PORTIONS OF BARK PENETRATION. FUTURE REMOVAL, REINSTALL OR INSTALLATION OF THESE MATERIAL SHALL BE TO THE REQUIREMENTS OF SPECIFICATION M-N-166. (CBI, B.E.P. Dwg. 0178-001)

NO.	DATE	REVISION	BY	CK	APP'D
4	5-14	INC. SCOPE OF W.O. 1 PER FCR [illegible]	MF	MF	[illegible]
3	3-14	INC. FOR ECO.	MF	MF	[illegible]
2	7-13	NOTE ADDED AT F-4.	FH	MF	[illegible]
1	6-13	NOTE 3 ADDED	MF	MF	[illegible]
0	5-13	ISSUE AS PER W.O. 1 PER FCR CHANGE FOR CONSTRUCTION	MF	MF	[illegible]

DRAWN [illegible] NOTED [illegible] E.S. [illegible] L.L.

BECHTEL COMPANY
[illegible] MARYLAND

BARNS-BESSE NUCLEAR POWER STATION
THE TOLEDO EDISON COMPANY
THE CLEVELAND ELECTRIC ILLUMINATING COMPANY

MAIN FEEDWATER
PENETRATION DETAILS

SCALE	DRAWING NO.	REV.
7749	M-284B	4

Exhibit 71: Comparison of Toledo Blizzards

COMPARISON OF SNOWFALL, WIND SPEED AND TEMPERATURE FOR MAJOR BLIZZARDS IN THE TOLEDO, OHIO AREA

EVENT	SNOWFALL 20 DAYS PRIOR (INCHES)	SNOWFALL DURING (INCHES)	MAX WIND (MPH)	LOW TEMPERATURE (DEG F)
BLIZZARD 1977	9.1	4	84 (gust) 78 (avg., est.)	-8, (850mb) -2, (surface)
BLIZZARD 1978	21.5	12	105	-24 (850mb) -5, (surface)
BLIZZARD 1994	11.9	3.5	45(avg., est.)	-17, (surface)

Exhibit 72: Water and Moisture Transfer into Concrete

Water and Moisture Transport Processes in the Concrete Wall

1. Water and moisture transport mechanisms in concrete

There are two types of moisture transport processes in Davis Besse containment structure that may possibly affect the ice-induced delamination. One may be called "top-down moisture transport", and the other may be called "Horizontal moisture penetration into the concrete". The first one resulted in high moisture content near rebar region. When temperature decreases, the moisture near rebars freezes, leading to the sub-mode 1 delamination cracking as described in FM 3.6 Freezing near Rebar in Blizzard. The second one caused high moisture content in the outer layer of concrete, which leads to the sub-mode 2 delamination cracking as described in FM 3.6. The following sections describe the two types of moisture transport processes in Davis Besse containment structure.

Mechanisms 1: Top-down moisture transport

The top-down moisture transport process assumes that the water comes from the top of the structure and slowly penetrates down within the concrete wall. The resulting cracking is delamination cracks in the wall caused by ice formation. Due to heterogeneous feature of concrete, the water comes down along random paths with the least resistance. That explains the sporadically distributed cracks in the wall. Patches of laminar cracks can distribute in a large area of the wall connected by narrow water paths behind the surface.

The identified areas of laminar cracking are detailed on Drawing C-111A. The document shows that the patches of cracks are generally located within the architectural shoulder areas of the Shield Building. The crack survey information also shows that in some shoulders the cracks are located a considerable distance (100+ feet below) from the top of the Shield Building wall. The cracks are also located in the top 20 feet of the cylinder wall.

Fig. 1 illustrates the top-down moisture transport process, which can be explained by using several evidences obtained during our investigation.

1. During the construction of the containment structure. The wall was built first and the dome was built two years and four months later. So, the jacking bars, dense rebars, and the top of the concrete wall were exposed to the environment. The two figures on the right side in Fig. 1 show the exposed wall, the dense rebars in the wall during construction, and dense rebars around the delaminated area. Many structures were built this way without any durability problem. In this structure, however, the initial defects may be generated by the jacking bars and dense rebars, together with the large aggregate used in the concrete. These factors resulted in high porosity concrete near the rebars and jacking bars, which formed a pathway for the water to penetrate down in the wall.

2. The cosmetic layer of rebars near the surface of wall was evenly spaced at 12". The concrete near the cosmetic rebars has good quality, and thus there is no delamination around this layer of rebars.

3. There is a flat concrete slab surrounding the dome (see the upper left figure in Fig. 1) where snow can stay for a long time in the winter after a snow storm. Slow melting of snow provides long-term ponding of water on the top of the wall. During the inspection, a part of flat slab was covered by water, as shown in the upper left figure in Fig. 1.

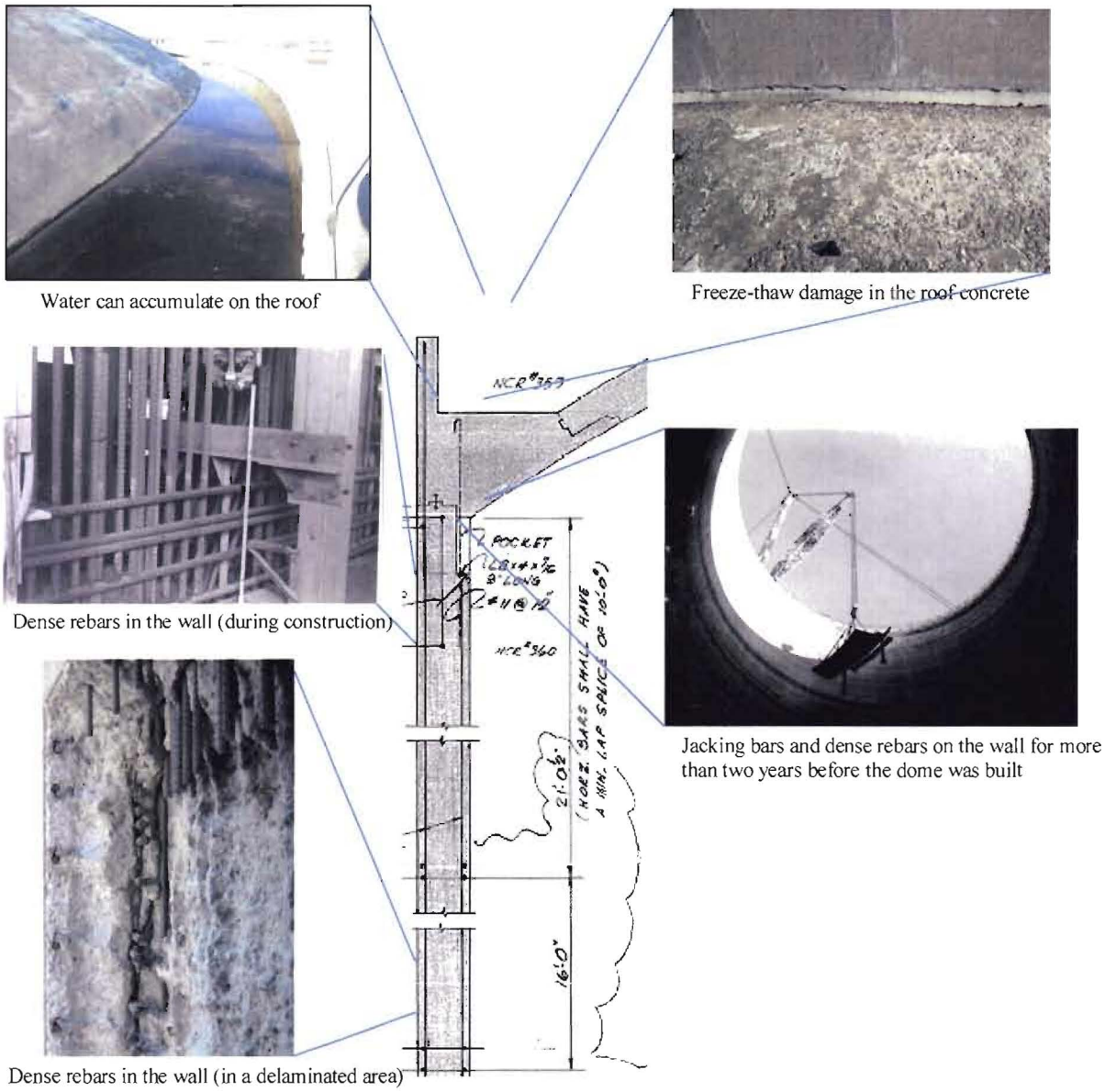

Fig. 1 Failure mode of Type 1 freeze-thaw damage in the wall

The concrete in the flat concrete slab exhibited typical sign of freeze-thaw damage (see the upper right figure in Fig. 1), such as scaling damage and cracking. Water can penetrate into the damaged concrete and slowly transport down to the concrete wall below. Because of heterogeneous concrete properties, the water penetration did not occur uniformly in the wall.

The penetration could be faster at one location and stopped at another location, which explain the random distribution of the delamination cracking in the wall. There is no theoretical model that can be used to quantitatively estimate the rate of this type of moisture penetration.

Mechanism 2: Horizontal moisture penetration into the concrete

This moisture transport process assumes that the moisture comes from the side surface of concrete wall and slowly penetrates horizontally into the wall. The concrete with high moisture content may expand when temperature decreases (as explained in FM 3.6 Freezing near Rebar in Blizzard, and in Exhibit 57 for temperature dependent coefficient of thermal expansion). The resulting cracking is delamination cracks in the wall caused by a combined action due to the expansion of outer layer of concrete as well as the contraction of inner layer of concrete. Similar to the top-down moisture transport process, the heterogeneous feature of concrete needs to be considered. More moisture will penetrate into the concrete wall in the locations where the resistance is low, and less moisture will penetrate into the concrete where the resistance is high. This explains the sporadically distributed cracks in the wall.

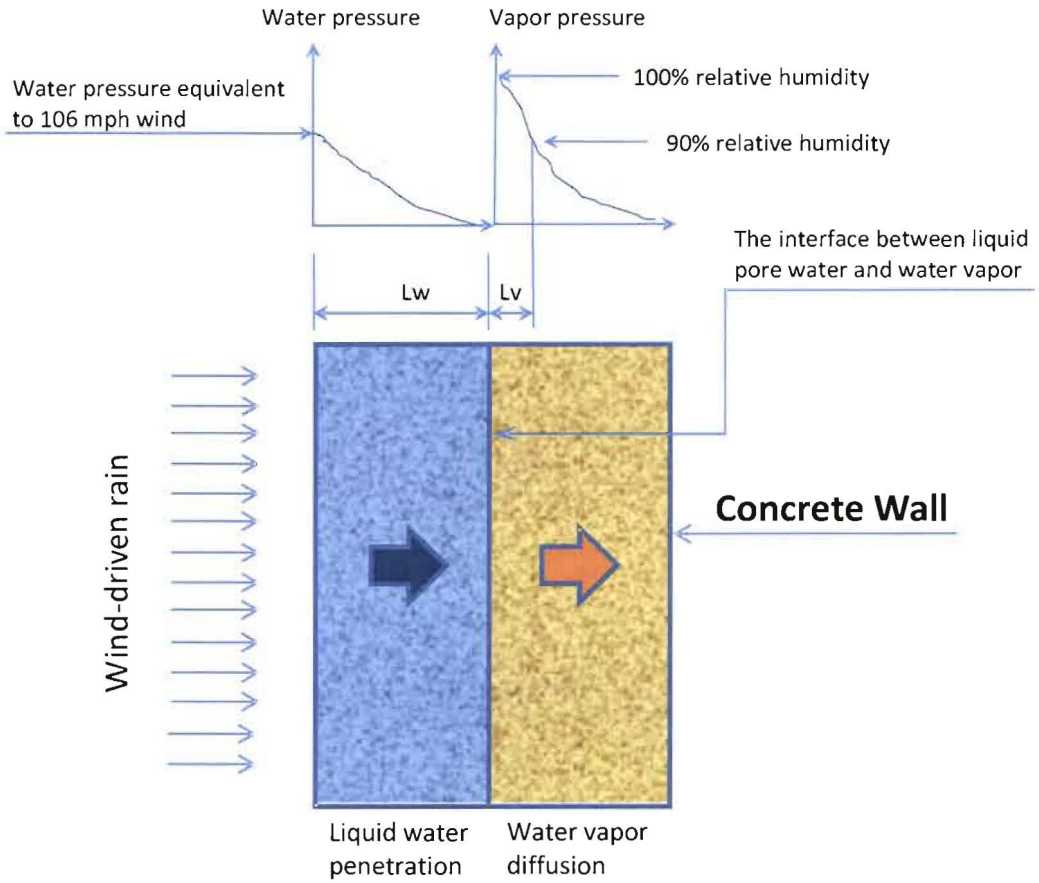

Fig. 2 Liquid water and moisture penetration into concrete due to wind-driven rain

For above ground concrete structures like Davis Besse containment structure, there is hardly any liquid water in the porous system in concrete under an arid environment, the moisture content of concrete can be described by pore relative humidity, and the water vapor diffusion is a dominant process which is driven by the humidity gradient from the location of high humidity to the location of low humidity. During a blizzard, the effect of wind-driven rain is an important factor to consider. On the outer surface of concrete wall, the rain water is pressed by the wind pressure and penetrates into concrete. The liquid water penetration is a dominant process which is driven by the wind pressure on the surface. Fig. 2 shows the two transport processes in a concrete wall during a blizzard. The blue region represents the outer layer of concrete in which pores are saturated by liquid water, which may be called water region, and the yellow region stands for the inner layer where vapor water dominant, which may be called vapor region. The interface between the two regions is simplified as a line in this study, and in reality, the interface is a zone with a finite depth for the transition of the two regions.

The entire depth of the water region is shown in Fig. 2 as Lw (on the left), which is important for our study. The partial depth of the vapor region, say higher than 90% pore relative humidity is shown as Lv (on the right), which is also important for our study. The sum of the two depths is called Lm, representing the depth of concrete with high moisture content:

$$Lm = Lw + Lv \tag{1}$$

In Section 2.1, Lw will be estimated by a theoretical model for liquid water transport in concrete taken into account the wind-driven rain effect on the surface of concrete water. In Section 2.2, Lv will be estimated by a theoretical model for water vapor diffusion in concrete. The two estimations need several important transport parameters such as water permeability and moisture diffusivity, which are not available for Davis Besse concrete. So, the material parameters will be calculated by using available material models in the literature. Lm calculated from the estimated Lw and Lv will be compared to moisture profiles measured in a concrete sample from Davis Besse power station. The comparison also serves as a calibration of the material parameters used in the two theoretical models. The calibrated models can be used to better predict water and moisture transfer in the concrete during blizzards and other conditions.

2. Analytical model for liquid water transport in concrete

The liquid water penetration process due to wind-driven rain is a very complicated process, which has been modeled by using coupled partial differential equations (Tariku et al. 2007). In this study, because of limited time, we used a simplified approach which is described by the following governing equation similar to heat conduction:

$$\frac{\partial W}{\partial P}\frac{\partial P}{\partial t} = K_P \frac{\partial^2 P}{\partial x^2} \tag{2}$$

in which P = water pressure in concrete pores in psi; W = water content in concrete in gram of water per gram of concrete; t = time in hour; and x = the depth into the concrete wall in inches; $\partial W/\partial P$ = water capacity in 1/psi (because W is a weight ratio), it is similar to the term of $\rho_c c$ in heat conduction where ρ_c is the density of concrete and c is heat capacity; and K_P = hydraulic

conductivity with a unit of $in^2/(psi.hr)$. From Eq. (2), K_P is related to pressure gradient of water in pores of concrete. The water penetration equation, Eq. (2), can also be written as

$$\frac{\partial P}{\partial t} = K_W \frac{\partial^2 P}{\partial x^2} \tag{3}$$

in which K_W = water diffusivity, similar to the thermal diffusivity for heat conduction. The unit for K_W is in^2/hr.

$$K_W = \frac{K_P}{\partial W / \partial P} \tag{4}$$

It should be noted that $\partial W/\partial H$ already includes the density of concrete ρ_c. Eq. (3) can be solved with given boundary condition and initial condition to obtain a water pressure distribution in concrete at any location and at any time. The boundary condition P(t, 0) = P_b and the initial condition P(0, x) = P_0 must be prescribed first. P_b represents the water pressure on the surface of concrete wall due to wind-driven rain, and P_0 represents the initial water pressure in the concrete. In order to find the internal water pressure distribution, the boundary condition and the material parameters must be determined first. Then, the depth of water region in Eq. (1), Lw, can be determined which is the distance from the surface to a location where the water pressure is considered to be low.

The boundary condition – Water pressure due to wind-driven rain

Wind-driven rain (WDR) has a significant effect on moisture content in building envelops. WDR intensity increases with wind speed (Hens 2010). RILEM tube method was developed to test the resistance of a building envelop to WDR, as shown in Fig. 3. The tube is designed to be attached to a vertical wall. The water level in a tube is used to simulate the pressure of WDR at various wind speeds.

RELATIONSHIP BETWEEN TUBE WATER LEVEL AND WIND SPEED

Graduation Mark (ml)	Theoretical Wind Speed (mph)
0	98.1
0.5	94.1
1.0	90.04
1.5	85.7
2.0	81.1
2.5	75.2
3.0	71.1
3.5	65.5
4.0	59.4
4.5	52.8
5	44.8

Fig. 3 RILEM tube tester and relationship between water level and wind speed (Crissinger 2005)

When the water level reaches the top of tube at graduation mark 0 as shown in Fig. 3, the corresponding wind speed is about 98.1 mph, which is a high Category 2 hurricane (Crissinger 2005). At this water level, the height of water is 12 cm, and the corresponding pressure is 0.17 psi. This pressure level is used in our analysis as the boundary condition.

[redacted]

The hydraulic conductivity K_P

From Eq. (4), we need to first determine K_P, the hydraulic conductivity, and $\partial W/\partial P$, the water capacity. K_P can be expressed in two different ways as

$$K_P^p = \frac{k}{\eta} \tag{5a}$$

$$\text{or} \quad K_p^h = \frac{k}{\eta}\rho_w g \tag{5b}$$

in which k = intrinsic permeability with a unit of in^2, which is the basic permeability of the material independent from the permeating media; and η = viscosity of fluid (water) in psi.s. Viscosity of water $\eta = 0.001 Pa.s = 4.028 \times 10^{-11}$ psi.hr. It is important to note that K_P as defined in Eq. (5a), K_P^p, is related to pressure gradient, the superscript p is for pressure, and its unit is in^2/psi/hr. This K_P is used as the field variable in our formulation of the governing equation, Eq. (2). On the other hand, K_P is often defined as in Eq. (5b), K_p^h. It is related to the height of water column, the superscript h is for the height of water column, and its unit is in/s.

Various test methods were developed for K_P^p and K_p^h: pressurized methods for K_P^p or water column methods for K_p^h. The different testing methods resulted in different K_P. For the pressurized methods, the water flux J is proportional to the pressure gradient, $J = K_P^p(\Delta P/L)$, where L is the thickness of specimen. For the water column methods, the water flux J is also proportional to the pressure gradient, which is expressed by the height of water column, $J = K_P^h(\Delta h/L)$. So, if a K_p^h with the unit of in/s is available for a concrete, the value must be converted to in^2/psi/hr in order to be consistent with the definition of Eq. 5(a) for the analytical solution used in this study (will be described later). The conversion is

$$K_p^p = \frac{K_P^h}{\rho_w g} \tag{5c}$$

The value of K_p^h varies in a very large range depending on the type of aggregate and water-cement ratio of the concrete. Mehta and Monteiro (1993) indicated that with different type of

aggregate, K_p^h may vary more than 1000 times for different concretes (see Table 5-2 of the reference).

In the case that the intrinsic permeability k is available, Eq. (5a) can be used. However, the intrinsic permeability k for Davis Besse concrete is not available. So, available test data in the literature will be used as reference in this study. As an example, the test data of k by Nehdi (1995) is $k = 3.875 \times 10^{-10}$ in^2 (25×10^{-14} m^2) for a concrete with w/c = 0.5, entrained air = 2%, and fc'= 6400 psi (44.2 Mpa) at 91 days, and thus $K_p^l = 9.62$ in^2/psi/hr. Another example is from the test results of Wang et al. (1997). They showed that K_p^h depends on the width of crack in concrete and it is in the range of 1×10^{-9} cm/s to 1×10^{-2} cm/s when the width of crack is between 0 to 500 μm (see). As one can see, the permeability values of distressed concrete vary in a very large range.

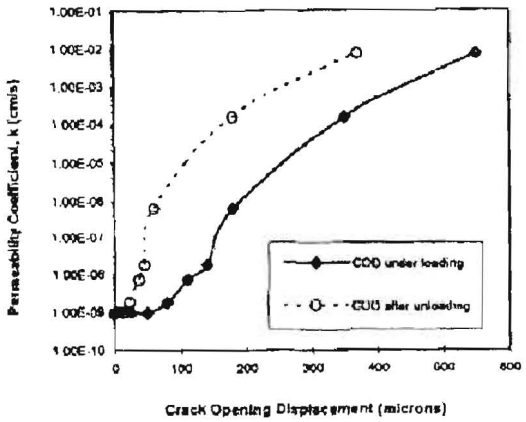

Fig. 4 Relationship between water permeability and crack widths (Wang et al. 1997)

[redacted]

[redacted]

The depth of water region Lw

Using the boundary, condition, initial condition, and material parameters derived above, and a 1D solution for Eq. (3) can be obtained

$$P(t,x) = P_b - (P_b - P_0)\,erf\left[\frac{x}{\sqrt{4K_{II}\cdot t}}\right] \tag{8}$$

in which erf is the error function. Fig. 5 shows that after 4 days and 16 days continuous wind-driven rain at wind speed 106 mph and 20°C, the internal water pressure distributions in a concrete [redacted]

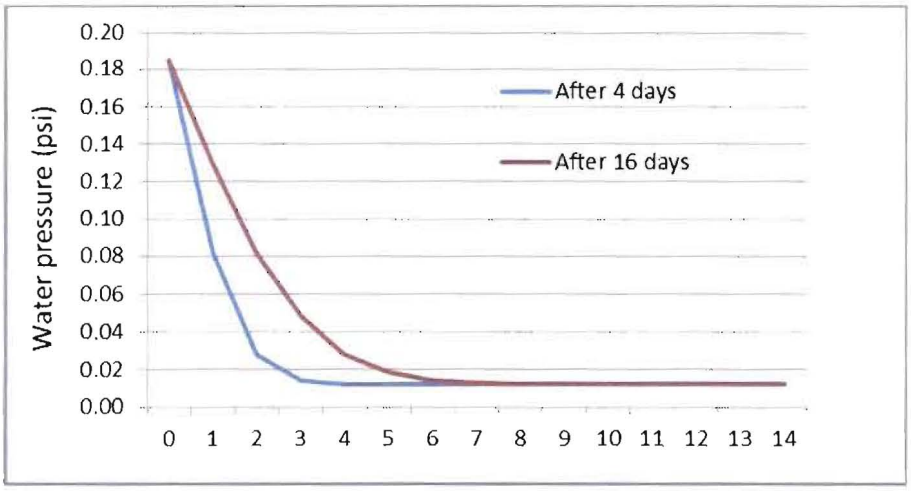

Fig. 5 Water pressure distributions in the concrete [redacted].

The transport parameters of Davis Besse concrete are not available. [redacted] During the 1978 blizzard, assuming average T = 0°C and wind speed of 98 mph, we obtained $K_{II} \approx 0.00193$ in^2/hr. and the two curves shown in Fig. 6

for water pressure distributions after four days and 16 days continuous wind-driven rain. From Fig. 6, we can see that Lw is about two inches after four days and about three inches after 16 days wind-driven rain.

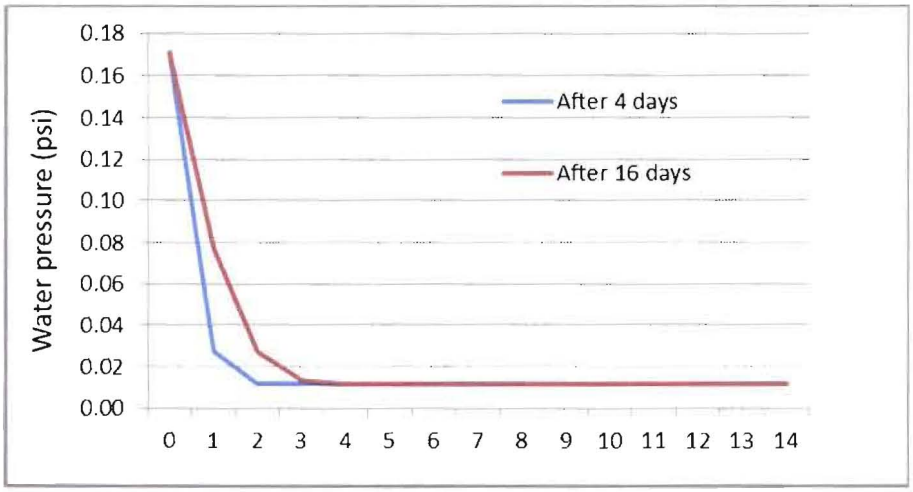

Fig. 6 Water pressure distributions in the concrete with water diffusivity $K_W = 0.00139$ in^2/hr. under T = 0°C and wind speed = 98 mph.

3. Analytical model for water vapor transport in concrete

Water vapor transport is driven by moisture concentration gradient. The moisture concentration is represented by pore relative humidity on concrete. The boundary (the starting point) of moisture diffusion is the interface between the water region and vapor region shown in Fig. 2, where the humidity boundary condition can be assumed to be 100%. This is actually a quite complicated problem, because the boundary (the interface) is not fixed, but moves to the right of the figure, depending on the depth of the water region. In this study, due to the tight schedule, the moving boundary problem is simplified as a one-dimensional moisture diffusion problem as described below.

The governing equation for the 1D moisture diffusion in concrete is (Xi et al. 1994a, 1994b):

$$\frac{\partial W}{\partial H}\frac{\partial H}{\partial t} = K_H \frac{\partial^2 H}{\partial x^2} \tag{9}$$

in which $\partial W/\partial H$ = moisture capacity in gram of moisture per gram of concrete, which is similar to the heat capacity $\rho_c c$ in heat conduction; and K_H = coefficient of moisture diffusion, similar to the thermal conductivity. The unit of K_H is in length^2/time, depending on the test data used for determining the parameter (will be explained later in detail). The subscript H is used here to represent humidity in concrete. The moisture diffusion equation can also be written as

$$\frac{\partial H}{\partial t} = D_H \frac{\partial^2 H}{\partial x^2} \tag{10}$$

in which D_H = moisture diffusivity, similar to the thermal diffusivity. The unit for D_H is the same as K_H because W and H are weight ratio and pressure ratio, respectively, and thus have no unit.

$$D_H = \frac{K_H}{\partial W / \partial H} \tag{11}$$

It should be noted that $\partial W/\partial H$ already includes the density ρ_c. Eq. (10) can be solved to obtain a moisture distribution in concrete at any location and at any time, which will be described in later sections. The boundary condition H(t, 0) = H_s and the initial condition H(0,x) = H_0 must be prescribed. In this study, H_s represents the relative humidity at the interface, 100%; and H_0 represents the initial relative humidity in the concrete. In order to find the internal moisture distribution from Eq. (10), the material parameters must be determined first.

Moisture capacity and coefficient of moisture diffusion

Moisture capacity of concrete is not a constant but a function of H. Fig. 6 shows the effects of water-to-cement ratio, w/c, and H on the moisture capacity (Xi et al. 1994a). The moisture capacity is highly nonlinear with respect to H. In fact, D_H depends on H as well, which will be shown later.

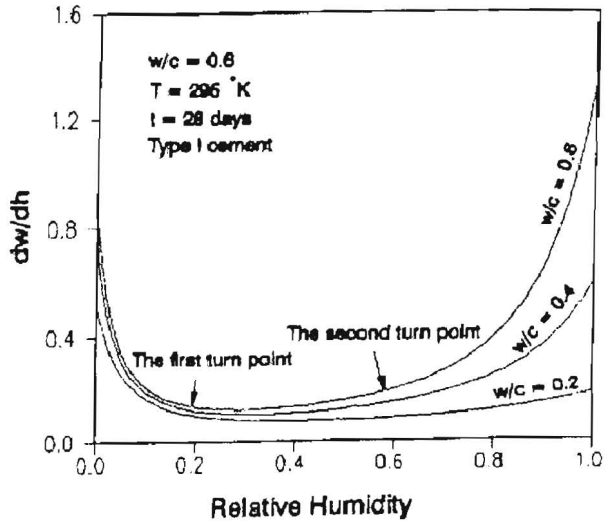

Fig. 6 The effects of water-to-cement ratio and H on the moisture capacity.

[redacted]

[redacted]

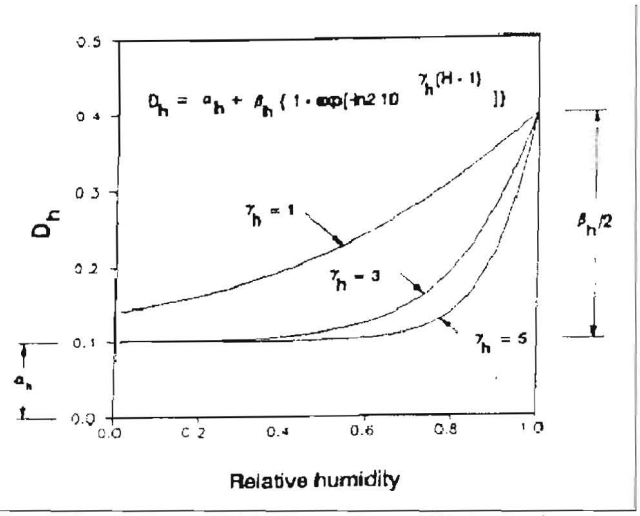

Fig. 7 The effect of relative humidity on the coefficient of moisture diffusion

[redacted]

As a summary, in the following moisture transport analysis

- The density of concrete ρ_c = 2400 kg/m^3 = 0.0868 lb/in^3
- $\partial W/\partial H$ / ρ_c = 0.35/0.0868 = 4.032 in^3/lb
- The coefficient of moisture diffusion K_H = 0.146 cm^2/day = 0.00094 in^2/hr.
- The moisture diffusivity D_H = 0.417 cm^2/day = 0.00269 in^2/hr.

The depth of vapor region Lv

At the interface H_s = 100%, and at the deep part of the wall H_0 = 70%, and the solution of Eq. (10) is

$$H(t,x) = H_s - (H_s - H_0)\text{erf}\left[\frac{x}{\sqrt{4D_H t}}\right] \tag{15}$$

in which $H(t,x)$ is the humidity distribution in the concrete at time t and depth x starting from the interface. The two curves for after 4 days and 16 days of WDR are shown in Fig. 8.

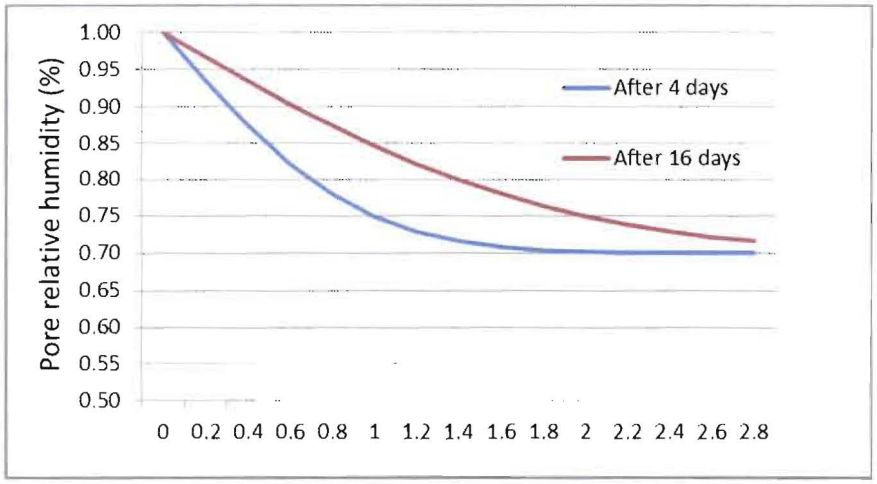

Fig. 8 Internal humidity profiles in the vapor region after 4 days and 16 days of WDR H_s = 100%, H_0 = 70%, and the moisture diffusivity D_H = 0.00269 in^2/hr.

Since only the high moisture region has effect on ice formation, we are interested in the depth from 100% to 90% relative humidity. The depth of high vapor density region is 0.3 in. after 4 days and 0.6 in. after 16 days of WDR.

After a major blizzard, the effect of WDR will disappear, but the moisture will stay in the wall in the water region if outside temperature is low. So, the depth of water region will remain more or less the same, while the depth of vapor region will increase because of continuous diffusion of moisture from the water region to deeper part of concrete. Neglecting the temperature effect,

Fig. 9 shows two curves of moisture distribution 20 and 80 days after a WDR. The depth of high vapor density region is 0.75 in. after 20 days and 1.5 in. after 80 days of the WDR.

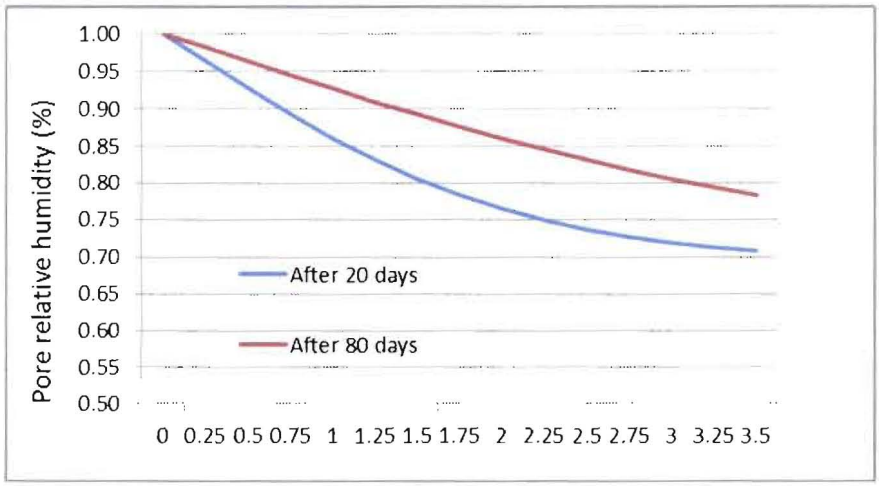

Fig. 9 Internal humidity profiles in the vapor region 20 and 80 days after a WDR $H_s = 100\%$, $H_0 = 60\%$, and the moisture diffusivity $D_H = 0.00269$ in^2/hr.

4. The depth of high moisture region Lm = Lw + Lv

The material models used in the water and vapor transport analyses were developed not based on Davis Besse concrete, because the transport parameters for the concrete are not available. Considering the large variation in the transport parameters, the variation of model predictions must be taken into account. One possible variation is the effect of aggregate and air-entraining agent used in Davis Besse concrete, which may increase the moisture diffusivity and thus increase the rate of moisture penetration (Xi 1995a, 1995b). An important variation is the distress in the concrete wall such as the surface cracking as shown in Fig. 4. The effect of internal damage on concrete diffusivity was analyzed by many researchers (see for example Xi and Nakhi 2005).

As a summary, the depth of water region Lw is much higher than that of vapor region Lv. Based on above preliminary and approximate analyses for solid concrete without major distress, the depth of high moisture region Lm is about 2 to 3 inches after a few days of WDR. This may be considered as a reference or guideline for determining the depth of high moisture region in the concrete wall. The present results are based on 1D analyses. The concrete in shoulder areas is subjected to 2D moisture penetration, and thus the high moisture region Lm in shoulder areas may be higher than that in the wall between shoulders.

References

1. Crissinger, J.L. (2005) "Measuring Moisture Resistance to Wind-Driven Rain Using a RILEM Tube", *Interface*, Nov., 4-11.

2. Hens, H. (2010) "Wind-Driven Rain: From Theory to Reality", *Buildings XI*, ASHRAE, 1-10.

3. Mehta, P.K., and Monteiro, P.J.M. (1993) "Concrete: Structure, Properties, and Materials", Prentice Hall Inc., Englewood Cliff, NJ 07632.

4. Nehdi, M., Aitcin, P.C., and Perraton, D. (1995) "Investigation of the Performance of Mass Concrete Using in Situ Permeability Tests", *Concrete Under Severe Conditions: Environment and Loading*, Vol. 1, Editors:P K. Sakai, N. Banthia, and O.E. Gjorv, E& FN Spon, 413-422.

5. Tariku, F., Cornick, S.M., and Lacasse, M.A. (2007) "Simulation of Wind-Driven Rain Penetration Effects on the Performance of a Stucco-Clad Wall", *Buildings X*, ASHRAE, 1-10.

6. Wang, K., Jansen, D., Shah, S.P., and Karr, A. (1997) "Permeability Study of Cracked Concrete," *Cement and Concrete Research*, 27(3), 381–393.

7. Xi, Y., Bazant, Z.P., and Jennings, H.M. (1994a) "Moisture Diffusion in Cementitious Materials: Adsorption Isotherm", *Journal of Advanced Cement-Based Materials*, 1, 248-257.

8. Xi, Y., Bazant, Z.P., and Jennings, H.M. (1994b) "Moisture Diffusion in Cementitious Materials: Moisture Capacity and Diffusivity", *Journal of Advanced Cement-Based Materials*, 1, 258-266.

9. Xi, Y. (1995a) "A Model for Moisture Capacities of Composite Materials - Formulation", *Computational Materials Science*, 4, 65-77.

10. Xi, Y. (1995b) "A Model for Moisture Capacities of Composite Materials - Application to Concrete", *Computational Materials Science*, 4, 78-92.

11. Xi, Y. and Nakhi, A. (2005) "Composite Damage Models for Diffusivity of Distressed Materials", *J. of Materials in Civil Engineering*, ASCE, May/June, 17(3), 286-295.

Exhibit 73: Laminar Cracking due to 1978 Blizzard

Laminar Cracking due to 1978 Blizzard

Table of Contents

Summary of Results

The results of the analysis presented in this report can be summarized as follows:

- Cracking is predicted due to the 1978 blizzard given the following assumptions:
  - Temperatures 20°F above calculated "worst case" temperatures (-24°F ⇒ -4°F)
  - Nonlinear CTE curve that is adapted from Exhibit 57 Figure 4
  - Saturation depths of at least 3"
  - Reduced effective fracture toughness of the concrete (discussed below)
- Cracking is not predicted due to the 1977 blizzard, even assuming worst case temperatures.
- The locations of the cracking remain confined to the observed crack locations under the thick sections of the shoulders and to locations where the horizontal rebar is spaced on 6" centers.

Modeling Summary

Overall Approach

The analysis results presented here is a result of many different modeling efforts combined. The convective heat transfer due to wind around the shield building was calculated using a computational fluid dynamics (CFD) model taking into account the wind velocity and direction. The surface roughness, the raised shoulder geometry around the flutes as well as the auxiliary buildings was included in the CFD model. A separate heat transfer analysis consisting of the free-standing reinforced concrete shield building, the free-standing steel containment vessel, and the annulus/hollow space between the two are included. The transient heat transfer model included the duration of two or three days in order to reach accurate temperature predictions. Effects included are solar radiation (tracking of the azimuth and elevation of the sun), the ambient temperature variation from meteorological data, and the temperature on the inside of the steel containment vessel. The details of the wind and thermal modeling are reported separately in the Root Cause Analysis Report.

The calculated temperature distribution in the reinforced concrete shield building is mapped to the Abaqus Global Model. A coupled temperature-displacement analysis for each temperature condition is performed using the Abaqus Global Model. [redacted]

Gravity is omitted [redacted]. It is expected gravity would have relatively little effect on the results based on previous studies, which are summarized in Exhibit 64 – Thermal Stress Analysis with Gravity and Wind Load.

Finite Element Software

Abaqus version 6.10 for Linux 64-bit was used exclusively to solve the finite element analysis models presented here. Abaqus is generally considered the gold standard for nonlinear analysis.

Scenarios Modeled

The following two scenarios are presented in this report. The details of the scenarios and the selection of the time of day are summarized separately in the Root Cause Analysis Report.

1) Low temperature and moisture intrusion during the 1978 blizzard
2) Low temperature and moisture intrusion during the 1977 blizzard

Background

Expansion of concrete due to freezing of entrapped moisture was studied [redacted]. This model implements the [redacted] material model. This is the same material model that was used to successfully predict and reproduce the laminar cracking observed in the containment of the Crystal River 3 nuclear power station. The [redacted] The horizontal rebars in the IF and OF rebar mats are modeled using solid elements, but as an approximation their cross-section is a 1" square, one element across. No other rebar is included in this model because doing so would be computationally prohibitive. This is an assumption made based on engineering judgment and is not expected to have a major impact on the results in this specific scenario because the laminar cracking near the OF rebar mat is driven by radial stresses and there are no radial rebars in the region where the cracks appear to initiate. Vertical stress components are also not expected to drive the damage, therefore the lack of vertical reinforcements [redacted] is assumed to be a justifiable simplification. Due to these simplifications, which are necessary to make the model computationally tractable, the detailed stress concentrations at the steel and concrete interface are not resolved in the model and therefore these results should be interpreted as a qualitative indication of where cracking is likely and not an absolute quantitative assessment of crack growth.

Global Model Description

The drawings used as geometry input for the global model are:

- Drawing No: C-100 Rev. 5 "Shield Building Foundation Plan & Details SH. 1"
- Drawing No: C-110 Rev. 6 "Shield Building Roof Plan Wall Section & Details"

All vertical reinforcing bars in the containment shell section are modeled as rebar #10 (diameter 1.270") at 12" center to center spacing. The inner face horizontal rebars are #8 (diameter 1.000") at 12" spacing. The outer face horizontal rebars are # 11 (diameter 1.410") at 12" spacing except in the top 20' of the walls, where the spacing is 6". The vertical and horizontal rebars in the shoulder sections are #8 at 12" spacing.

Material Properties

The material properties used as input to the finite element analysis in this report are summarized in the following documents attached to the Root Cause Analysis Report:

- Exhibit 56, Figure 2.1.4: Material Properties for Davis-Besse 3D Nastran Global Model
- Exhibit 56, Section 4.7: Effects of Variable CTE
- Exhibit 57: Temperature dependent coefficient of thermal expansion (CTE)

Material Properties specific to this analysis include the tensile strength (F_T) and the fracture toughness or "strain energy" (G_F). These are inputs to the Concrete Damaged Plasticity (CDP) material model, which was developed by Lee-Fenves and implemented natively in the Abaqus FEA software. The Lee-Fenves material model and the implementation in Abaqus are recognized to accurately predict cracking in concrete by the concrete modeling community. This technology is new to the nuclear industry.

The tensile strength of the Davis-Besse concrete was tested and found to vary from roughly 500 psi to 1000 psi with an average strength close to 900 psi. The test methods used to measure the tensile capacity will generally produce varying results depending on sample size and test method (e.g. split tensile vs. direct tensile). And, the samples used in these tests may have been too small for the standard test, thus over-predicted the strength. The strength of the concrete will also vary locally, with the concrete in the immediate vicinity of the rebars usually being weaker due to a higher void fraction in those areas. The samples were taken from regions away from the rebars (purposely to avoid the rebars). There is also some uncertainty in the modulus of elasticity. These models assumed E = 4.94Msi, when the stiffness may have actually been closer to 5.9Msi, which is about 20% higher and would increase the stresses by up to 20%. In this case, we assume an effective strength (tensile capacity) of F_T = 600 psi, which is toward the low end of the test results.

The fracture toughness ("strain energy", G_F) of the Davis-Besse concrete was not measured. Various values of G_F were tried and calibrated to the observed cracking. By means of comparison, the fracture toughness of the Crystal River concrete was estimated to be about 0.4 in-lb/in^2.

These values serve as starting points, F_T = 600 psi and G_F = 0.4 in-lb/in^2

Due to the known mesh size dependency in the Lee-Fenves material model, it is necessary to treat the measured strength parameters as starting points only. The mesh used for these models has very large elements relative to what the material model expects, and the stress concentrations are not fully developed. This inhibits cracking significantly. Therefore, it is necessary to use a lower set of strength parameters as an "effective strength" specific to the mesh. A sensitivity study is performed and a reasonable set of strength parameters is found to result in cracking of the concrete due to the conditions of the 1978 blizzard event. These strength parameters are F_T = 600 psi and G_F = 0.18 in-lb/in^2. These calibrated parameters are used in both the 1978 and 1977 cracking models to compare the relative severity of the two events. The parameters themselves are found to be well within the range of expected values for these parameters, which establishes this failure mode as having a high probability.

Coefficient of Thermal Expansion of High Moisture Concrete

The coefficient of thermal expansion (CTE) of high moisture concrete is a highly nonlinear function of temperature. This is associated with the 9% volume expansion of the freezing of entrapped water. The freezing of water in small pores in concrete takes place at a lower temperature than 32°F due to surface tension, which prevents the formation of ice at 32°F. The water in the concrete freezes at varying temperatures depending on the pore size. This creates a nonlinear dependence of the CTE with temperature. This is shown in Figure 1 and is a key input to the finite element analysis presented here. (Please see Exhibit 57 for a more detailed explanation of the nonlinear CTE.)

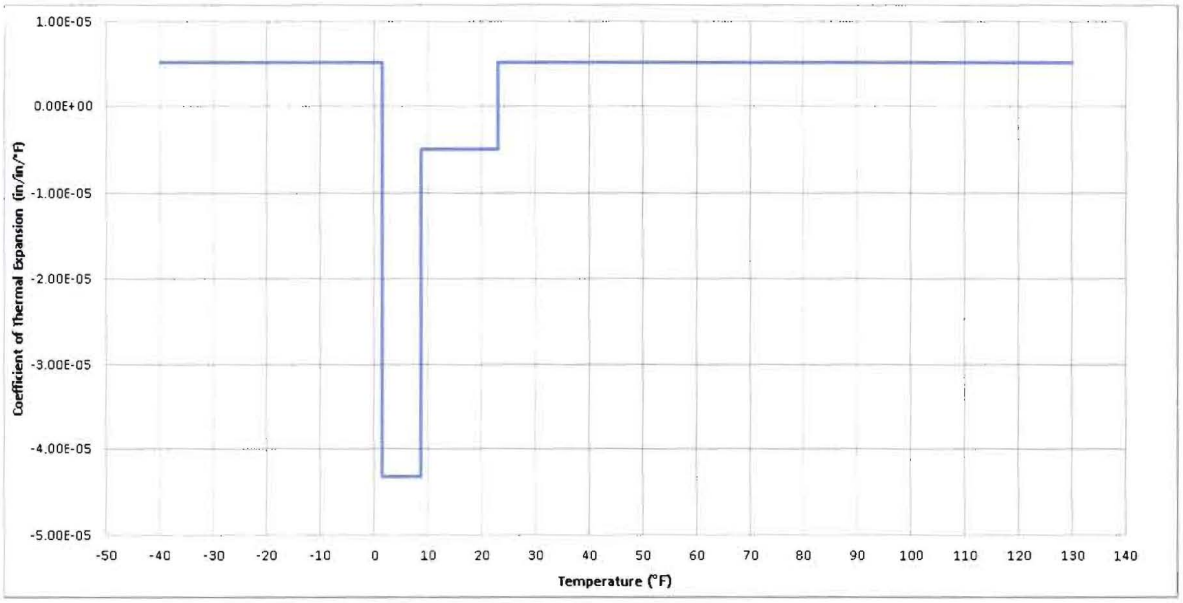

Figure 1 – Nonlinear CTE for Davis-Besse Concrete with 93% Moisture Content (See Exhibit 57)

Without having enough information to perform a thorough 3D moisture diffusion analysis on the Davis-Besse shield building model with measured properties taken from Davis-Besse concrete, it was necessary to make an assumption about the moisture gradient and proceed with that assumption in order to get a general qualitative response from the models. The most efficient way to do this was to assume that the moisture content gradients essentially match the temperature gradients. Rather than producing a constant depth of penetration, this produces a variable depth of penetration that takes into account the difference in the surface area to volume ratio in the shoulders.

The models assume that there are two regions. The two outermost contour regions are assumed to have a saturation of 93% (see Exhibit 57 Figure 4). This region is assigned the nonlinear CTE plotted in Figure 1. The calculation of the saturated depth is discussed in detail in Exhibit 72 "Water and Moisture Transfer into Concrete".

The rest of the structure is assigned the linear CTE of 5.2e-6, as found and discussed in Exhibit 56, Figure 2.1.4 (Material Properties for Davis-Besse 3D Nastran Global Model).

Tests of moisture penetration were also performed at the University of Colorado at Boulder, which showed that a 1-dimensional (1D) depth of water penetration up to 3 or 4 inches is possible when there are winds in excess of 90mph (such as during the 1978 blizzard). The 1978 models are calibrated so that the depth of penetration is approximately 3 to 4 inches in locations subject to 1D moisture diffusion. In the flute valleys, where there is a very low surface area to volume ratio, the depth is about 3 to 4 inches. In the "middle" of the walls between the shoulders, the depth is about 3.5 to 4 inches. In the corners of the shoulders, where there is a very high surface area to volume ratio, the depth of penetration transitions from 4 inches up to as high as about 14 inches in the corner. This is due to 2D moisture penetration in the shoulders, which appears to be highly significant. The 1977 models assume that the moisture depth of penetration is roughly half the 1978 case due to significantly less wind and precipitation in the 1977 case. Exhibits 66 and 71 summarize some key meteorological data during and prior to the blizzards of 1977 and 1978.

In the Results Section, Figure 7 shows the region that was assigned the nonlinear CTE as the two outermost thermal gradients (4°F to -4°F). Figure 10 shows the region that was assigned the nonlinear CTE for the 1977 case, the outermost thermal gradient (-4°F to -8°F). Depth of penetration is discussed in Exhibit 72.

Location of [redacted]

Figure 2 below shows the location of the [redacted].

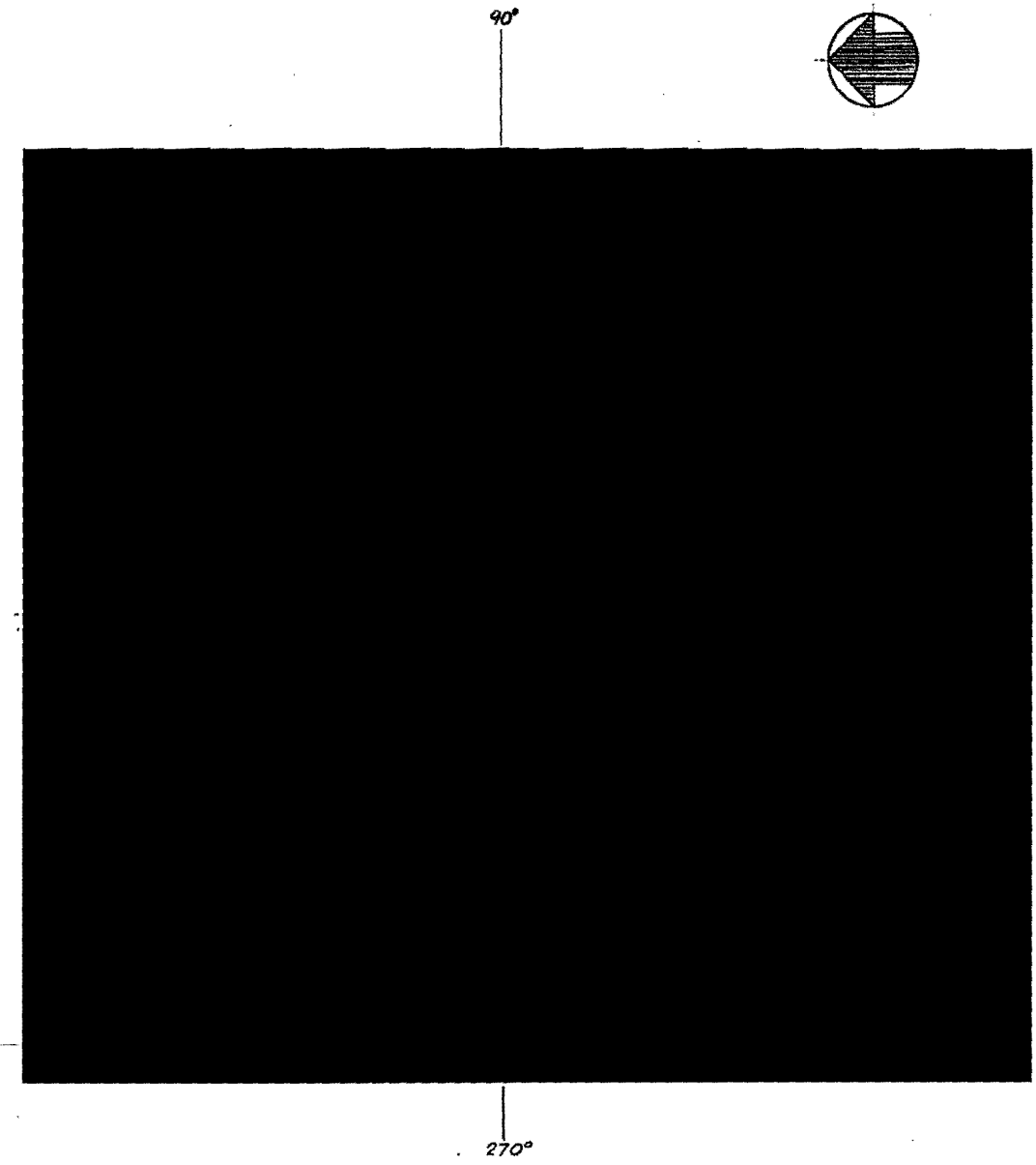

Figure 2 – Shield Building with Flute Numbers [redacted]

Circumferential Temperature Distribution at O.F. Horizontal Rebar

The temperature distribution in the [redacted] presented here were calculated in [redacted]. (See Exhibit 65) The temperature profiles around the Shield Building at the outer face horizontal rebars are shown in Figure 3. The models presented here use the worst case temperatures calculated for the 1978 blizzard with an offset of +20°F to simulate nominal temperatures. In this case, nominal temperatures will produce the most expansion and therefore the worst case stress condition for the building (see Figure 1). The +20°F offset brings the 1978 temperature gradients into rough equivalence with the lowest recorded ground temperatures during the 1978 blizzard (see Exhibit 66), which would be the expected low temperature condition assuming heavy cloud cover rather than a clear night sky (see Exhibit 65).

The 1977 blizzard model uses the worst case temperatures calculated for the 1977 blizzard with no temperature offset because the worst case 1977 temperatures are already in the range that will maximize expansion and cracking.

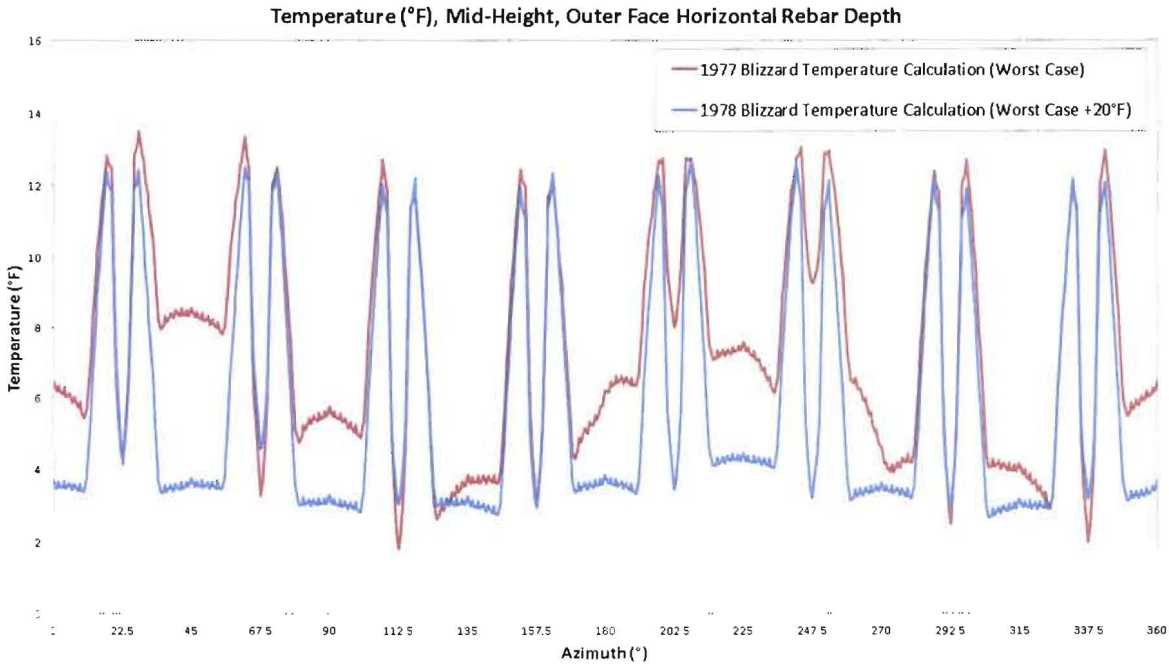

Figure 3 – Circumferential Temperature Distribution at the O.F. Horizontal Rebar Depth

[redacted] Description

In the [redacted].

[redacted].

Figures 4 through 6 depict the geometry [redacted].

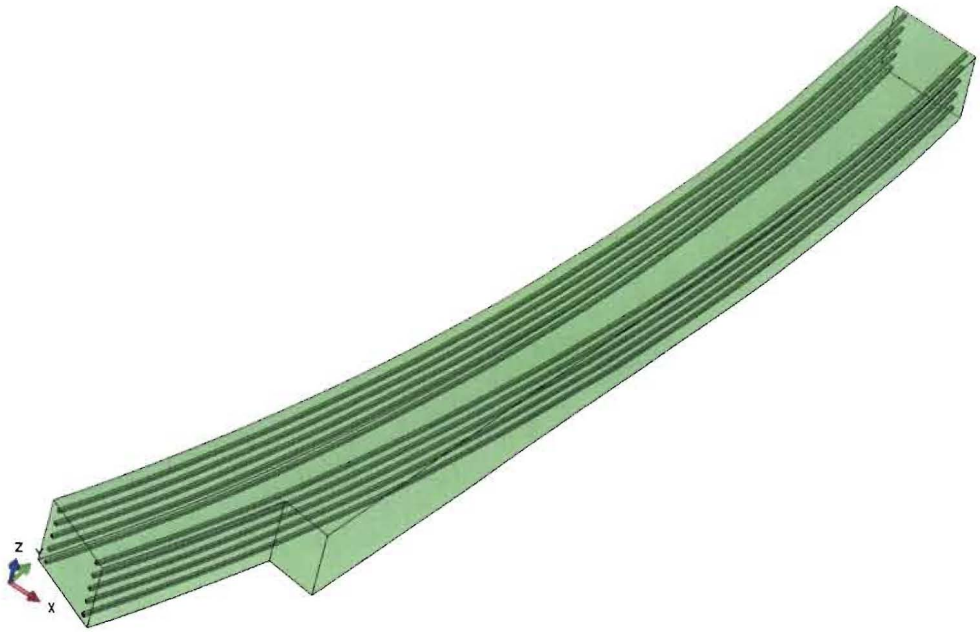

Figure 4 – [redacted]; Geometry and Rebars

Figure 5 – [redacted] Detail of Flute Region

Figure 6 – [redacted] Section View of Flute Region with Mesh

Discussion

The result [redacted] delamination propensity due to the two blizzard conditions, given the assumptions of the model.

The scale of damage ranges from 0 to 1 and represents the degree of tensile capacity lost from 0% to 100%. Any elements with red or magenta coloring are considered to have formed a structural crack, as they have less than 20% of their original strength left.

The damage that results from any tensile stress above the strength of the concrete depends on the 3D stress state as well as the strain energy available to open the crack. Low strain energy results in microcracks and high strain energy results in a structural crack.

[redacted] Results

The [redacted] model results shown in this section can be summarized as follows:

- The blizzard of 1978 scenario results in laminar cracking near the OF rebar mat.
- The blizzard of 1977 shows some damage (microcracking) relatively close to the surface of the shoulders, and significantly less damage compared to the blizzard of 1978.
    - It is important to point out that the distress in the concrete shoulder, predicted due to the conditions in 1977, could have also contributed to the damage in 1978 because distressed concrete can have a permeability that is 1,000 to 10,000 times higher than pristine concrete (see Exhibit 72). Thus, the assumptions being made in this analysis regarding depth of moisture penetration in the shoulders may actually be too shallow. And as a result, the analysis presented here may be under-predicting the laminar cracking concentrated beneath the shoulders. Note that this is true regardless of the actual depth of penetration during 1977, as less depth of penetration will primarily make the damage more shallow (closer to the surface), which will still have the potential to greatly increase the permeability of the concrete near the surface.
- The [redacted] Laminar cracks developed most prominently at the OF rebar mat under the thick shoulder regions and not in the thinner sections in the flute and shell.

1978 Blizzard Condition

The result due to the 1978 blizzard is shown in Figures 7 to 9. The temperature contours can be seen in Figure 7 and the cracking result is shown in Figures 8 and 9.

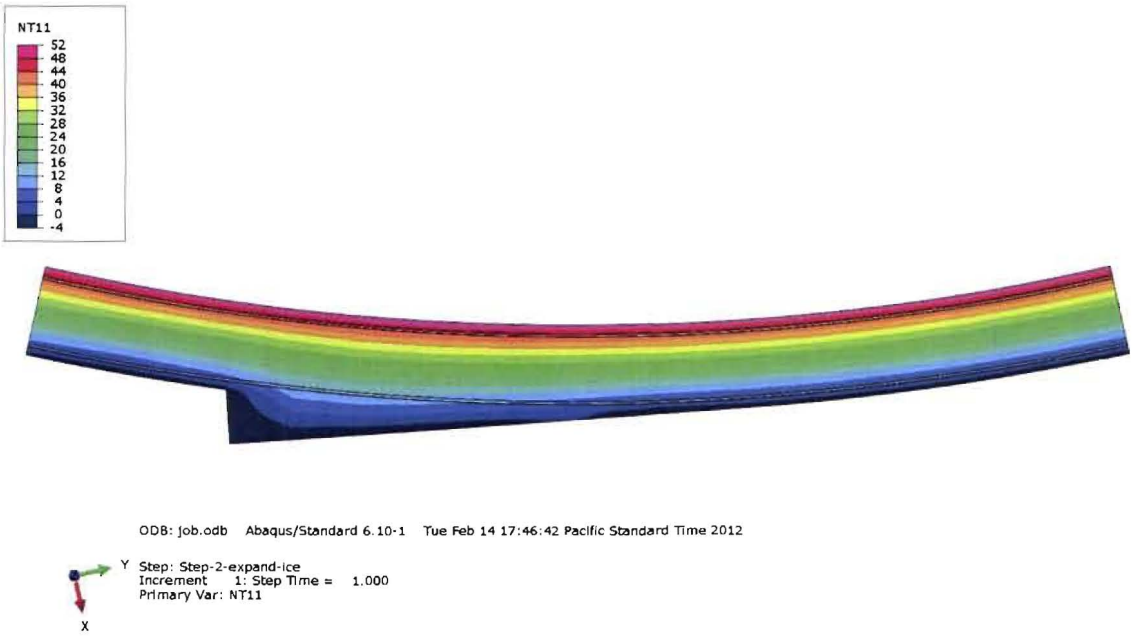

Figure 7 – Temperatures (°F) used in the 1978 Blizzard Analyses

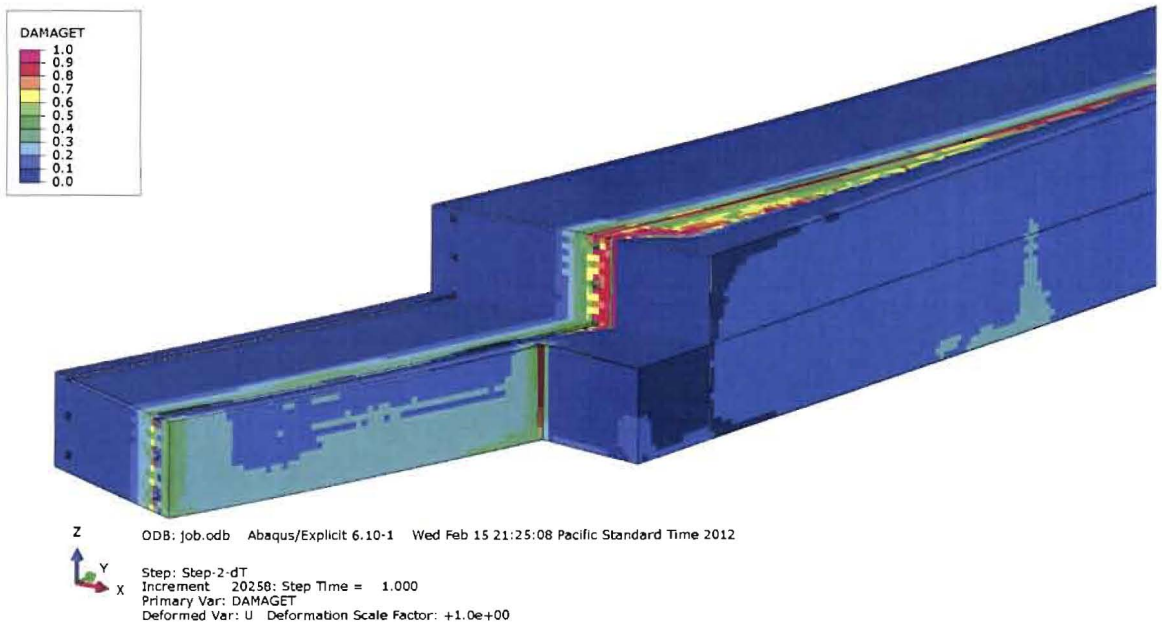

Figure 8 – Cracking Result due to 1978 Blizzard Conditions

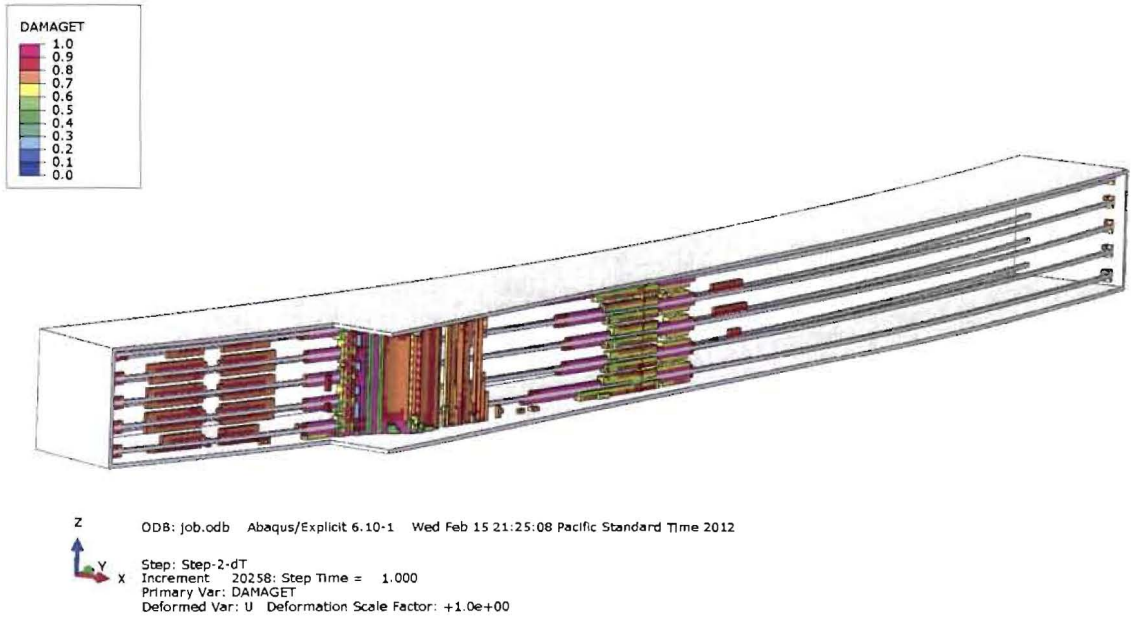

Figure 9 – Cracking Result due to 1978 Blizzard Conditions showing regions with DAMAGE > 0.7

1977 Blizzard Condition

The result from the [redacted] due to the 1977 blizzard conditions is shown in this section. Figure 10 depicts the temperature distribution in the [redacted] Figures 11 and 12 show the cracking result.

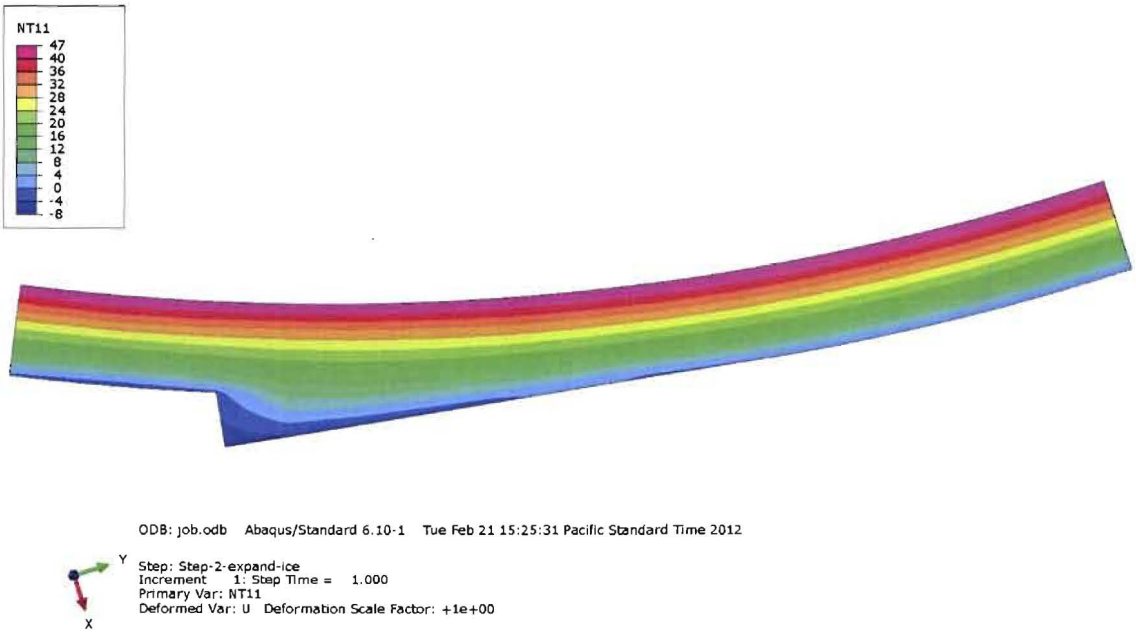

Figure 10 – Worst Case Temperatures (°F) calculated for the Blizzard of 1977 (see Exhibit 65)

Figure 11 – [redacted] due to 1977 Blizzard Conditions

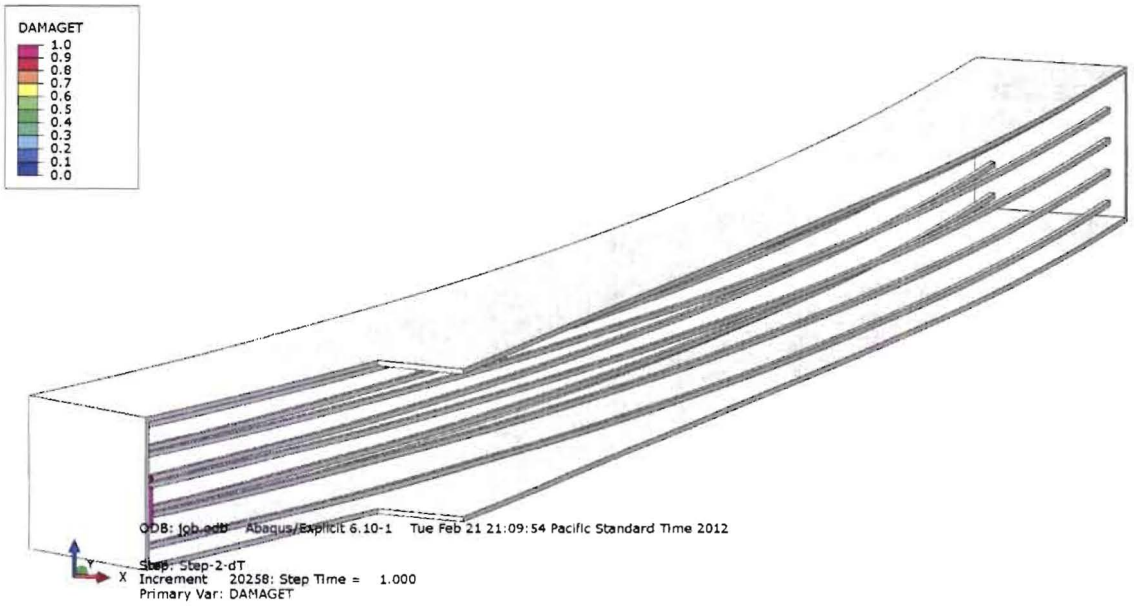

Figure 12 – Cracking Result due to 1977 Blizzard Conditions showing regions with DAMAGE > 0.7

Exhibit 74: Exhibit Not Used

Exhibit 75: Damage Propagation Analysis

Damage Propagation into Regions with High Rebar Density

Table of Contents

Summary of Results

The results of the analysis presented in this report can be summarized as follows:

- The purpose of this investigation is to study the sensitivity of the models response to location and high rebar density. This investigation identifies a plausible scenario in which damage under the shoulders propagates into the shell due to high rebar density, particularly along the top 20' of the walls and around the main steam line opening near to the Aux Building roof.
- The environmental conditions and nonlinear CTE studied are the same as in Exhibit 74.
- The locations of the cracking remain confined to the observed crack locations at the OF rebar mat, both under the thick sections of the shoulders and in locations where the horizontal rebar is spaced on 6" centers.
    - The model at the top 20' of the walls shows some damage in the flute valley, which is in line with observation.
    - The model near the Aux building roof shows less damage in the flute valley, which is also in line with observation.

Modeling Summary

Overall Approach

The analysis results presented here is a result of many different modeling efforts combined. The convective heat transfer due to wind around the shield building was calculated using a computational fluid dynamics (CFD) model taking into account the wind velocity and direction. The surface roughness, the raised shoulder geometry around the flutes as well as the auxiliary buildings was included in the CFD model. A separate heat transfer analysis consisting of the free-standing reinforced concrete shield building, the free-standing steel containment vessel, and the annulus/hollow space between the two are included. The transient heat transfer model included the duration of two or three days in order to reach accurate temperature predictions. Effects included are solar radiation (tracking of the azimuth and elevation of the sun), the ambient temperature variation from meteorological data, and the temperature on the inside of the steel containment vessel. The details of the wind and thermal modeling are reported separately in the Root Cause Analysis Report.

The calculated "worst case" temperature distribution in the reinforced concrete Shield Building is mapped onto the Abaqus Global Model with an applied offset of 20°F to simulate nominal conditions rather than worst case conditions. A coupled temperature-displacement analysis for each temperature condition is performed using the Abaqus Global Model. The computed displacements for the shield building and the mapped temperatures are subsequently used [redacted] The usage of the [redacted] technique is required [redacted].

Gravity is omitted from [redacted] the global models [redacted]. It is expected gravity would have relatively little effect on the results based on previous studies, which are summarized in Exhibit 64 – Thermal Stress Analysis with Gravity and Wind Load.

Finite Element Software

Abaqus version 6.10 for Linux 64-bit was used exclusively to solve the finite element analysis models presented here. Abaqus is generally considered the gold standard for nonlinear analysis.

Scenarios Modeled

The following scenario is presented in this report. The details of the scenario and the selection of the time of day are summarized separately in the Root Cause Analysis Report.

- Temperatures 20°F above calculated "worst case" temperatures (-24°F ⇒ -4°F)
- Nonlinear CTE curve that is adapted from Exhibit 57 Figure 4
- Saturation depths of at least 3"
- Reduced effective fracture toughness of the concrete (discussed below)

Background

Expansion of concrete due to freezing of entrapped moisture was studied in the [redacted].

Global Model Description

The drawings used as geometry input for the global model are:

- Drawing No: C-100 Rev. 5 "Shield Building Foundation Plan & Details SH. 1"
- Drawing No: C-110 Rev. 6 "Shield Building Roof Plan Wall Section & Details"

All vertical reinforcing bars in the containment shell section are modeled as rebar #10 (diameter 1.270") at 12" center to center spacing. The inner face horizontal rebars are #8 (diameter 1.000") at 12" spacing. The outer face horizontal rebars are # 11 (diameter 1.410") at 12" spacing except in the top 20' of the walls where the spacing is 6". The vertical and horizontal rebars in the shoulder sections are #8 at 12" spacing.

Material Properties

The material properties used as input to the finite element analysis in this report are summarized in the following documents attached to the Root Cause Analysis Report:

- Exhibit 56, Figure 2.1.4: Material Properties for Davis-Besse 3D Nastran Global Model
- Exhibit 56, Section 4.7: Effects of Variable CTE
- Exhibit 57: Temperature dependent coefficient of thermal expansion (CTE)

Material Properties specific to this analysis include the tensile strength (F_T) and the fracture toughness or "strain energy" (G_F). These are inputs to the Concrete Damaged Plasticity (CDP) material model, which was developed by Lee-Fenves and implemented natively in the Abaqus FEA software. The Lee-Fenves material model and the implementation in Abaqus are recognized to accurately predict cracking in concrete by the concrete modeling community. This technology is new to the nuclear industry.

The tensile strength of the Davis-Besse concrete was tested and found to vary from roughly 500 psi to 1000 psi with an average strength close to 900 psi. The test methods used to measure the tensile capacity will generally produce varying results depending on sample size and test method (e.g. split tensile vs. direct tensile). And, the samples used in these tests may have been too small for the standard test, thus over-predicted the strength. The strength of the concrete will also vary locally, with the concrete in the immediate vicinity of the rebars usually being weaker due to a higher void fraction in those areas. The samples were taken from regions away from the rebars (purposely to avoid the rebars). There is also some uncertainty in the modulus of elasticity. These models assumed E = 4.94Msi, when the stiffness may have actually been closer to 5.9Msi, which is about 20% higher and would increase the stresses by up to 20%. In this case, we assume an effective strength (tensile capacity) of F_T = 600 psi, which is toward the low end of the test results.

The fracture toughness ("strain energy", G_F) of the Davis-Besse concrete was not measured. Various values of G_F were tried and calibrated to the observed cracking. By means of comparison, the fracture toughness of the Crystal River concrete was estimated to be about 0.4 in-lb/in^2.

These values serve as starting points, F_T = 600 psi and G_F = 0.4 in-lb/in^2

Due to the known mesh size dependency in the Lee-Fenves material model, it is necessary to treat the measured strength parameters as starting points only. The mesh used for these models has very large elements relative to what the material model expects, and the stress concentrations are not fully developed. This inhibits cracking significantly. Therefore, it is necessary to use a lower set of strength parameters as an "effective strength" specific to the mesh. A sensitivity study is performed and a

reasonable set of strength parameters is found to result in cracking of the concrete due to the conditions outlined above. These strength parameters are F_T = 600 psi and G_F = 0.09 in-lb/in^2.

Coefficient of Thermal Expansion of High Moisture Concrete

The coefficient of thermal expansion (CTE) of high moisture concrete is a highly nonlinear function of temperature. This is associated with the 9% volume expansion of the freezing of entrapped water. The freezing of water in small pores in concrete takes place at a lower temperature than 32°F due to surface tension, which prevents the formation of ice at 32°F. The water in the concrete freezes at varying temperatures depending on the pore size. This creates a nonlinear dependence of the CTE with temperature. This is shown in Figure 1 and is a key input to the finite element analysis presented here. (Please see Exhibit 57 for a more detailed explanation of the nonlinear CTE.)

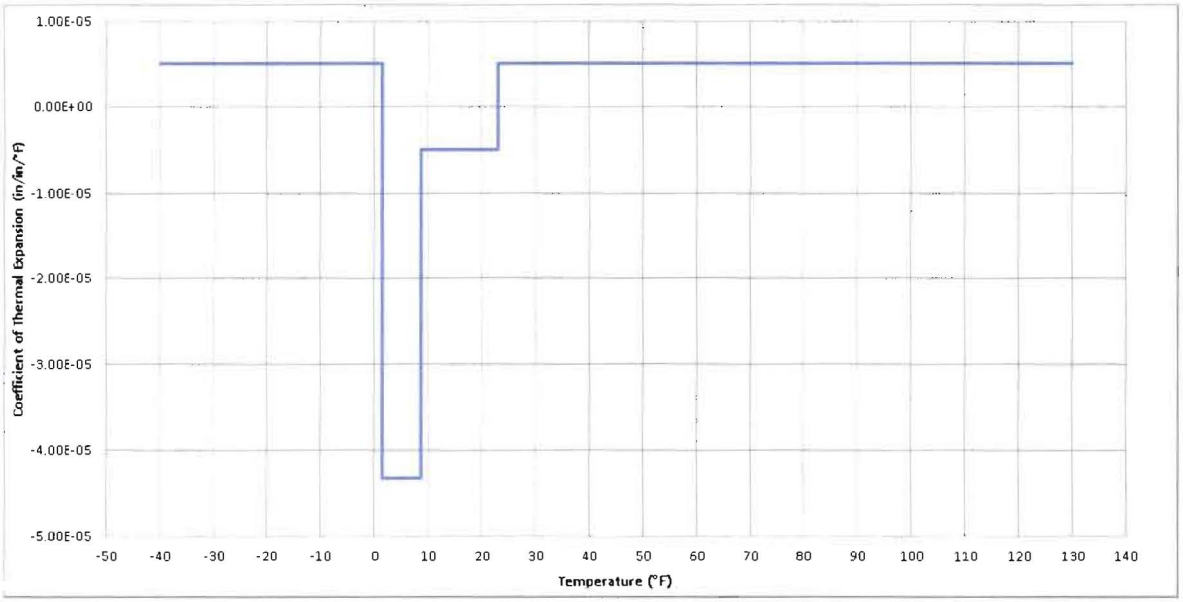

Figure 1 – Nonlinear CTE for Davis-Besse Concrete with 93% Moisture Content (See Exhibit 57)

Without having enough information to perform a thorough 3D moisture diffusion analysis on the Davis-Besse shield building model with measured properties taken from Davis-Besse concrete, it was necessary to make an assumption about the moisture gradient and proceed with that assumption in order to get a general qualitative response from the models. The most efficient way to do this was to assume that the moisture content gradients essentially match the temperature gradients. Rather than producing a constant depth of penetration, this produces a variable depth of penetration that takes into account the difference in the surface area to volume ratio in the shoulders.

The models assume that there are two regions. The outermost contour region is assumed to have a saturation of 93% (see Exhibit 57 Figure 4). This region is assigned the nonlinear CTE plotted in Figure 1.

The calculation of the saturated depth is discussed in detail in Exhibit 72 "Water and Moisture Transfer into Concrete".

The rest of the structure is assigned the linear CTE of 5.2e-6, as found and discussed in Exhibit 56, Figure 2.1.4 (Material Properties for Davis-Besse 3D Nastran Global Model).

Tests of moisture penetration were also performed at the University of Colorado at Boulder, which showed that a 1-dimensional (1D) depth of water penetration up to 3 or 4 inches is possible when there are winds in excess of 90mph (such as during the 1978 blizzard). The shield building models are calibrated so that the depth of penetration is approximately 3 to 4 inches in locations subject to 1D moisture diffusion. In the flute valleys, where there is a very low surface area to volume ratio, the depth is about 3 to 4 inches. In the "middle" of the walls between the shoulders, the depth is about 3.5 to 4 inches. In the corners of the shoulders, where there is a very high surface area to volume ratio, the depth of penetration transitions from 4 inches up to as high as about 14 inches in the corner. This is due to 2D moisture penetration in the shoulders, which appears to be highly significant.

In the Results Section, Figures 7 and 9 show the region that was assigned the nonlinear CTE as the two outermost thermal gradients (4°F to -4°F). Exhibits 66 and 71 summarize some key meteorological data during and prior to the blizzards of 1977 and 1978. Depth of penetration is discussed in Exhibit 72.

Also note that the model being placed near the Aux Building roof assumes no contribution of heat from the Aux Building itself. However, it is worth noting that a similar stress state may exist in the Shield Building wall below the Aux building roof – because the elevated temperatures inside the Aux building will act to expand the concrete at the surface of the Shield Building wall, in a manner similar to the outer surface expansion due to ice above the Aux building roof.

Location of [redacted]

Figure 2 below shows the location of the detailed [redacted] in the containment structure.

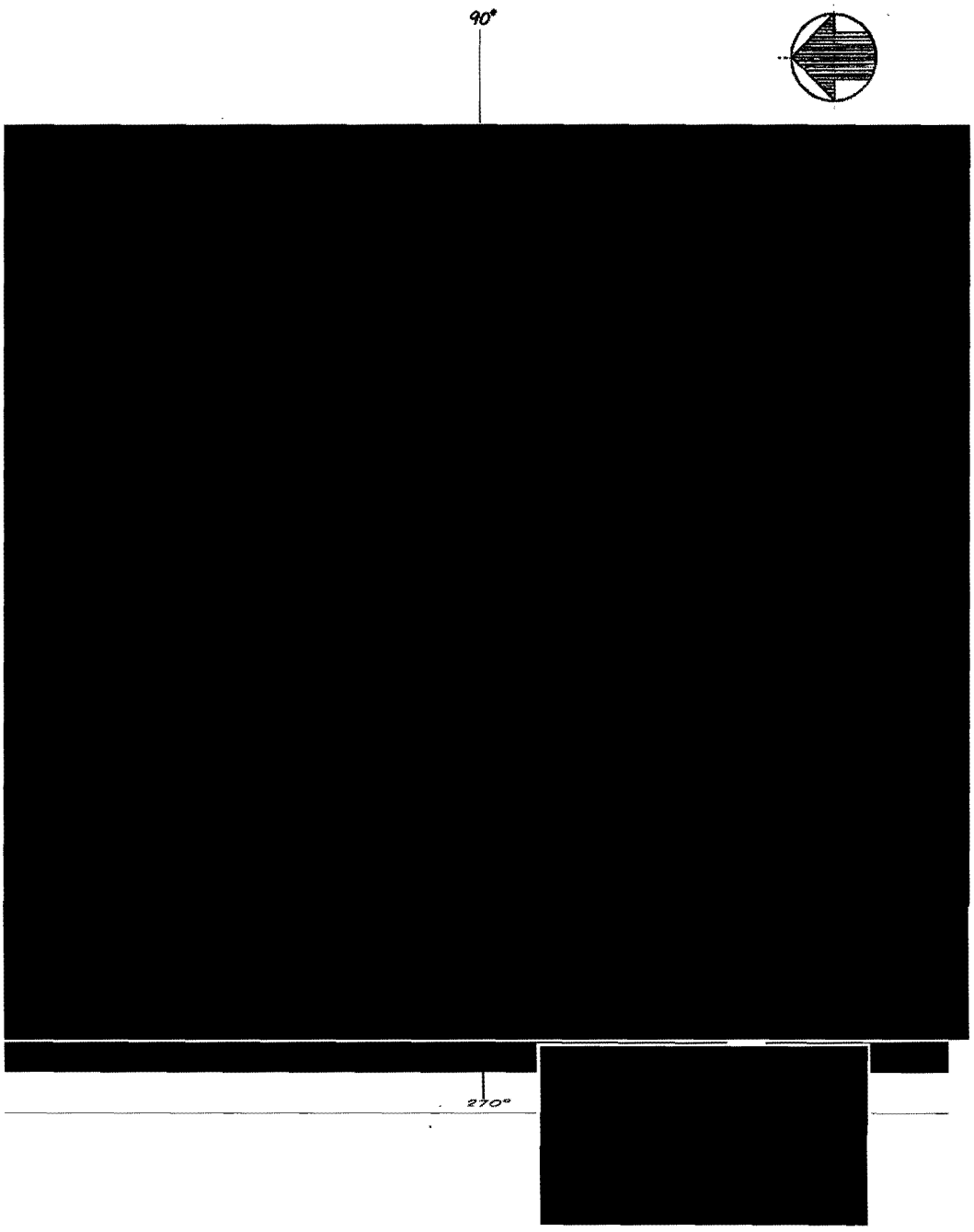

Figure 2 – Shield Building with Flute Numbers and Locations [redacted]

Circumferential Temperature Distribution at O.F. Horizontal Rebar

The temperature distribution in the [redacted] presented here were calculated in separate heat transfer analysis and mapped to the Abaqus Global Model. (See Exhibit 65) The temperature profiles around the Shield Building at the outer face horizontal rebars are shown in Figure 3. The models presented here use the worst case temperatures calculated for the 1978 blizzard with an offset of +20°F to simulate nominal temperatures. In this case, nominal temperatures will produce the most expansion and therefore the worst case stress condition for the building (see Figure 1). The +20°F offset brings the 1978 temperature gradients into rough equivalence with the lowest recorded ground temperatures during the 1978 blizzard (see Exhibit 66), which would be the expected low temperature condition assuming heavy cloud cover rather than a clear night sky (see Exhibit 65).

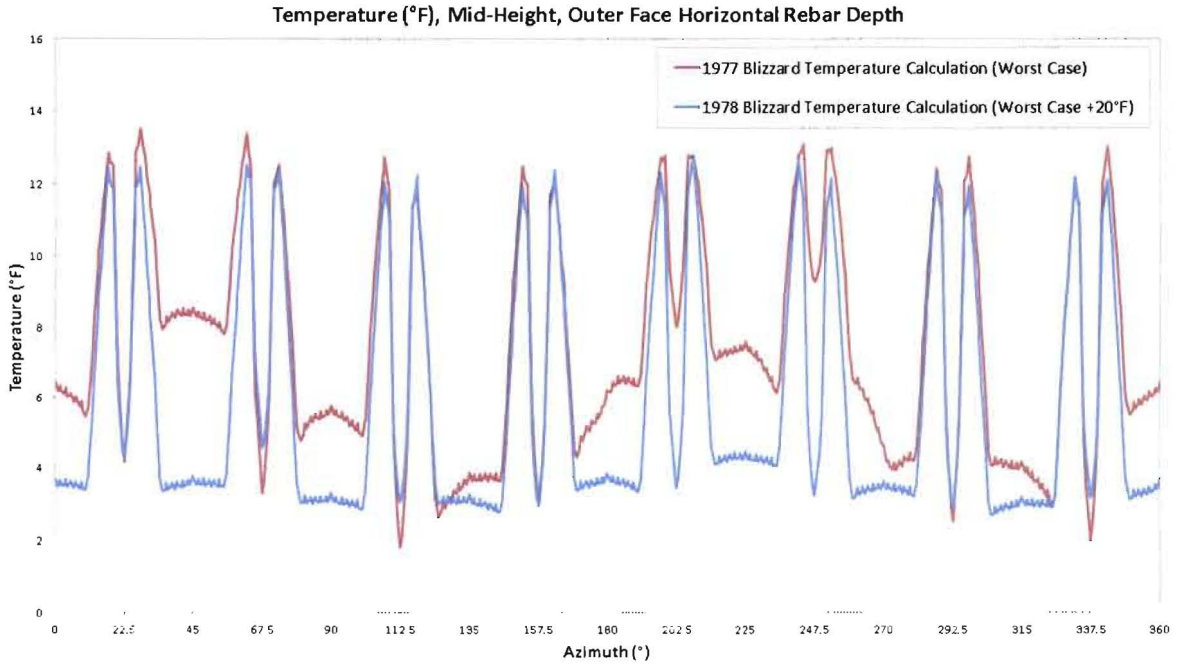

Figure 3 – Circumferential Temperature Distribution at the O.F. Horizontal Rebar Depth

Cracking [redacted] Description

In the cracking [redacted] both the inner face and outer face horizontal rebars are [redacted]. [redacted] in the circumferential direction, spanning one flute valley, one full shoulder, to the midpoint between the shoulders. The [redacted]. For this analysis, [redacted].

The temperatures and displacements [redacted]. The rebars and concrete are all modeled with solid continuum elements.

Figures 4 through 6 depict the geometry and finite element mesh of the [redacted]

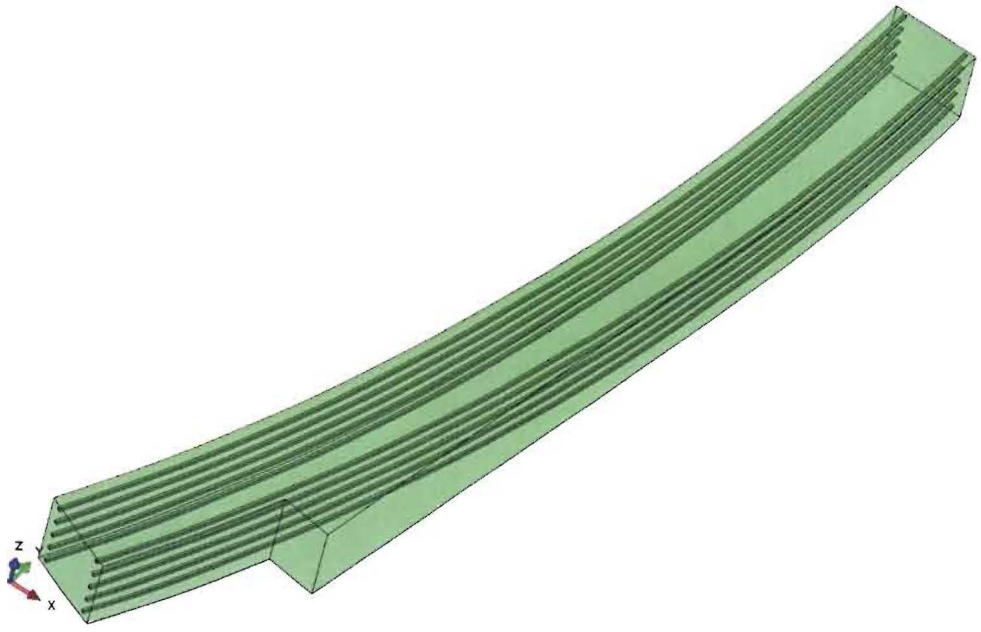

Figure 4 – [redacted] Geometry and Rebars

Figure 5 – [redacted] Detail of Flute Region

Figure 6 – [redacted] ection View of Flute Region with Mesh

Discussion

The result from the [redacted] is used to make predictions about the delamination propensity due to blizzard conditions, given the assumptions of the model.

The scale of damage ranges from 0 to 1 and represents the degree of tensile capacity lost from 0% to 100%. Any elements with red or magenta coloring are considered to have formed a structural crack, as they have less than 20% of their original strength left.

The damage that results from any tensile stress above the strength of the concrete depends on the 3D stress state as well as the strain energy available to open the crack. Low strain energy results in microcracks and high strain energy results in a structural crack.

[redacted] Results

The cracking model results shown in this section can be summarized as follows:

- The locations of the cracking remain confined to the observed crack locations at the OF rebar mat, both under the thick sections of the shoulders and in locations where the horizontal rebar is spaced on 6" centers.
    - The model in the top 20' of the walls shows some damage in the flute valley, which is in line with observation.
    - The model near the Aux building roof shows less damage in the flute valley, which is also in line with observation.
- Overall, the results show good agreement with observed cracking in the areas studied.

Top 20' of the Wall Location

The results at the top 20' location, perturbed by the 1978 blizzard are shown in Figures 7 and 8. The 20°F offset temperature contours can be seen in Figure 7 and the cracking results are shown in Figure 8.

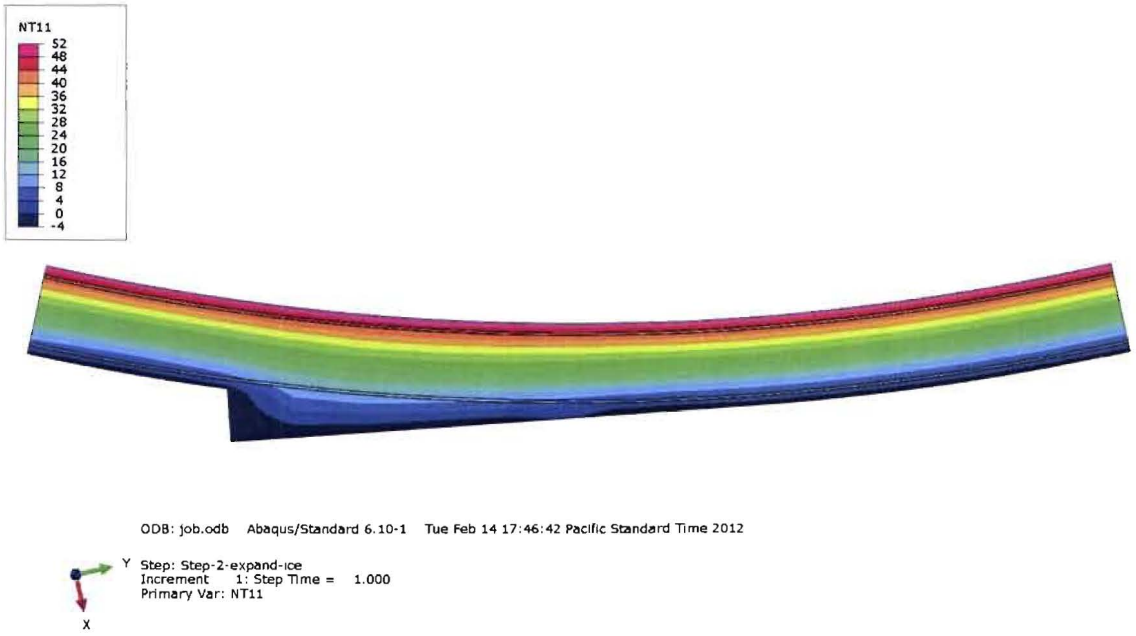

Figure 7 – Temperature Contours (°F) in the Top 20' of the Wall

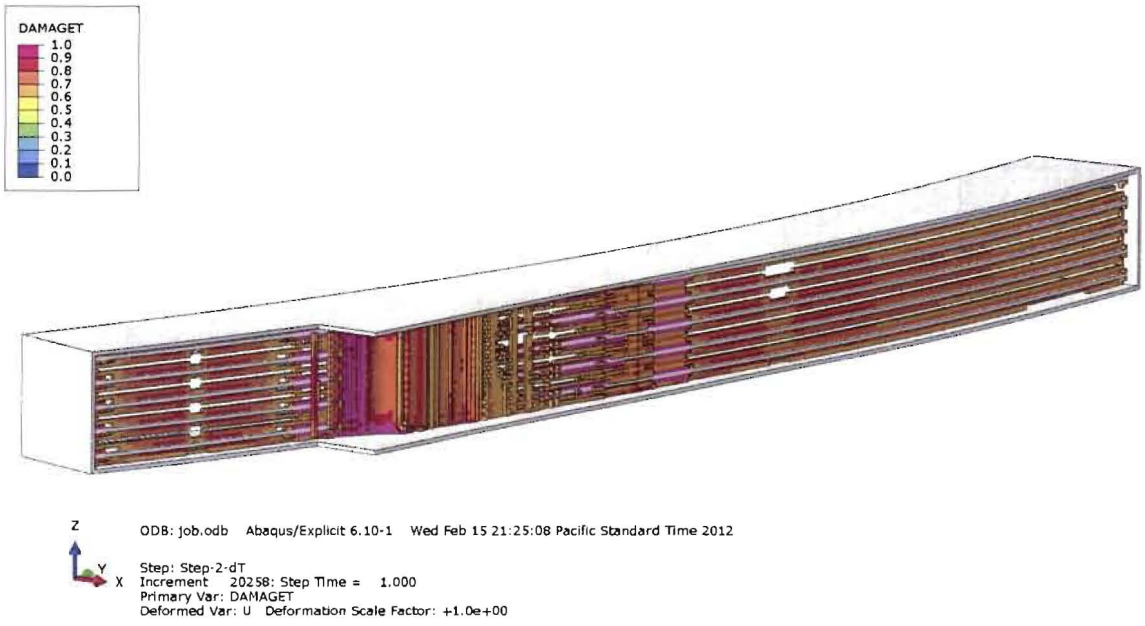

Figure 8 – Cracking Result in Top 20' of the Wall showing regions with DAMAGE > 0.6

Steam Line Location

The results at the steam line location, perturbed by the 1978 blizzard are shown in Figures 9 and 10. The 20°F offset temperature contours are in Figure 9 and the cracking results are shown in Figure 10.

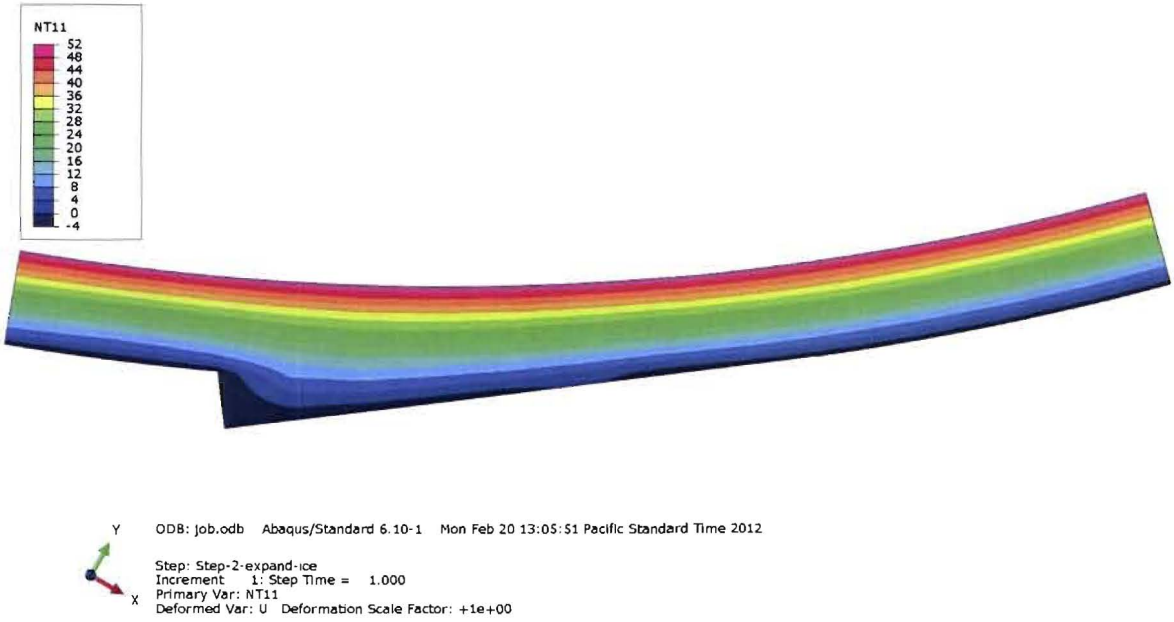

Figure 9 – Temperature Contours (°F) at Steam Line

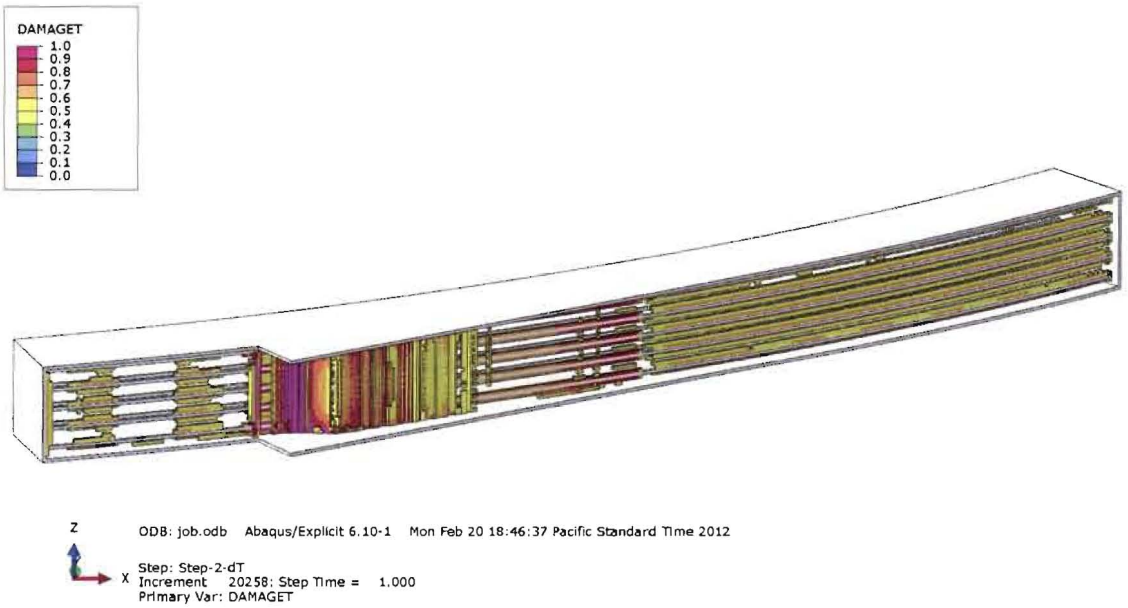

Figure 10 – Steam Line Area Cracking Result showing regions with DAMAGE > 0.6

Exhibit 76: Sample List and Activity for Lab Testing

Performance Improvement International

Providing a competitive advantage through research and applications

To: [redacted]

From: [redacted]

Date: 02/27/2012

Subject: Laminar Cracking of the Davis-Besse Shield Building – Sample List & Activity of Concrete-Core Samples

[redacted]

You will find detailed in what follows a list of the concrete-core samples received from Davis-Besse and the corresponding activities performed.

[redacted]

Sample List & Activity

Sample Handling

Twenty Eight (28) total samples were received from Davis-Besse Nuclear Power Station for laboratory tests and examination.

Each sample is alpha-numerically identified and begins with either an 'F' or an 'S' depending on the area of the shield building from which the sample was extracted, that is, from the *Flute* or from the *Shoulder*.

As the samples were received, they were photo documented in their 'As Received' condition, as can be seen in Figures A1 & A2. Afterwards, the samples were marked from the "exterior surface" to the end of the sample in 1.0 inch increments, they were also photographed. The exterior surface is defined as the surface from which the core drill begins. Thus, it is possible for the exterior surface to be the inner or outer diameter surface of the shield building. The samples were also inspected and cracks identified. Figure A3 & A4 show examples of these photo-marked samples.

Tables A1 & A2 show the list of samples received and the corresponding tasks performed on each respective sample. Note that the samples had varying degrees of testing and examination.

Table A3 documents the disposition of 6 out of the 28 samples which were not examined nor tested by methods described in tables A1 & A2.

Table A 1: List of Samples and Tasks Performed on Samples (* Fracture was cut)

Sample	Date Received	Photo As Received	Examine for Cracks and Mark	Photo as Marked	Isolate Cracks and fractures	Carbonation Test Crack(s) and Fractures (millimeters)	Longitudinal Cut	Aggregate Size and Fraction, (inches)	Coarse Void Size
F3-1	10/29/2011	X	X	X	X*	X	X	X	X
S11-1	10/29/2011	X	X	X	X	X	X		
S11-2	10/29/2011	X	X	X	X	X	X		
S12-1	10/29/2011	X	X	X	X	X	X		
S12-2	10/29/2011	X	X	X	X	X	X		
S16-3	10/29/2011	X	X	X	X	X	X		
S5-1	10/29/2011	X	X	X	X	X	X		
S5-2	10/29/2011	X	X	X	X	X	X		
S7-1	10/29/2011	X	X	X	X	X	X	X	X
S7-2	10/29/2011	X	X	X	X*	X	X		
S7-3	10/29/2011	X	X	X	X	X	X		
S9-1	10/29/2011	X	X	X	X	X	X		
S9-2	10/29/2011	X	X	X	X	X	X		
S-9-653-11	11/10/2011	X	X	X	X	X	X	X	X
S-9-785-22.5	11/10/2011	X	X	X	X	X	X	X	X
S-7-656.5-6.5	11/10/2011	X	X	X	X	X	X	X	X
F2-790.0-4.5	12/2/2011	X	X	X	X	X			
F5-791.0-4	12/2/2011	X	X	X	X	X			
F4-794.0-3.5	12/2/2011	X	X	X	X	X			
S2-798.5-4.5	12/2/2011	X	X	X	X	X			
S3- 55'	11/2/2011	X							
S13-633.08	1/17/2012	X	X	X					

Table A 2: List of Samples and Tasks Performed on Samples (* Fracture was cut)

Sample	Date Received	Coarse Void Size on Transverse Fractures	Fine Void Size	Micro Crack Examination	Micro-Hardness Coarse & Fine Aggregate and Cement	Dry/Wet Carbonation Tests	Coarse Void Size on One Transverse Fracture Only	Coarse Void Size on Rebar Imprint	EDS of Iron Oxide Transfer
F3-1	10/29/2011		X	X	X				
S11-1	10/29/2011			X					
S11-2	10/29/2011	X		X					
S12-1	10/29/2011	X		X					
S12-2	10/29/2011	X		X					
S16-3	10/29/2011	X		X					
S5-1	10/29/2011	X		X					
S5-2	10/29/2011	X		X					
S7-1	10/29/2011		X	X					
S7-2	10/29/2011			X					
S7-3	10/29/2011	X		X					
S9-1	10/29/2011	X		X					
S9-2	10/29/2011	X		X					
S-9-653-11	11/10/2011			X					
S-9-785-22.5	11/10/2011			X					
S-7-656.5-6.5	11/10/2011			X					
F2-790.0-4.5	12/2/2011			X			X	X	X
F5-791.0-4	12/2/2011			X					
F4-794.0-3.5	12/2/2011			X					
S2-798.5-4.5	12/2/2011			X					
S3- 55'	11/2/2011			X		X			
S13-633.08	1/17/2012						X		X

Table A 3: Samples shipped out from Photometrics for Mechanical and Physical Testing

Sample ID	Date Received	Photo As Received	Disposition	Status
S9	11/1/2011	X	Shipped to Dr. Xi on 11/7/2011 (14" piece only), Shipped to Dr. Xi on 11/14/2011 (7" piece only)	Dr. Xi Results
Main Steam Room	11/1/2011	X	Shipped to Dr. Xi on 11/7/2011	Dr. Xi Results
EDG Hallway #1	11/1/2011	X	Shipped to Dr. Xi on 11/14/2011	Dr. Xi Results
S-1	11/10/2011	X	Picked Up By Twinning Labs For Compressive Strength and MOE on 11/14/2011	Complete
S-3	11/10/2011	X	Picked Up By Twinning Labs For Split Tensile on 11/14/2011	Complete
S-8	11/10/2011	X	Picked Up By Twinning Labs For Step Loading Fatigue Test on 11/14/2011	Shipped to Dr. Xi

Figure A 1: Example of *As Received* Core Sample (Core F3-1)

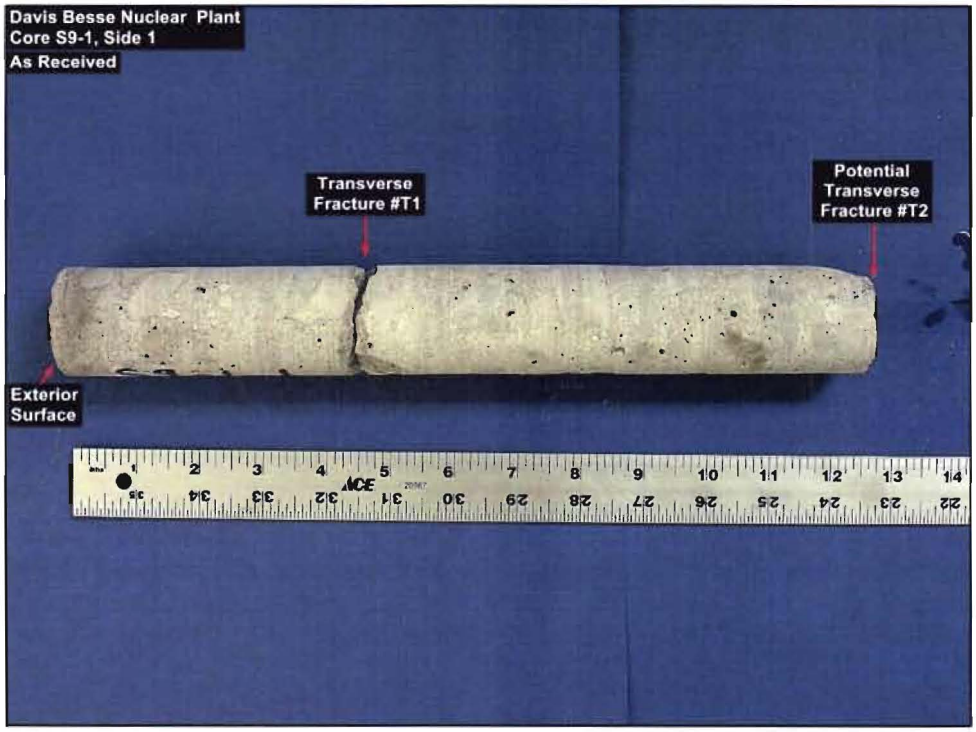

Figure A 2: Example of *As Received* Core Sample with Transverse Crack (Sample # S9-1)

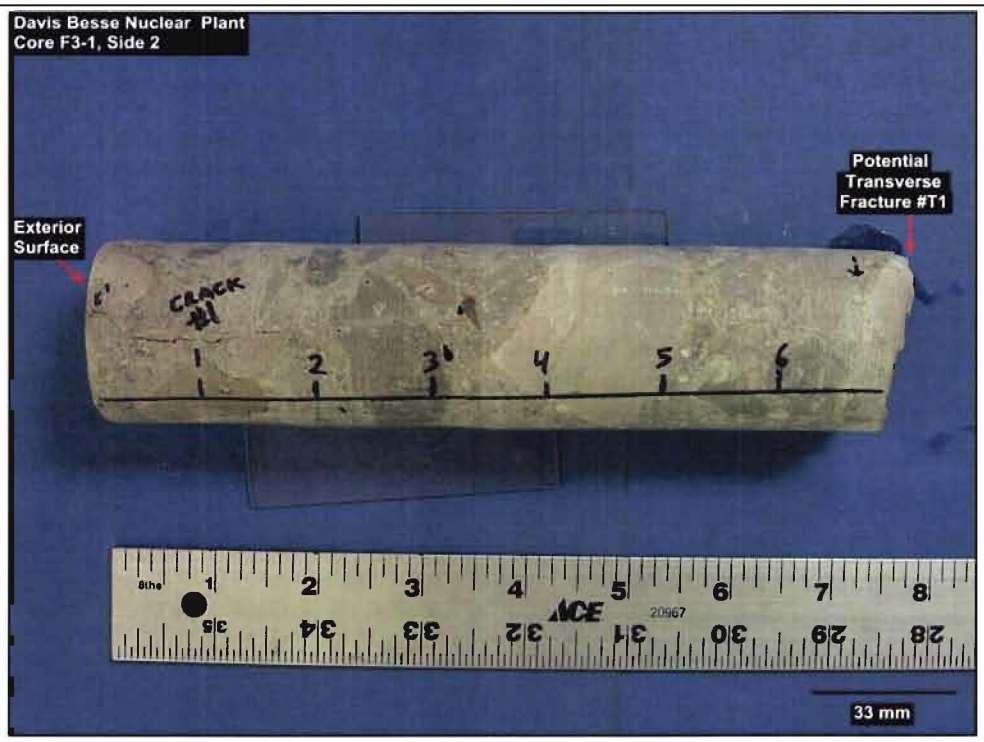

Figure A 3: Marked Sample at 1" Intervals, Cracks Identified (Sample # F3-1)

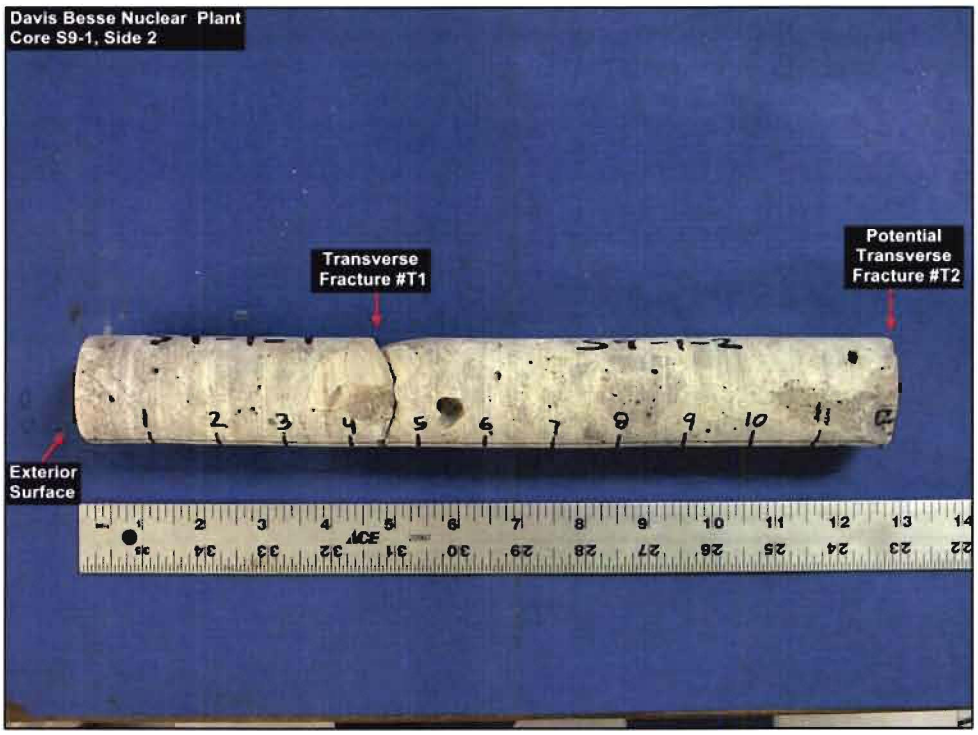

Figure A 4: Marked Sample at 1" Intervals, Cracks Identified (Sample # S9-1)

Exhibit 77: Aggregate Size Distribution
& Void Fraction Lab Testing

Performance Improvement International

Providing a competitive advantage through research and applications

To: [redacted]

From: [redacted]

Date: 02/27/2012

Subject: Laminar Cracking of the Davis-Besse Shield Building – Concrete Sample Testing for Aggregate Size Distribution and Void Fraction

[redacted],

Based on my observation and examination of concrete-core samples received from the Davis-Besse Shield Building, my findings for Aggregate Size Distribution and Void Fraction are detailed in what follows.

[redacted]

Aggregate Size Distribution and Void Fraction Analysis

Aggregate Size Distribution

ASTM C 856 Paragraph 8.1 allows for procedures to be chosen based on the purpose of the examination. The procedure used for determination of the Area Fraction of Aggregates in concrete will be discussed in what follows.

Of the three established methods for determining the area of a phase, the Delesse Method was chosen due to the limited sample sizes. In addition, Image J which is a government sponsored image analysis software program was used to facilitate this method.

The aggregate size is measured using Feret's diameter and coarse aggregates are considered those which have a major diameter of 0.3" or greater. Feret's diameter is used as defined in the in the Image J handbook:

> *Feret's diameter: The longest distance between any two points along the selection boundary, Improved in IJ 1.45m also known as maximum caliper.*

The procedural outline along with an example is shown in what follows:

1. The surface sample is polished then decorated with phenolphthalein which colors the concrete paste (purple) but not the aggregate. A micrograph is then taken.

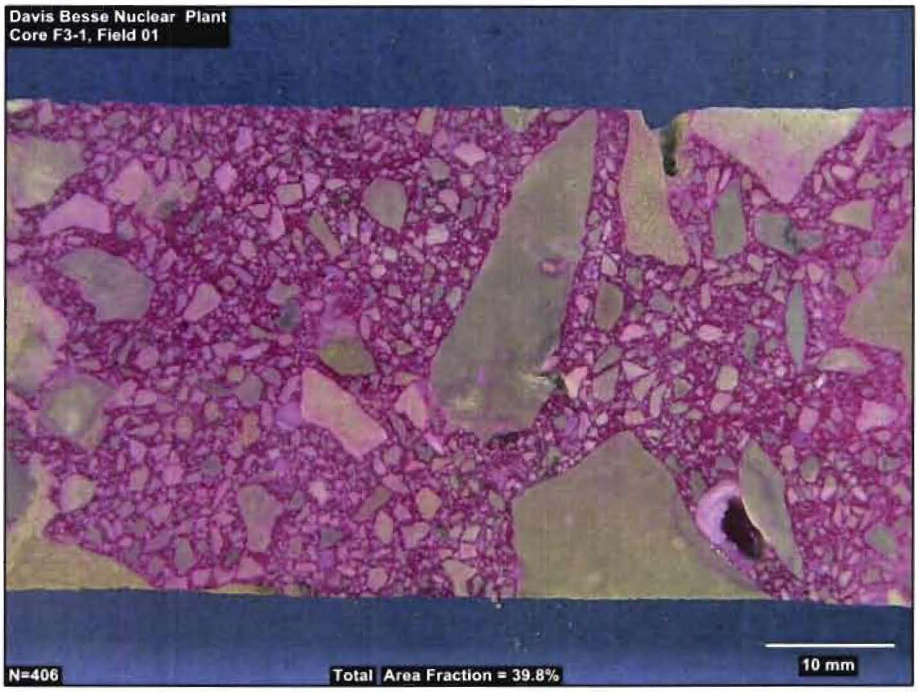

Figure A 1: Micrograph of paste (red) / Aggregate mixture paste is decorated with phenolphthalein

2. The micrograph is then converted to grayscale via green channel for enhanced contrast.

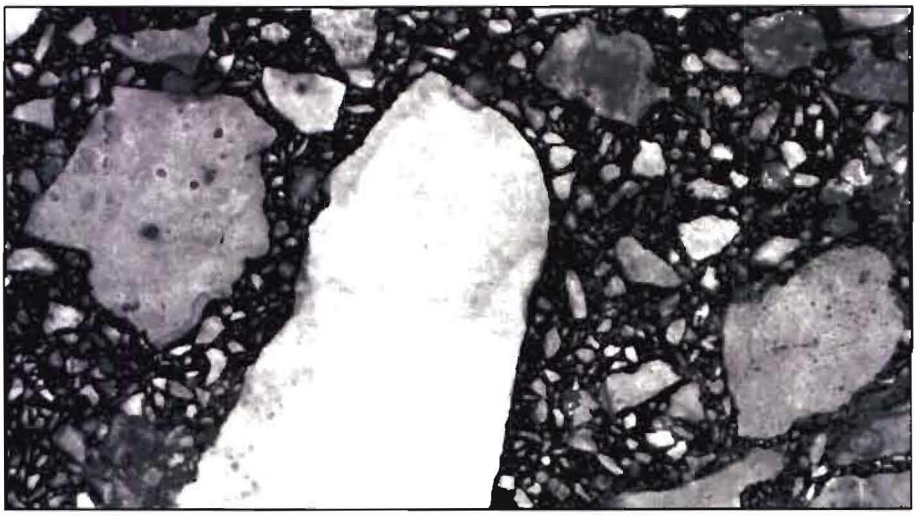

Figure A 2: Micrograph of paste / Aggregate mixture converted to grayscale via green channel for enhanced contrast

3. The micrograph is further converted to a Binary Selection of Aggregate Particles.

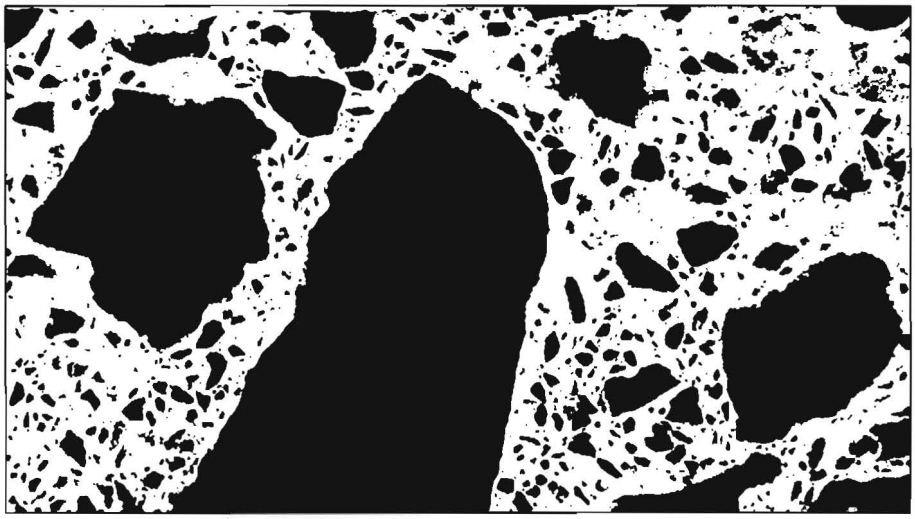

Figure A 3: Binary Selection of Aggregate Particles

4. The aggregate size is then represented by image analysis, using Image J.

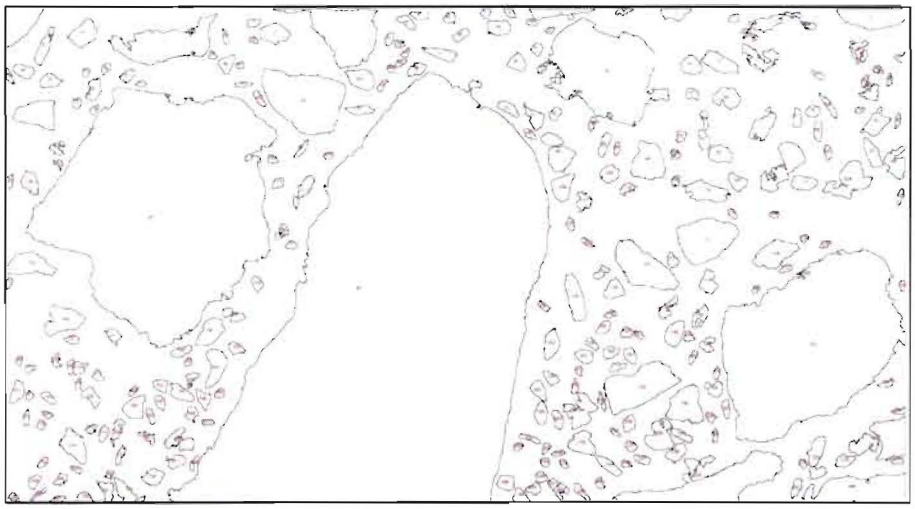

Figure A 4: Representation of Aggregate Size by Image Analysis,
(The minimum aggregate size analyzed was set to 0.0004 square inches)

5. A table is generated listing each aggregate and its corresponding Feret diameter and Area.

	Area	Feret	%Area	FeretX	FeretY	FeretAngle	MinFeret
246	0 002	0.098	100	1 817	1 654	144.345	0.035
247	6 913E-4	0.044	100	0.096	1.684	33 690	0.021
248	7.064E-4	0.035	100	1.644	1.663	143.130	0.030
249	6.189E-4	0.046	100	2 717	1 659	167.005	0.019
250	5.645E-4	0 034	100	2.446	1.659	113.962	0 025
251	5.645E-4	0 039	100	1.701	1.665	138.576	0 022
252	7 457E-4	0 054	100	1.892	1.671	159 228	0.027
253	5 796E-4	0.041	100	0.198	1.682	146.976	0 021
254	0.003	0 080	100	0.412	1.724	16.460	0.058
255	4.076E-4	0.037	100	0 054	1.731	79.216	0.017
256	4 830E-4	0 037	100	0.302	1.720	31.430	0 027
257	0.001	0.042	100	1.626	1.711	163.072	0.037
258	0 033	0.352	100	2.441	1.797	15 751	0 135
259	0.001	0 054	100	0 142	1.739	33.179	0 034
260	0.001	0 054	100	0 073	1.757	47 603	0 033
261	0.002	0 060	100	1.512	1.750	29 539	0 050
262	6 823E-4	0 043	100	1 821	1.720	133 363	0 031
263	0 005	0 138	100	0.334	1.720	133 977	0 089
264	0.002	0.075	100	1 682	1.724	111.801	0 044
265	0.001	0 072	100	2 419	1.790	67.166	0.032
266	0.002	0.096	100	0 268	1 727	121 675	0.049
267	0.001	0 048	100	1 598	1.762	21 038	0 036
268	0.001	0 073	100	1 751	1.739	126.327	0 027
269	5.464E-4	0 061	100	0.078	1.795	42.709	0.018
270	0.002	0 077	100	1 571	1.755	127.648	0.046
271	0.001	0 068	100	0.021	1.765	129 806	0 029
272	0.003	0.093	100	0 222	1 774	149.589	0 055
273	0 001	0.058	100	0.136	1.812	30.379	0.031

Figure A 5: Feret Diamter and Area Table generated for each aggregate found in the analysis

6. A summary report is produced for each sample under consideration, yielding the following information:
   i. Aggregate Count
   ii. Total Area
   iii. Average Size
   iv. Area Fraction
   v. Feret Diameter

Slice	Count	Total Area	Average Size	Area Fraction	Feret	FeretX	FeretY	FeretAngle	MinFeret
F3-1, Coarse Aggregate-2 JPG (green).jpg	273	2 361	0.009	40 7	0 087	1.407	1 035	89 362	0 049

Figure A 6: Output for a sample under consideration.

The following table shows the samples investigated and the subsequent results using The Delesse Method which was facilitated by Image J. For purposes of Aggregate Size Distribution, 5 samples were tested.

Table A 1: Aggregate Size Distribution Summary

Sample Identification	Number of Aggregate per Square Inch (Coarse+Fine)	Area Fraction Aggregate on Surface (Coarse+Fine) %	Coarse Aggregate Area Fraction, %	Coarse Aggregate Maximum Size, inches	Coarse Aggregate Average Size, inches	Coarse Aggregate Standard Deviation, inches	Number of Coarse Aggregate/Square inch
F3-1	73.6	49.3%	35.5%	1.614	0.598	0.327	2.4
S7-1	86.6	46.8%	31.7%	1.364	0.653	0.275	2.1
S-7-656.5-6.5	64.6	44.0%	33.2%	1.591	0.598	0.307	2.3
S-9-653-1	85.3	44.5%	28.3%	1.569	0.568	0.297	2.4
S-9-785-22.5	101.8	46.8%	34.8%	1.251	0.548	0.289	2.1
AVERAGE	**82.4**	**46.0%**	**33%**	**1.48**	**0.59**	**0.3**	**2.26**

Void Fraction Analysis on Core Samples

A methodology that meets the intent of the **ASTM C 457** Standard for Void Fraction Analysis will be detailed in what follows. Under the microscope, at 4X magnification, the areas of the coarse voids were summed and divided by the cross-sectional area of the sample under view. The micro-void fraction was measured on two samples (F-3 and S7-1). The contribution of the micro voids to the total void fraction (micro + coarse voids) was verified to be less than 10% of the coarse measured void fraction. Therefore, the micro voids were neglected in the results provided.

The under mentioned outlines the void fraction analysis method and provides some examples:

Coarse Voids on the Transverse Fracture Surface

1. Photograph the fracture surface or the rebar imprint as applicable using a magnification of 4 X (on screen).
2. Measure the voids diameter in the entire field of view and tabulate.
3. Calculate the total surface area of voids
4. Divide the total surface area of voids by the total surface area of the sample to obtain the void fraction.
5. Plot Void size distribution in histogram presentation

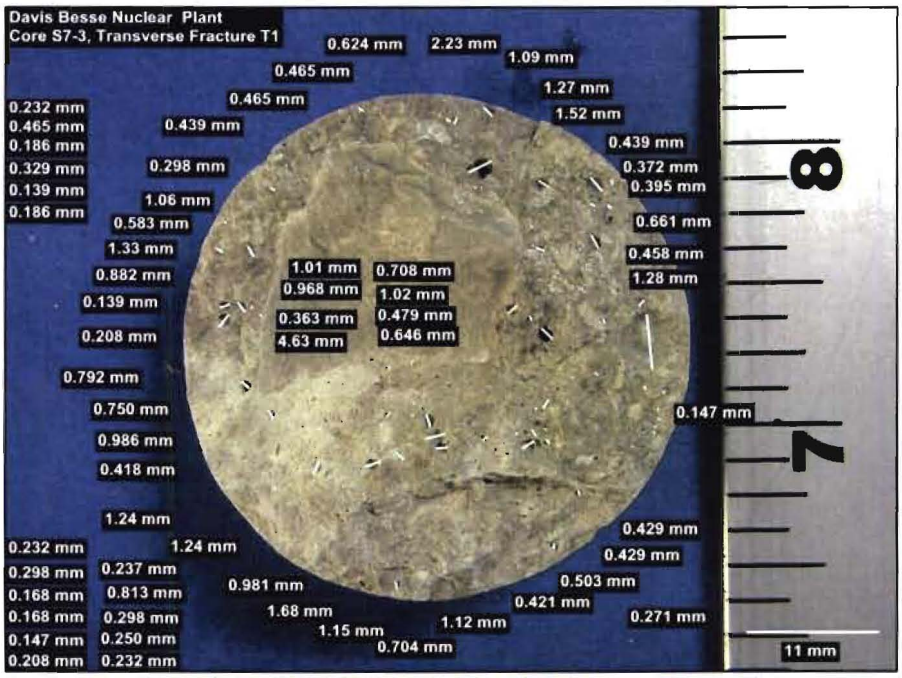

Figure A 7: Void Fraction Analysis (Core S7-3, Transverse Fracture)

Coarse Void on the Longitudinal Fracture Surface

1. Cut the core sample longitudinally, along its centerline.
2. Photograph the cut surface using a magnification of 4 X (on screen).
3. Measure the voids diameter in the entire field of view and tabulate.
4. Calculate the total surface area of voids
5. Divide the total surface area of voids by the total surface area of the sample cross-section to obtain the void fraction.
6. Plot Void size distribution in histogram presentation.

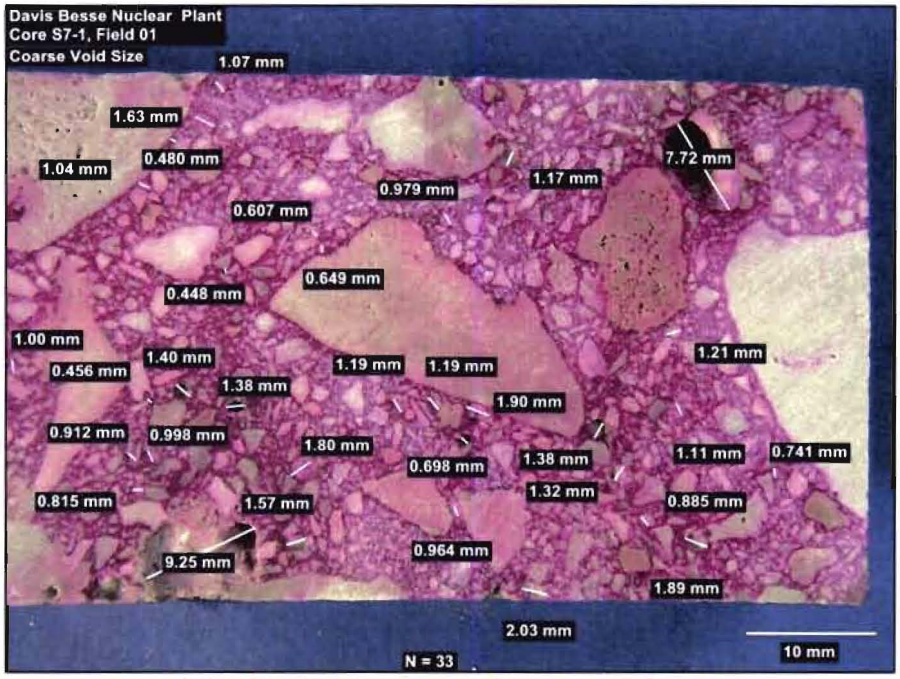

Figure A 8: Void Fraction Analysis (Core S7-1, Longitudinal)

Micro-Void Size Longitudinal Cross-Sections:

1. Cut the core sample longitudinally, along its centerline.
2. Polish the cross-section and examine under optical microscope at 50X.
3. Photograph.
4. Measure the voids diameter in the entire field of view and tabulate.
5. Calculate the total surface area of voids.
6. Divide the total surface area of voids by the total surface area of the sample cross-section to obtain the void fraction.
7. Plot Void size distribution in histogram presentation.

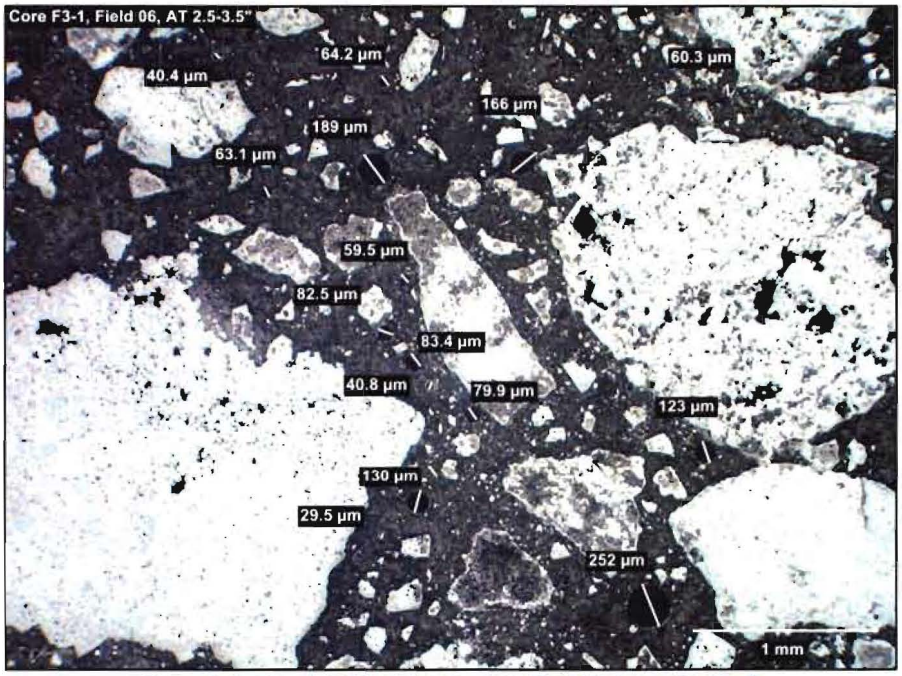

Figure A 9: Micro-Void Fraction Analysis (Core F3-1, Longitudinal)

**Note: The micro void fraction was measured on two samples (F-3 and S7-1), and the contribution of the micro voids to the total void fraction (micro + coarse voids) was verified to be less than 10% of the coarse measured void fraction. This Methodology was used in lieu of ASTM C 457 since it meets the intent. Reference micro void calculation analysis of samples F-3 and S7-1.

The following tables show the void distribution summary for samples on which void fraction analysis was conducted. The samples with an asterisk in their identification number are core samples with transverse cracks as identified by plant IR inspection.

Table A 2: Coarse Void Size and Distribution Summary for Concrete not in Contact with Rebar

Sample Identification	Total Number of Coarse Voids / Sq. inch	Number of Coarse Voids per Square inch	Coarse Void Maximum Size, microns	Coarse Void Average Size, microns	Standard Deviation, microns	Coarse Void Content by Area Fraction, %
F3-1	31 voids / 8.51 Sq. inches	3.6	6680	1917	1397	1.9%
S12-2*	56 Voids / 2.16 Sq. inches	25.9	3610	1064	796	4.8%
S16-3*	23 Voids / 2.16 Sq. inches	10.6	5610	667	1120	1.2%
S5-1*	31 Voids / 2.16 Sq. inches	14.3	2420	987	521	1.9%
S7-1*	139 voids / 20.05 Sq. inches	6.9	10800	1652	1579	3.2%
S7-3*	63Voids / 2.16 Sq. inches	29.1	2230	630	445	2.1%
S9-1*	42 Voids / 2.16 Sq. inches	19.4	3650	938	716	3.3%
S-7-656.5-6.5	179 Voids / 9.37 Sq. inches	19.1	4310	729	528	1.9%
S-9-653-1	100 Voids / 8 Sq. inches	12.6	10300	975	1125	2.6%
S-9-785-22.5	90 Voids / 8.95 Sq. inches	10.1	6710	1081	872	2.0%

Void Fraction Analysis at Areas near Rebar Contacts

Void fraction analysis at areas near rebar contacts was conducted similarly to the aforementioned. Samples F2-790 and S13-633 are the only two samples received from Davis-Besse that show concrete/rebar interaction. Void fraction analysis was conducted on both samples.

Below are the micrographs that illustrate the areas under investigation and subsequent coarse void measurements. Again, the coarse voids (neglecting micro-voids) were summed and then divided by the cross-sectional area under examination.

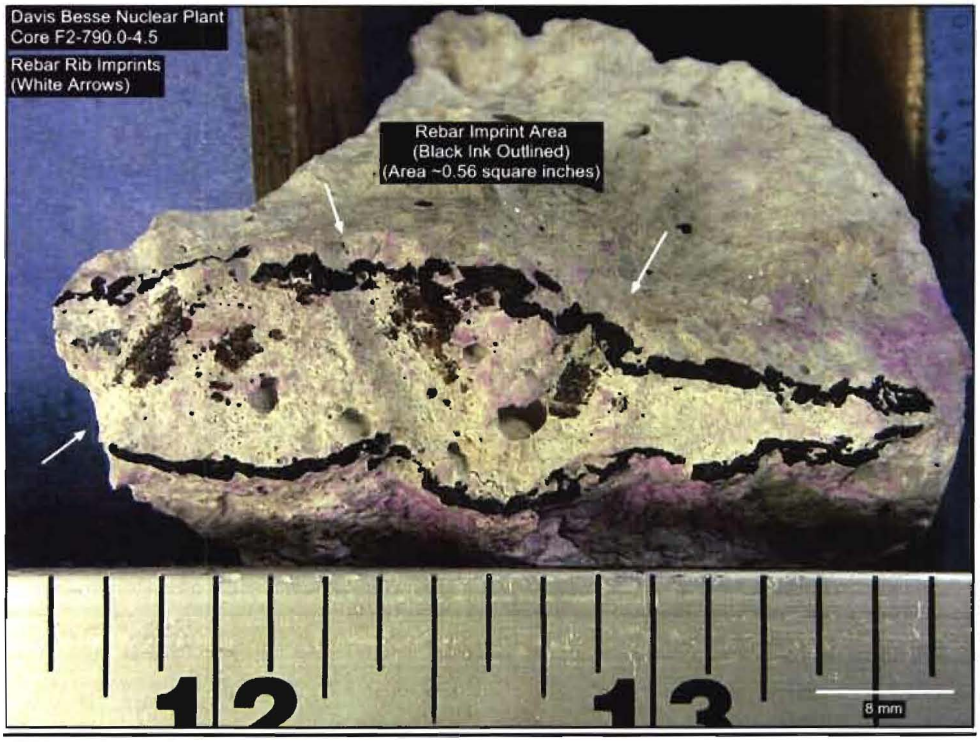

Figure A 10: Cross-sectional view of rebar/concrete contact area (Core F2-790.0-4.5)

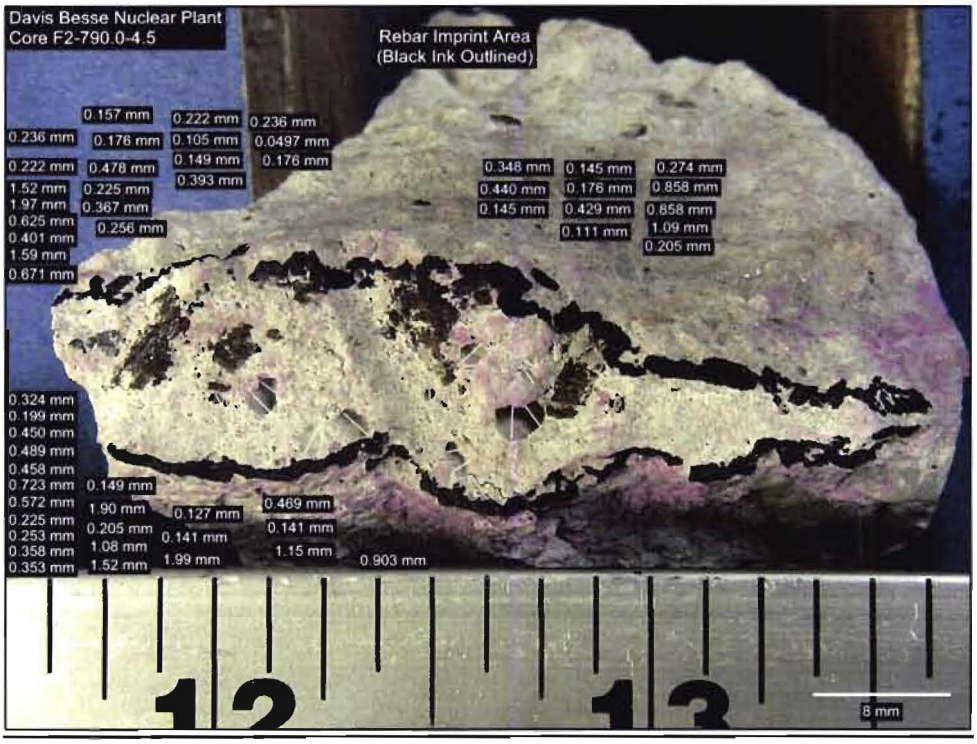

Figure A 11: Void Fraction Analysis (Core F2-790.0-4.5)

Figure A 12: Void Fraction Analysis (Core S13-633.08)

The following table shows several samples on which void fraction analysis was conducted. The samples with an asterisk in their identification number are core samples with transverse cracks as identified by plant IR inspection. The row highlighted in red shows void fraction analysis conducted on the concrete/rebar-interaction core sample, F2 790.0-4.5. The void fraction is roughly 3 times higher than for samples not in contact with rebar.

Table A 3: Coarse Void Size and Distribution Summary

Sample Identification	Total Number of Coarse Voids / Sq. inch	Number of Coarse Voids per Square inch	Coarse Void Maximum Size, microns	Coarse Void Average Size, microns	Standard Deviation, microns	Coarse Void Content by Area Fraction, %
F3-1	31 voids / 8.51 Sq. inches	3.6	6680	1917	1397	1.9%
S12-2*	56 Voids / 2.16 Sq. inches	25.9	3610	1064	796	4.8%
S16-3*	23 Voids / 2.16 Sq. inches	10.6	5610	667	1120	1.2%
S5-1*	31 Voids / 2.16 Sq. inches	14.3	2420	987	521	1.9%
S7-1*	139 voids / 20.05 Sq. inches	6.9	10800	1652	1579	3.2%
S7-3*	63Voids / 2.16 Sq. inches	29.1	2230	630	445	2.1%
S9-1*	42 Voids / 2.16 Sq. inches	19.4	3650	938	716	3.3%
S-7-656.5-6.5	179 Voids / 9.37 Sq. inches	19.1	4310	729	528	1.9%
S-9-653-1	100 Voids / 8 Sq. inches	12.6	10300	975	1125	2.6%
S-9-785-22.5	90 Voids / 8.95 Sq. inches	10.1	6710	1081	872	2.0%
Core F2-790.0-4.5 (Rebar Imprint Area)	56 Voids / 0.56 Sq. inches	100	1988	526	505	6.4%

Exhibit 78: Microcrack Lab Testing

Performance Improvement International

Providing a competitive advantage through research and applications

To: [redacted]

From: [redacted]

Date: 02/27/2012

Subject: Laminar Cracking of Davis-Besse Shield Building – Concrete Sample Testing for Microcracking

[redacted]

Based on my observation and examination of concrete-core samples received from the Davis-Besse Shield Building, my findings for Microcracking are detailed in what follows.

[redacted]

Micro Cracks

Micro Crack Examination

Laboratory examinations were conducted to determine whether or not micro cracks existed on the samples received from Davis-Besse. Virtually all samples were examined. Cross-sections of samples were prepared, polished, and scanned. There was no evidence of micro cracking on any of the samples received. Cross-sections were inspected with magnifications of up to 500 times; recorded photos are at magnifications of 25 to 100 times.

There are numerous evidential photographs that show no micro-cracking, however, only a few will be shown below for illustration purposes.

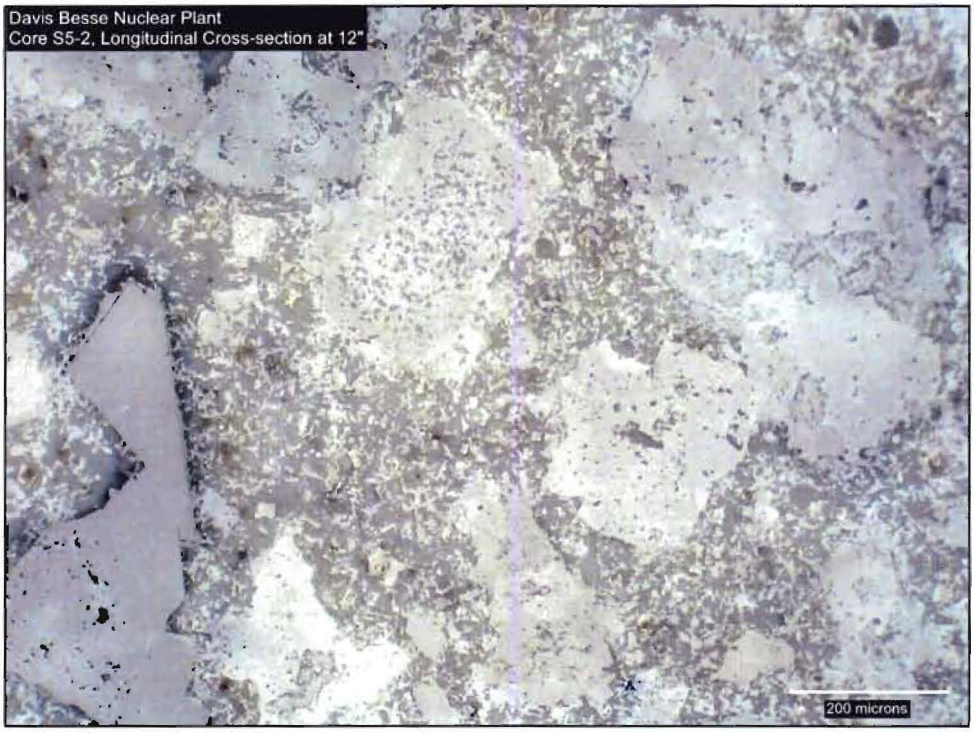

Figure 1: Magnification at 100 Times

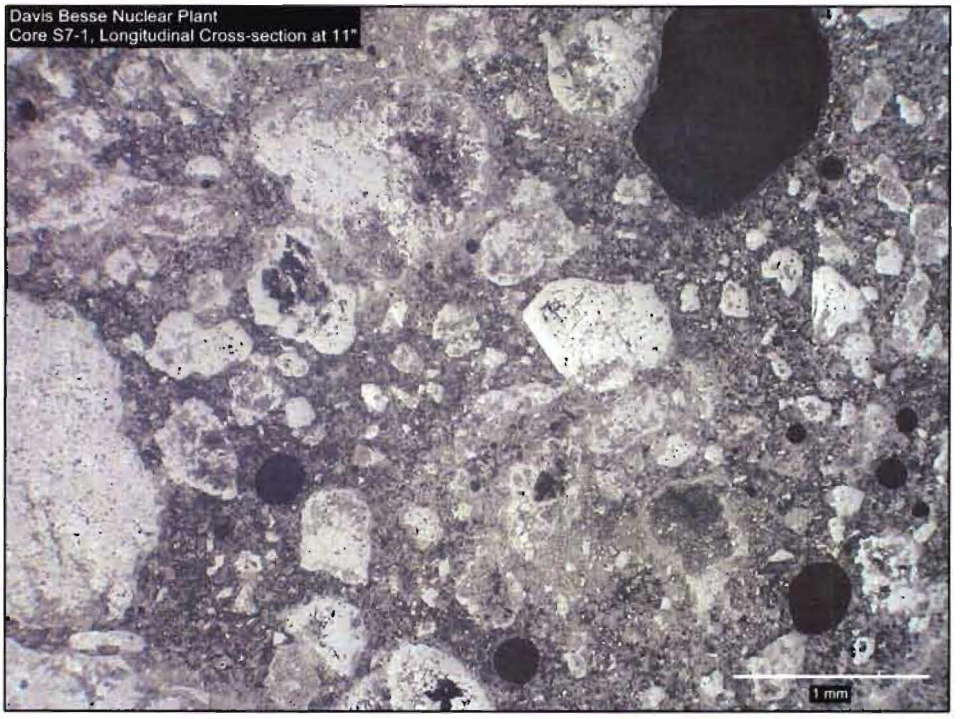

Figure 2: Magnification at 25 Times (Core S7-1)

Figure 3: Magnification at 100 Times (Core F5-791.0-4)